PERCEPTUAL LEARNING: EXPERIMENTAL AND COMPUTATIONAL CONSIDERATIONS

by
Erika Dunn-Weiss

A dissertation submitted to Johns Hopkins University

in conformity with the requirements for the degree of Doctor of Philosophy

Baltimore, Maryland

September 2020

© 2020 Erika Dunn-Weiss

All rights reserved

Abstract

Perceptual learning – learning to see the difference between similar images through repeated practice – has long fascinated neuroscientists as a means of inducing plasticity in the adult visual cortex. However, the neural underpinnings of visual perceptual learning are still debated. New approaches that investigate visual perceptual learning at the population level, and across visual areas, are needed. This thesis advances both experimental and computational techniques to address this need.

In chapters 2 and 3, I advance chronic two photon-imaging in the behaving ferret as a means of investigating the effects of learning on a population of primary visual cortical neurons. First, in chapter 2, I evaluate the visual capabilities of the ferret in order to establish the ferret as an animal model for studying visual perceptual learning. I demonstrate that ferrets are good behavioral subjects, with performance on motion and form integration tasks that is well-characterized by standard psychometric functions. I also develop a behavioral setup that is compatible with two-photon imaging studies. In chapter 3, I describe the design and assessment of a chronic imaging implant in ferrets. I show that a healthy cranial window can be maintained for up to three months with this implant, and demonstrate two-photon imaging through the imaging chamber for 9 weeks.

In chapter 4 of this thesis, I investigate the cascading effects of learning-induced plasticity in a deep convolutional neural network. Broadly, by showing the ways that plasticity works together across layers in the network, I show the limitations of searching for a singular origin of learning-induced plasticity. Specifically, I show that task difficulty influences the breadth of the population of neurons that provide evidence for the classification more so than

the distribution of plasticity across layers of the network. Finally, I show that training on an easy task before training on a difficult task affects how plasticity at early processing stages impacts tuning downstream.

Taken together, the work presented in this thesis advances tools for studying the distributed effects of perceptual learning, both within a local population of neurons as well as across visual processing stages.

Readers:

Kristina J. Nielsen, Ph.D. (advisor, first reader)

Shreesh P. Mysore, Ph.D. (second reader)

Thesis Committee:

Hey-Kyoung Lee, Ph.D. (chair)

Shreesh P. Mysore, Ph.D.

Marshall G. Hussain Shuler, Ph.D.

Acknowledgements

"I'm not simply claiming that people are more important than ideas, I'm claiming that ideas cannot be independent of people. I'm claiming that ideas are not separable from the community of people within which the ideas get their meaning, and within which the ideas do their work. And so I'm claiming that our responsibility to ideas is not separable from our responsibility to each other." – Larry McEnerney, AM'80. 2020 convocation speech, University of Chicago, South Campus Residential Commons East.

First and foremost, this thesis would not have been possible without my advisor, Dr. Kristina Nielsen. I chose to work in Kristina's lab because of her ambition, the thoughtfulness and rigor that she puts into every single aspect of her work, and the close-knit community of lab members that she had created. Not only did I become an academic scholar through her mentorship, but more fundamentally, Kristina challenged me to overcome my weaknesses, and to recognize and hone my strengths. At its core, she understood that investing in me as a person was inextricably linked to investing in my scholarship. For this, I am incredibly grateful. I am also privileged to be a mentee of one of the most frequently acknowledged faculty members in the dissertations of my friends and colleagues. Her investment in students both within and beyond her lab is renowned and makes me proud.

Dr. Hey-Kyoung Lee, Dr. Shreesh Mysore, and Dr. Marshall Hussain Shuler have been the best thesis committee members a Ph.D. student could hope for. They raised deeply thoughtful questions, pushed for a high standard of excellence, were well organized, and were compassionate. I am especially grateful for the time that Shreesh made to help me develop the

proposal for the computational project described in chapter 4. I am indebted to his guidance, and I have learned a lot from him.

This work also would not have been possible without the help William Nash, William Quinlan, Lei Hao, Justin Kilbrew, Ofelia Garalde, and Cathy Evans. William Nash and William Quinlan had the creativity and craftmanship to help design and machine the behavioral setup and imaging chamber described in this thesis, and patience to work with me to clarify the design and work through multiple rounds of prototyping. I am grateful to both Lei Hao and Justin Kilbrew for not only the technical skills they provided, but for the natural inclination to teach. The most special thank you is for Ofelia Garalde and Cathy Evans. Ofelia is the heart of the lab. In addition to the invaluable work she does in helping take care of our animals, she is nurturing and kind, and an incredible listener, support, and cheerleader. Cathy is one of the most dedicated, organized, and hard-working people that I have ever met. She easily does the work of three people in a single day, and her love and care for the animals is deeply inspiring. Some of my favorite moments in the Ph.D. have been times I have had the privilege to just chat with Ofelia and Cathy – I have so much admiration for them, and aspire to be like them.

In addition to the people who made my thesis possible, I want to thank the community of co-workers and friends that I found in the lab and in MBI. First, the lab. Augusto Lempel and Ram Srinath have been my older brothers in science, two people that I have looked up to from the beginning. Later on, the lab grew to include Alexandriya Emonds, Josh Ross, Thomas Burnett, Dallas Khamiss, Jen Smith, Qingyang (Alice) Wang, and Emmanuel Osikpa. I am so, ridiculously fortunate to have had the opportunity to work with all of these brilliant, kind, and casually hilarious people, and can't wait to see what they do in their future careers. I am

especially grateful for having the opportunity to dig deeply into the theory and practices deployed in my thesis with Josh and Emmanuel, whose thoughtful questions helped this project grow. I also want to thank Josh for helping me grow as a mentor. As a mentor himself, Josh is the ideal mentee – he understands the kind of feedback that mentors need to be successful. I have learned a lot from him, and reaching the point where I was no longer his mentor but instead became his colleague was one of my proudest days. I also want to give a shout out to Alice for all of her help with the chronic imaging project - for her hard work, her humor, her style, and her resilience. Finally, I want to give a shout out to Soohoo for reminding all of the scientists in MBI that there is life outside of the lab. Many of my best experiences in Baltimore have been attending the events that Soohoo recommended.

Beyond the lab, the neuroscience department itself has been an invaluable source of community for me. My pre-thesis advisors, Dr. Amy Bastian and Dr. James (Jim) Knierim, as well as Rita Ragan and Beth Wood-Roig, were indispensable supports during the first two years of grad school. I am especially indebted to Beth for cheering me on through NeuroCog, and to Rita for making sure that I graduate with no last-minute surprises. Beth and Rita are also two of my favorite dancers, and I will miss dancing with them every year at retreat. I also want to give a shout out to the Student Diversity Committee (SDC). It has been an honor to work with such brilliant people who are dedicated to making a brighter and more equitable future for science.

Working on a Ph.D. feels like rowing a boat across Lake Michigan. There is a long, long stretch where you can't see the horizon, and you row as a matter of survival. Surviving the middle stretch was only possible with the love and support from friends and family. At Hopkins, those friends were Lujing Chen, Tim Gamache, Will Hockeimer, Kevin Monk, Alice Berners-Lee,

Michelle Sheena, Darya Task, Jen Smith, and Alexandriya Emonds. It's easy to feel alone when you feel lost or like you're not succeeding, and Lujing was the friend who stood by me the most through thick and thin, letting me know that I was not alone. Will gives the best pep talks in the history of pep talks, always has excellent tea, and had the patience to teach me how to make tetrode drives. Through Will's warm and inclusive nature, the Knierim lab felt like a second lab home. Jen was a friend I got the opportunity to know only a year before graduating, but her ability to always make me laugh, kindness, and perspective from the other side of the Ph.D. have made all the difference. Lastly, Alexandriya has been a kindred spirit on so many levels, and I simply can't imagine the past six years (or the future) without her.

Beyond Hopkins, I have the best friends in the entire universe. It is impossible to put into words how much weekly phone calls with Maham, Gautham, and Amanda have meant over the past six years, except to say that it has meant everything. And the love, support, and brilliance from Patty absolutely picked me up and pulled me out of the deepest pits of doubt. Patty's constant refrain that 'done is better than perfect' is a huge part of why this thesis is complete today – that, and her incredible surprise in-person delivery of flowers and snacks during the final hours. Special thanks to Kelly, who has been with me on every journey since the beginning of our lives, and an important shout out to my former-mentee-now-friend, Lizette, who told me plainly on day 1 that I'd better stick it out and get that title. She's the best.

Then, there are the people that made Baltimore a home over the last six years. First of course is Anne, who was a constant source of humor, storm watching, love, good food, and fawning over my dog Milo. Moving to Baltimore knowing she was in the area definitely kept me connected to family and a sense of home. Artie also gets a shout out for giving me the playlist

that got me through half the writing of this thesis. In Baltimore itself, I could not have been luckier than to have had Laura #1 and Laura #2 as roommates. Laura #1 was my first friend in Baltimore, the person who helped me fall in love with the city, and her infectious spirt and style, PG tips tea, and rabbits were the highlights of my first year in grad school. Her warm welcome set the tone for the rest of my time here in the best possible way. And Laura #2 has been the most constant cheerleader through this entire process, always willing to meet me wherever I am at, whether that is sitting on the floor or dancing around the apartment. Last but not least, Rachel, Daniel, and Roscoe have taken me in as family, and their warm and beautiful home in DC has always felt like a refuge where I could recharge. I will miss them so, so much.

Finally, I want to thank my partner, Dan, my godmother Maria, and my family. Few people can say that they have had the kind of unconditional love and support from their family as I have had my entire life. Their belief in me and their encouragement has kept me going, and talking to my mom on the way to the bus everyday was a fabulous way to stay connected across the distance. The person who has supported me the most completely throughout this journey has been Dan. Part of that support comes from things you expect from any good partnership – the love, the care, the respect, the kindness. But another huge part of it has been his calming presence, his infinite patience, his reassurance, his ability to make me laugh, and his commitment to making sure I stay well-fed. Plus, Dan is brilliant, and talking to him about my thesis at every stage has really helped the project and my thoughts to develop. I'm also grateful to Dan's family for the curiosity and support they have shown over the years.

The BIGGEST thank you of all goes to Milo Dunn-Weiss. Not only because he is so good, and smart, and kind, and handsome, and generous, and thoughtful, and full of love, but also

because he helped me come home on time, get exercise, and take play breaks. He also sat on my lap through countless hours of writing and studying. His constant companionship has made all the difference. As Dan puts it, we are ‘a binary star system’ – we reflect each other’s light.

Table of Contents

1 Introduction

One of the most significant results in the field of neuroscience was the discovery of a "critical period" in development, a window in which emerging foundational cortical circuits are most plastic – and therefore, the most vulnerable. Pioneering work by Hubel and Wiesel demonstrated that the ocular dominance properties of primary visual cortex (V1) neurons are strongly affected by monocular deprivation between the first 4 - 8 weeks of visual experience, but are unaffected by monocular deprivation in the adult cat (Hubel and Wiesel, 1970; Wiesel and Hubel, 1963). This work suggests that after the critical period of development, visual experience has little effect on the organization and function of visual cortex.

Within this context, the finding that perceptual learning – long-term improvements in the ability to perceive minute differences in sensory stimuli, achieved through repeated practice – could occur specifically for low-level stimulus attributes, such as orientation, retinotopy, and ocularity, suggested the radical possibility that certain experiences might still induce plasticity in adult V1 (Ball and Sekuler, 1982; Fiorentini and Berardi, 1980, 1981; Karni and Sagi, 1991; Sagi 2011; Schoups et al., 1995). Determining the locus of such learning-induced plasticity thus became an essential pursuit, both in order to clarify, at the level of basic science, the extent to which sensory cortices continue to be plastic into adulthood, and moreover, to understand the way in which perceptual learning might be used as a tool for rehabilitating sensory deficits in adults. Yet, the locus of perceptual learning continues to be hotly debated, with several distinct theories responding to an expansive set of psychophysical data and inconclusive neurophysiological results.

This introduction will review our current understanding of perceptual learning, expanding upon both the insight that psychophysics and neurophysiology can offer as well as each method's limitations, and summarizing key findings. We further review the interpretation of these findings by the main conceptual frameworks in the field. We conclude this introduction by arguing that, in order to advance the field of perceptual learning, new investigative tools that can track the effects of perceptual learning at network scale are needed.

1.1 Visual perceptual learning

1.1.1 Psychophysics

The phenomena of visual perceptual learning has been described by psychologists since the early 20th century, and has encapsulated everything from a butcher learning visual estimations of weight to a teacher learning to perceive differences in handwriting (Gibson, 1953). Yet, the characterization of the tuning properties of V1 neurons in the late 20th century (Blakemore and Campbell, 1969; Hubel and Wiesel, 1968) led to a paradigm shift in the way neuroscientists understood perception (Barlow, 1972), and consequently redirected the field of perceptual learning to question the neural processes underlying behavioral gains. By using stimuli that had previously been used to characterize the properties of visual cortical neurons, such as oriented bars and gratings, and by restricting training to a particular position in retinotopic space or to one eye, psychophysicists sought to use the specificity and precision of perceptual gains to infer the locus of learning-induced plasticity (Fiorentini and Berardi, 1981).

Accordingly, perceptual learning has been studied with respect to hyperacuity (Fahle and Edelman, 1993; Fahle et al., 1995; Mckee and Westheimer, 1978), orientation (Schoups et

al., 1995; Vogels and Orban, 1985), contrast (Adini et al., 2004; Dorais and Sagi, 1997; Sowden et al., 2002), spatial frequency (Fiorentini and Berardi, 1981), texture (Ahissar and Hochstein, 1993; Karni and Sagi, 1991), and direction of motion (Ball and Sekuler, 1982, 1982; Matthews et al., 1999). With the emergent understanding that orientation and spatial frequency were processed in "selective channels" in V1, i.e., that neurons were tuned to specific orientations and spatial frequencies, perceptual learning gains were evaluated for specificity to particular stimulus features. For instance, the ability to perform an orientation discrimination task at the trained stimulus orientation was measured against the subject's performance at the untrained, orthogonal orientation. If the learned sensitivity to orientation failed to transfer to an untrained, orthogonal stimulus, it was deduced that perceptual learning must be supported by a similarly selective subset of neurons, which were known to exist in V1 (Fiorentini and Berardi, 1981; Karni and Sagi, 1991; Schoups et al., 1995). Similarly, the insight that visual inputs to the two eyes remained separate within and until V1 (Hubel and Wiesel, 1962, 1968, 1977) was also leveraged to establish bounds on the possible locus of learning-induced plasticity by training monocularly and testing for transfer (Ahissar and Hochstein, 1996; Ball and Sekuler, 1987; Fahle et al., 2002; Karni and Sagi, 1991; Schoups et al., 1995). Finally, the knowledge that retinotopic receptive fields increased in size hierarchically across visual areas (Felleman and Van Essen, 1991) inspired psychophysicists to confine perceptual training to a specific position in retinotopic space and ask the extent to which gains transferred across retinotopic space (or across the visual hemifield) (Fiorentini and Berardi, 1981; Karni and Sagi, 1991; Schoups et al., 1995; Shiu and Pashler, 1992).

Early psychophysical studies of perceptual learning demonstrated an exceptional degree of specificity for orientation (Fiorentini and Berardi, 1981; Karni and Sagi, 1991; Schoups et al., 1995), retinotopic position (Fiorentini and Berardi, 1981; Karni and Sagi, 1991; Schoups et al., 1995), and even ocularity (Ball and Sekuler, 1987; Karni and Sagi, 1991). The extent of specificity observed in early psychophysical studies of perceptual learning was so profound that it quickly became a defining feature of the phenomena of perceptual learning (Dosher and Lu, 2017; Gilbert et al., 2001). This led many to theorize that perceptual learning induced plasticity in V1 (Gilbert et al., 2001), which, in turn, ignited the possibility that perceptual learning could be used as a clinical tool for visual deficits known to affect early visual processing stages. Indeed, perceptual learning has been shown to improve Snell acuity in amblyopic individuals (Levi and Li, 2009), to combat reduction in contrast sensitivity in aging adults (DeLoss et al., 2015), and even to facilitate recovery of vision after injury-induced cortical blindness in V1 (Huxlin et al., 2009).

Yet, although specificity is a desirable property when attempting to use psychophysical experiments to estimate the locus of learning-induced plasticity, specificity is antithetical to the aim of using perceptual learning as a clinical tool (Levi and Li, 2009). Thus, the circumstances under which perceptual learning gains could generalize to other stimulus features became of equal interest to psychophysicists. It has now been shown that transfer can be facilitated by including easy trials in training (Hung and Seitz, 2014; Zhang et al., 2010b). Moreover, Yu and colleagues have developed a “training-plus-exposure” paradigm that can help performance gains at the trained location “piggy-back” to a different location where the subject was exposed to a related stimulus (Wang et al., 2012, 2014; Xiao et al., 2008; Zhang et al., 2010a).

Psychophysical experiments have provided significant experimental insight into perceptual learning, and have driven much of the debate concerning the locus of learning-induced plasticity. Yet, the interplay between psychophysics and neurophysiology is crucial. Just as foundational neurophysiology discoveries about the visual system shaped the questions that psychophysicists have asked, in turn the careful and systematic psychophysical survey of visual perceptual learning has guided the inquiry of neurophysiologists into mechanisms that might underly learning-induced plasticity. In the next section, we review key neurophysiology experiments that were performed in direct response to the psychophysical experiments described above.

1.1.2 Neurophysiology

V1

Led by the hypothesis that perceptual learning induced plasticity in V1, the earliest neurophysiology experiments sought to measure changes in tuning properties of V1 neurons following perceptual learning. Schoups and colleagues (Schoups et al., 2001) trained two macaque monkeys to perform a simple orientation discrimination task, and replicated the retinotopic and orientation specificity of perceptual gains demonstrated earlier in humans. Performance thresholds were 7 to 12 times lower for the trained versus untrained position and orientation. The retinotopic specificity, in particular, allowed them to measure the effects of perceptual learning as the differences in tuning properties between neurons responding to trained and untrained regions of retinotopic space. Contrary to their expectation, the distribution of orientation tuning preferences was the same between the trained and untrained population of neurons. However, the slope of neurons tuned 12 - 20° away from the trained

orientation had sharpened by 27% on the flank that supported discrimination for the trained stimulus. This suggested that perceptual learning led to an increased discriminability of the trained stimulus within the population of V1 neurons. Although the improvement in neuronal sensitivity was subtle, and much less than the observed behavioral improvement, the observed effects put forward the idea that perceptual learning would induce plasticity within V1 in a manner that specifically targeted the most informative neurons.

Yet, within the same year, Ghose, Yang and Maunsell (Ghose et al., 2002) also trained macaque monkeys on an orientation discrimination task and did not find any significant changes in tuning curve slope in V1. Instead, they found a small but nevertheless significant reduction in the proportion of cells tuned for orientations near the trained stimulus. This was not observed in the untrained population of cells. Similarly, they found a small yet significant reduction in the response amplitude of neurons tuned near the trained orientation. Otherwise, they found no significant differences in tuning characteristics, including orientation bandwidth, peak response, and variance ratio. The authors conclude with a resounding negative result: neither a discrimination model nor a classification model based on the observed tuning properties of trained V1 neurons could account for behavioral gains – indeed, the performance of these models based on the responses of trained V1 neurons was actually slightly worse than that based on the responses of untrained neurons.

Some of the strongest psychophysical evidence in support of the position that learning induces plasticity within or before V1 was the ocular specificity observed by Karni & Sagi in a texture discrimination task (Karni and Sagi, 1991). Specifically, when subjects learned to determine the orientation of a texture through monocular training, their performance gains did

not transfer to the untrained eye, thus implicating a stage of visual processing where the input from the two eyes was still separate. Accordingly, Schwartz and colleagues sought to investigate the neural correlates of texture discrimination using fMRI (Schwartz et al., 2002). Using fMRI allowed them to not only investigate signal change in V1, but to compare response differences following perceptual learning across brain areas. Moreover, by training monocularly, Schwartz and colleagues could use responses to visual stimuli through the untrained eye as an internal control. Consistent with psychophysical results, Schwartz and colleagues found that after monocular training, V1 BOLD activity was stronger while the subjects performed texture discrimination with the trained eye than when subjects performed the texture discrimination with the untrained eye in the same retinotopic quadrant. Moreover, no similar change in BOLD activity was observed in any other area of cortex, which the authors suggest is strong evidence that texture discrimination does indeed induce plasticity within V1. Interestingly, although Yotsumoto and colleagues replicate the result that perceptual learning in a texture discrimination task increases BOLD activity in V1 following learning, they also show that BOLD activity in V1 returned to baseline levels after a few weeks, despite the persistence of behavioral gains (Yotsumoto et al., 2008).

V4

Although accounts of perceptual learning-induced plasticity in V1 differ, by all accounts, the degree of plasticity observed was substantially less than that which was hypothesized. Thus, neurophysiologists turned to V4. V4 sits at an intermediate stage of processing along the ventral pathway, such that neurons in V4 can still be responsive to low level stimulus attributes. Therefore, it was hypothesized that classical perceptual learning tasks could induce plasticity in

V4. The first study of perceptual learning in V4 was by Yang & Maunsell in 2004, replicating the orientation discrimination task design the authors had used to study perceptual learning in V1. As in their previous study in V1 (Ghose et al., 2002), the authors found a small but significant decrease in the proportion of V4 neurons with tuning preferences near the trained orientation following learning. Yet unlike in V1, tuning curve amplitudes increased significantly with training, and the population tuning curve for neurons responding to the trained stimulus was substantially narrower (bandwidth of 24° for the trained population versus 30° for the untrained population). Moreover, discriminability improved by 33%. Although changes in tuning curve amplitude were seen throughout the trained population of V4 neurons regardless of orientation tuning preference, neurons that were tuned near the trained orientation exhibited significantly more narrow tuning curves and higher discriminability. Nevertheless, the authors found that V1 neurons were more sensitive to the trained stimulus, with fewer neurons needed to discriminate between the trained stimuli than in V4. More precisely, a population of 14 V1 neurons, either trained or untrained, were needed to achieve a *d'* corresponding to 79% correct at the trained orientation difference, whereas 25 trained V4 neurons or 34 untrained V4 neurons were needed to reach the same criterion.

Raiguel and colleagues replicated the finding that V4 exhibited more learning-induced plasticity than V1 (Raiguel et al., 2006). Building on their earlier work in V1 (reported in Schoups et al. 2001), Raiguel and colleagues theorized that perceptual learning should induce plasticity in a way that would specifically target the responses of neurons that exhibited the steepest slope at the trained orientation. Raiguel and colleagues reasoned that such neurons would be the most informative to the discrimination task, and moreover, that if plasticity were to be

restricted to merely a particular aspect of the tuning of a subset of neurons, this could help preserve the existing functionality of the network. In line with their hypothesis, Raiguel and colleagues found that the flank of the tuning curve of V4 neurons tuned 22-67° away from the trained stimulus became steeper with perceptual learning. Yet, although a greater proportion of V4 neurons exhibited tuning plasticity following learning than in V1, the increase in slope of the population of neurons most sensitive to the trained stimulus was similar between V4 and V1, while the overall discriminability of V1 neurons was better than V4 neurons by a factor of 3 to 4. Moreover, untrained V1 neurons were more sensitive to the trained stimuli than trained V4 neurons. Thus, the observed tuning plasticity in V4 was insufficient to account for behavioral gains.

1.1.3 Summary

The physiology experiments described above have largely continued, rather than resolved, the debate about the locus of learning-induced plasticity, especially given the conflicting reports of plasticity in V1, and the overall failure of the reported plasticity to account for perceptual gains. In what follows, we review the most prominent conceptual frameworks for understanding visual perceptual learning, including their motivations and their hypotheses, and evaluate each framework in light of the available psychophysical and physiological data.

1.2 Conceptual frameworks for visual perceptual learning

1.2.1 Primary cortex theory

As alluded to in the introduction, the exquisite specificity observed in psychophysical perceptual learning experiments led to the hypothesis that perceptual learning induced

plasticity in V1. Neurons in V1 not only exhibit tuning for orientation, spatial frequency, and ocular dominance, but also, the most selective neurons exhibit the sensitivity needed to match behaviorally measured orientation and spatial frequency discrimination thresholds in normal adult individuals (Bradley et al., 1987). Moreover, the specificity of perceptual learning gains to retinotopic space as precise as 2.5° (Schoups et al., 1995) strongly implicated the involvement of an early stage of visual processing (Felleman and Van Essen, 1991).

Furthermore, the specificity of perceptual learning had been observed in other modalities (Recanzone et al., 1992a, 1993), and neurophysiology reports clearly demonstrated corresponding plasticity in primary cortices (Recanzone et al., 1992b, 1992c, 1993). In particular, Recanzone & colleagues observed an expansion in the population of neurons tuned for the trained stimulus in somatosensory area 3a & 3b and in primary auditory cortex of adult owl monkeys following somatosensory and auditory perceptual learning, respectively (Recanzone et al., 1992b, 1992c, 1993). They also observed tuning curve sharpening and decreased response variance in somatosensory area 3b, the latter of which could account for perceptual gains (Recanzone et al., 1992d). Neurons in A1 also exhibited tuning curve sharpening at the trained stimulus (Recanzone et al. 1993). However, while the increased cortical area tuned to the conditioned frequency was correlated with behavioral gains, tuning curve sharpening was not (Recanzone et al. 1993).

Taken together, proponents of the primary cortex hypothesis theorized that visual perceptual learning would lead to cortical reorganization or changes in tuning properties in V1, as had been observed in the auditory and somatosensory modalities. Yet, as described in the previous section, electrophysiology reports of learning-induced plasticity within V1 have been

conflicting, and no plasticity has been observed that is comparable to the degree of behavioral improvement. To further complicate the picture, psychophysicists began to observe not only stimulus specificity, but contextual specificity, in their perceptual learning paradigms (Crist et al., 1997; Fahle and Morgan, 1996). Contextual specificity is at odds with the cortical expansion that was hypothesized, where one would expect the enhancement of stimulus features to lead to performance increases in any task leveraging the same features (Gilbert et al., 2001). Moreover, where perceptual learning in a texture discrimination task studied by Karni & Sagi was one of the most striking examples of specificity, more recent work by the same group suggests that this specificity may have been a result of adaptation rather than learning – when controlling for adaptation, Sagi & colleagues observed generalization (Harris et al., 2012). Finally, the generalizability of perceptual learning, which has now been reported in several studies (Hung and Seitz, 2014; Wang et al., 2012, 2014; Xiao et al., 2008; Zhang et al., 2010a, 2010b), debases the psychoanatomy argument that the substrate of perceptual learning must be V1.

1.2.2 Summary of the primary cortex theory

Though rarely delineated, it's useful to distill two distinct hypotheses from the primary cortex theory: the first is that perceptual learning will induce plasticity in V1, while the second is that this learning-induced plasticity will underlie perceptual gains. Notably, the hypothesis that learning will induce plasticity in V1 is specific to the signal within V1, and does not distinguish between plasticity that occurs within V1 itself versus a change in input drive (Bejjanki et al., 2011). However, the primary cortex theory does predict that learning-induced plasticity will be evident outside the context of the task (Schoups et al., 2001). The available electrophysiological

evidence suggests that perceptual learning can induce plasticity in V1 (Ghose et al., 2002; van Kerkoerle et al., 2018; Schoups et al., 2001), but not to the degree that was predicted by perceptual learning studies in other modalities (Recanzone et al., 1992c, 1993), and there is debate as to whether learning manifests in the tuning properties of single neurons at all (Ghose et al., 2002; Schoups et al., 2001). Significantly, and unlike perceptual learning in other modalities, to date no study has been able to account for behavioral gains using only the observed plasticity in V1.

1.2.3 Reweighting Theory

The functional organization of V1 is particularly high-dimensional, simultaneously encoding orientation, spatial frequency, ocular dominance, and retinotopy in superimposed maps that are thought to optimize uniform feature coverage (Hubel and Wiesel, 1968, 1974, 1977; Nauhaus et al., 2012, 2016; Shmuel and Grinvald, 1996; Swindale et al., 1987, 2000; Tootell et al., 1981). The subsequent series of coding transformations from V1 to IT are also more extensive than the coding transformations within auditory or somatosensory cortex (Young 1993). Therefore, learning-induced cortical remapping like that observed in primary auditory and somatosensory cortex might be more disruptive to visual processing. The problem of how learning should induce plasticity without disturbing the existing functionality of a specialized network has been termed the plasticity-stability dilemma (Dosher and Lu, 2017, 2009). As a possible resolution of this dilemma, Dosher and Lu put forth the reweighting theory (Dosher and Lu, 1998), which posits that the sensory representation of perceptual stimuli remains constant while the feedforward weights to downstream decision units are reweighted to strengthen inputs from the most informative channels. Using a simple computational model

that reflected the tuning properties of V1 neurons and a Hebbian learning rule, they showed that perceptual learning may indeed occur merely by reweighting the most informative channels of stimulus information, rather than by inducing plasticity in the representation itself (Petrov et al., 2005, 2006). The specificity of perceptual gains, then, is posited to arise through the strengthening or weakening of synapses between V1 and downstream decision units, leading to stable tuning properties within the sensory representation and dynamic response properties in the output layer. To account for transfer across retinotopic space, Dosher and Lu later introduced an 'integrated reweighting theory', in which decision units received inputs from both V1 and V4 neurons. Positional uncertainty with respect to the stimulus led to increased weights assigned to V4 inputs, while positional certainty led to increased weights to V1 channels. Thus, their framework could account for both the specificity and generality observed in perceptual learning under different training regimes (Dosher et al., 2013). The reweighting theory has gained considerable influence in the field, with the majority of computational models of perceptual learning being reweighting models (Law and Gold, 2009; Petrov et al., 2005, 2006; Poggio et al., 1992; Sotiropoulos et al., 2011; Vaina et al., 1995; Weiss et al., 1993; Zhaoping et al., 2003).

The theoretical work by Dosher and Lu suggests that the specificity of perceptual learning to stimulus attributes cannot be used to infer a locus of learning-induced plasticity (Dosher and Lu, 2009; Petrov et al., 2005). Instead, the most relevant psychophysical experiments for the reweighting theory are ones in which the visual stimulus remains approximately equivalent between the trained and transfer tasks, while the task itself changes. If performance gains are observed only in the learned context, despite the fact that both tasks

use similar visual stimuli, then perceptual learning cannot be supposed to arise simply through enhancing the sensory representation of the stimulus. Interestingly, context specificity has been observed for three-dot bisection and three-dot Vernier acuity performed in the same retinotopic region, suggesting that, indeed, "leaning does not take place on the first level of common analysis" (Fahle and Morgan, 1996), but rather through reweighting by downstream units. In a more recent psychophysical study, training subjects to perform an orientation discrimination task while interleaving training on a spatial frequency discrimination task enhanced the degree of perceptual learning in both feature domains beyond the gains observed by training on each feature independently (Szpiro et al., 2014). In the context of the reweighting theory, this result suggests that when the trained stimulus is multidimensional in feature space, interleaved training on each stimulus dimension can enhance the ability of downstream decision units to selectively reweight input from neurons that carry the most information about the stimulus.

It's important to emphasize that the reweighting theory does not suggest that V1 is not involved in perceptual learning – quite the opposite, V1 is posited to be essential for perceptual learning in most tasks, since the neurons within V1 will be the most informative, and therefore, their inputs should be weighted most strongly. Furthermore, the reweighting theory does not preclude the possibility that perceptual learning will induce plasticity in V1. By pointing to the inadequacy of psychophysical experiments for localizing perceptual learning, as well as by demonstrating that reweighting could account for perceptual gains through a simple computational model, Dosher and Lu simply argue that plasticity in V1 itself is not necessary for

perceptual gains, and moreover, implementing perceptual learning as reweighting is advantageous for maintaining functional stability.

The reweighting hypothesis is a useful framework for interpreting the electrophysiology studies of perceptual learning that find little to no tuning plasticity in V1 neurons (Crist et al., 2001; Ghose et al., 2002; Schoups et al., 2001), as well as the finding that, although there is substantially more plasticity within V4, this plasticity on its own cannot explain behavioral gains either (Raiguel et al., 2006; Yang and Maunsell, 2004). Yet, perhaps the strongest physiological evidence in favor of the reweighting hypothesis is the finding that training on a motion discrimination task leads to plasticity in the responses of LIP neurons, but not in the responses of MT neurons (Law and Gold, 2008). These findings are significant, because neurons in LIP are thought to be responsible for the transformation of motion information into choice-driven motor output (Roitman and Shadlen, 2002; Shadlen and Newsome, 2001), while neurons in MT are thought to only represent motion information about the visual stimulus. Moreover, although the response properties of neurons in MT did not change with learning, the trial to trial variability of the most sensitive neurons in MT became increasingly predictive of the monkey's choice. This analysis, called choice probability, suggests that read out from these neurons by downstream decision units was enhanced with training. The authors further demonstrate that their data can be explained by a reweighting model which uses a reinforcement learning rule (Law and Gold, 2009). In this model, learning proceeds in two phases: first, functional connections are established between a decision-making population of neurons in LIP and sensory input from MT. This accounts for early task learning. Subsequently, these connections are refined to selectively weight the most informative channels.

1.2.4 Summary of the reweighting theory

Central to the reweighting theory is the "plasticity-stability dilemma", which is the idea that perceptual learning should preserve the existing functionality of the network wherever possible. To achieve this, perceptual learning may be a process of reweighting the most informative units – thereby requiring little to no change in the sensory representation itself, but rather enhancing the most informative units of the network. The premises of the reweighting theory are supported by the finding that perceptual learning induces little plasticity within V1 (Crist et al., 2001; Ghose et al., 2002; Schoups et al., 2001) or MT (Law and Gold, 2008), and insufficient plasticity to account for perceptual gains in V4 (Raiguel et al., 2006; Yang and Maunsell, 2004). Moreover, the behavioral result that perceptual learning can show specificity for context despite overlapping sensory features (Fahle and Morgan, 1996) further suggests that plasticity in the sensory representation of the trained stimulus is at least, on its own, inadequate to account for perceptual learning. Yet, evaluating the reweighting hypothesis necessitates recording from multiple brain areas, spanning both sensory and decision neural populations, as well as monitoring the connections between neurons across areas. Thus, the finding that LIP exhibits plasticity that correlates with behavioral gains and reflects enhanced readout from MT, while MT neurons exhibit stable responses (Law and Gold, 2008, 2009), critically advances the case for the reweighting theory.

However, an analogous study investigating the ability of macaques to discriminate coarse orientation differences masked by noise found significant plasticity in V4 (Adab and Vogels, 2011), which is considered a similarly intermediate area along the ventral pathway to MT in the dorsal pathway. Why perceptual learning would induce substantial plasticity in V4

and not in MT for analogous tasks is not addressed by the reweighting theory. In fact, the plasticity that has been observed in V4, and to a lesser extent V1, is paradoxical from the perspective of the reweighting theory: if reweighting is sufficient for perceptual learning, and if there exists a plasticity-stability dilemma, why would plasticity ever be observed in the sensory representation itself?

1.2.5 Reverse Hierarchy Theory

The reverse hierarchy theory (Ahissar and Hochstein, 1997, 2004) offers a partial answer to the question of why perceptual learning might induce plasticity in V1, and more so in V4, by extending the reweighting theory to a hierarchical model of visual processing. Specifically, the reverse hierarchy theory supposes that visual information must pass through a series of visual areas before reaching decision units. As a consequence, if the task requires the precision of neurons in a low-level visual area such as V1, then changing the inputs of those neurons will, in turn, affect the tuning of neurons in the next processing stage that pools from V1 neurons. This process will ripple through the network, such that neurons at the latest stages of processing will exhibit the greatest degree of plasticity. This seemingly simple idea is actually quite radical from the perspective of the primary cortex theory, where the notion that the area least sensitive to task-relevant stimuli would undergo the most plasticity would be paradoxical. The reverse hierarchy theory therefore contributes a foundational insight – that the extent of plasticity observed in the area is dissociable from how much the area contributes to the task.

Yet, the reverse hierarchy theory does not merely extend the reweighting theory to a hierarchical network. More specifically, the reverse hierarchy theory makes predictions about how learning should unfold, as a function of time and task difficulty. As reflected in the name,

the reverse hierarchy theory hypothesizes that the process of selectively reweighting the most informative inputs occurs as a cascade from top to bottom. More precisely, let H_i denote a particular stage of the visual hierarchy, indexed by *i*, with *i* increasing hierarchically. The reverse hierarchy theory first posits that the first neurons to be selectively reweighted by decision units are those at the last stage of visual processing. Then, as the most informative neurons within H_i are selectively enhanced, subsequently, the inputs from H_{i-1} to the most informative neurons in H_i will also be enhanced, and this process will proceed as a cascade down the hierarchy as learning and task difficulty progress.

The building blocks of the reverse hierarchy theory's central argument are the findings that training on an easy task leads to more transfer of perceptual gains (Ahissar and Hochstein, 1997), and facilitates learning of a more difficult discrimination task (Ahissar and Hochstein, 1997; Liu and Weinshall, 2000; Rubin et al., 1997). Since performance gains following learning an easy task generalize across stimulus features while performance gains following learning a difficult task are specific to the trained features, easy tasks must induce selective reweighting at an intermediate or late stage of visual processing where neurons' receptive field properties are correspondingly broad, while difficult tasks must induce plasticity where receptive fields are correspondingly selective for the trained visual features. Moreover, because easy tasks are learned more quickly than difficult discrimination tasks, and because learning an easy task facilitates learning of a more difficult task, the reverse hierarchy theory posits that perceptual learning should first reweight the inputs of late stages of visual processing, and then this plasticity should subsequently direct which units are reweighted at progressively lower stages of processing (Ahissar and Hochstein, 2004).

The reverse hierarchy theory offers powerful insight into the otherwise puzzling findings that V4 exhibits greater plasticity than V1 for fine orientation discrimination tasks (Raiguel et al., 2006; Yang and Maunsell, 2004), as well as the finding that the distribution of orientation tuning preferences changes more in PIT than in V4 for coarse orientation discrimination tasks (Adab and Vogels, 2011; Adab et al., 2014) despite V1 and V4 neurons being more informative. Moreover, the conflicting findings with respect to learning-induced plasticity in V1 might also be accounted for by the reverse hierarchy theory, considering that Schoups and colleagues trained monkeys on a task with more stable stimulus properties than Ghose and colleagues, and their monkeys achieved lower perceptual thresholds (Ghose et al., 2002; Schoups et al., 2001; Wenliang and Seitz, 2018). However, the theory's predictions with respect to the sequences of learning-induced plasticity have been understudied. The intuition that the sensory representation weighted most strongly by downstream decision units might change locus over the course of learning has some support from inactivation studies in MT (Chowdhury and DeAngelis, 2008; Liu and Pack, 2017). Chowdhury and DeAngelis showed that the performance of monkeys trained exclusively on a coarse depth perception task was severely diminished following reversible inactivation of MT, yet, after continued training on a fine depth discrimination task, coarse depth perception was no longer dependent on MT. Liu and Pack showed a similar result for motion direction discrimination. Monkeys trained on a direction discrimination task using low contrast drifting gratings initially did not exhibit performance deficits when MT was inactivated. However, after training on a motion discrimination task with random dot stimuli, MT inactivation devastated performance on the grating motion task. Notably, the tuning properties of MT neurons remained stable, but choice probability analysis

revealed that the most sensitive neurons in MT became increasingly predictive of the monkey's choice. Furthermore, the extent of spatial integration – the inflection point at which increasing the size of the stimulus no longer enhanced performance – was approximately doubled after training on the dot motion task, suggesting that the relevant sensory neurons had larger receptive fields. Taken together, Liu and Pack's results strongly suggest that the sensory input weighted most strongly by downstream integrator neurons had shifted from a low-level area to MT.

Although the results from Chowdhury and DeAngelis, and Liu and Pack, make the compelling argument that the locus of sensory input to decision units can change with learning, neither result fully tests the predictions of the reverse hierarchy theory. For one, neither study explicitly studied perceptual learning, since neither study investigated the extent to which the subject's ability to perceive differences between visual stimuli improved with prolonged practice. Thus, whether the sensory neurons weighed most strongly changes over the course of perceptual learning is still unknown. Moreover, the reverse hierarchy theory not only predicts that the locus of neurons most informative to the decision will shift with task demands, but further, that the neurons which were most informative at a higher hierarchical stage will influence which neurons are reweighted at lower levels. This idea rests on the foundational premise that the visual stimuli are processed through a hierarchy to begin with, and more specifically, that the hierarchy of visual processing is consistent between the trained tasks. In Chowdhury and DeAngelis' work, it's clear that this premise was not met: coarse depth perception is thought to be processed in the dorsal stream, while fine depth perception is thought to be processed in the ventral stream (Umeda et al., 2007). Thus, sequential training on

a coarse then fine depth discrimination task may have involved a cross over between similarly intermediate areas in the two streams. Meanwhile, Liu and Pack's experimental design investigates whether the sensory representation underlying perceptual decision making can move up, rather than down, the hierarchy, a scenario for which the reverse hierarchy theory makes no specific predictions.

There is, perhaps, a deeper challenge to evaluating the reverse hierarchy theory other than observing that previous studies have been scant or inadequate. Although the ripple of reweighting through the visual hierarchy might be experimentally observable (Adab and Vogels, 2011; Adab et al., 2014; Raiguel et al., 2006; Yang and Maunsell, 2004), the specific hypothesis that plasticity induced by learning an easy task should subsequently direct plasticity induced by learning a difficult task, theoretically along the reverse hierarchy, is extremely difficult to test experimentally, for it both requires recordings from multiple brain areas while simultaneously monitoring shifts in synaptic weights to particular neurons. Nevertheless, the simpler hypothesis - that late stages of visual processing will undergo feedforward plasticity before earlier stages, as a function of time and task difficulty - is one that could be tested with a longitudinal study of perceptual learning that recorded from multiple brain areas, and evaluated the relationship between neural tuning and choice probability.

1.2.6 Summary of the reverse hierarchy theory

The reverse hierarchy theory is a powerful model in the field of visual perceptual learning, most notably because it makes clear predictions for how perceptual learning should manifest in a hierarchical network and how it should unfold in time. While some of its specific hypotheses are extremely challenging to test in cortex, and although other hypotheses have simply not yet

been tested, the fact remains that the reverse hierarchy theory is able to explain the majority of key electrophysiology studies in the field of visual perceptual learning, particularly those findings for which neither the primary cortex theory nor the reweighting theory could account (Adab and Vogels, 2011; Adab et al., 2014; Ghose et al., 2002; Raiguel et al., 2006; Schoups et al., 2001; Yang and Maunsell, 2004).

1.2.7 Dual-plasticity model

By postulating that learning-induced plasticity will selectively enhance input from neurons that are the most informative to the behavioral task, both the reweighting theory and the reverse hierarchy theory make an implicit assumption with respect to the underlying plasticity mechanism: namely, that learning-induced plasticity is task-specific, and therefore affects only the neurons that are connected to decision units for the task at hand. Though the details of how learning-induced plasticity is actualized have been modeled different ways, with varying degrees of supervision and different weight-update rules (Law and Gold, 2009; Petrov et al., 2005, 2006; Sotiropoulos et al., 2011; Vaina et al., 1995; Zhaoping et al., 2003), the association between the sensory representation and the decision unit is essential in all of these models. However, there is an alternative hypothesis, which is that the sensory representation might first be enhanced by a diffuse, global reinforcement signal to all active neurons, and then further refined by task demands (Watanabe and Sasaki, 2015). This idea has been termed the 'dual-plasticity' model, as it posits that perceptual learning should induce both feature-based and task-relevant plasticity (Watanabe and Sasaki, 2015).

The motivation for this hypothesis arises from a series of studies evaluating the effects of exposing subjects to a task-irrelevant stimulus while they train on a perceptual task. Watanabe and colleagues have demonstrated that subjects exhibit both task-relevant and task-irrelevant learning in this context (Watanabe et al., 2001), a finding which has also been demonstrated by another group (Rosenthal and Humphreys, 2010). Watanabe and colleagues further demonstrate that task-irrelevant learning only occurs in the presence of reinforcement (Seitz and Watanabe, 2003; Seitz et al., 2009), and only if the features of the irrelevant stimulus are weakly detectable without selective attention or training (Tsushima et al., 2008).

1.2.8 Summary of the Dual-Plasticity model

Watanabe and colleagues contend that the dual-plasticity model is a parsimonious model, which reconciles the observed plasticity in low-level sensory areas as well as high-level decision areas. Arguably, it also offers a useful hypothesis for the mechanism of learning-induced plasticity, which has hitherto been modeled in a variety of ways. However, the utility of the dual-plasticity model is weaker than other theoretical frameworks. Aside from being a catch-all, umbrella model for all preceding models, it does not address any new or unresolved tension in the field of perceptual learning - except the phenomenon of task-irrelevant learning. Given that task-irrelevant learning only occurs with reinforcement while perceptual learning can occur without feedback (Ball and Sekuler, 1987; Crist et al., 1997; Fahle and Edelman, 1993; Karni and Sagi, 1991; Mckee and Westheimer, 1978; Shiu and Pashler, 1992), task-irrelevant learning is likely not a general feature of perceptual learning. Furthermore, the dual-plasticity model is broad enough so as to be difficult to refute. By contrast, the primary visual cortex theory, though waning in its explanatory power, was fundamental to advancing the field of perceptual

learning precisely because it offered testable predictions that could be refuted by neurophysiology studies. Nonetheless, the fact that the dual-plasticity model still wields influence in the field does suggest that the question of whether perceptual learning induces a representational change in low-level visual areas has not been satisfactorily resolved by other models.

1.3 Motivation and summary of chapters

The primary cortex theory, the reweighting theory, and the reverse hierarchy theory have each significantly advanced the field of visual perceptual learning. The primary cortex theory led to the important observations that the tuning curves of neurons may be sharpened at the trained stimulus (Schoups et al., 2001), and that the axonal arbors of V1 neurons can undergo substantial remodeling following learning of a contour detection task (van Kerkoerle et al., 2018). These findings demonstrated that, as predicted, perceptual learning can induce plasticity within V1. Yet, equally valuable have been the moments where the primary cortex theory has failed – notably, the finding that V1 neurons do not increase their representation, nor their response amplitude to the trained stimulus, and that changes in the slope of V1 neurons are neither sufficient to explain behavioral gains nor observed in all paradigms (Ghose et al., 2002). The limitations of the primary cortex theory have pushed the field to consider that perceptual learning could leave the sensory representation of the stimulus largely intact, and instead lead to selective reweighting of the most informative channels. This idea motivated valuable work investigating the way that choice probabilities evolve with learning (Law and Gold, 2009), and the extension of this idea to consider the effects of reweighting through a hierarchical network

can offer valuable insight into why V4 and even PIT might exhibit a greater degree of plasticity than V1, though V1 is most informative for the task.

1.3.1 Perceptual learning & population coding in V1

Yet, despite significant progress, learning-induced plasticity within V1 remains unexplained: primary cortical theorists cannot account for why V1 plasticity falls short of perceptual gains, while reweighting theorists cannot account for why V1 plasticity occurs at all. What's missing? Here, history may offer some insight. The field of perceptual learning was transformed by single-unit recordings of the properties of V1 neurons, much in line with the emergent 'neuron-doctrine for perceptual psychology' (Barlow, 1972). The primary cortex theory, having its roots in the era of single-unit physiology, implicitly postulates that the single neuron is the fundamental basis unit for perception, and thus, the population response is simply the sum of its component neurons. Yet, the development of technology that allows physiologists to collect data from populations of neurons simultaneously is leading to a paradigm shift towards viewing the activity of a population of neurons as an irreducible unit of perception in its own right. Ni and colleagues have recently made this argument within the field of perceptual learning, by demonstrating that choice probability exhibited a relationship with the shared variability within a population of V4 neurons (Ni et al., 2018). Relatedly, Peters and colleagues have shown that in mice that undergo motor learning, the spatiotemporal activity patterns of a population of motor cortical neurons become more stereotyped with learning, and this reproducibility is correlated with learned behavior (Peters et al., 2014). It might be that the code for perceptual learning is similarly distributed in V1. Such a population-level code would have the advantage of being minimally disruptive to the existing functionality of the

network, and could be shaped through learning without necessitating dramatic shifts in orientation tuning of individual neurons. Decision units might learn not simply to reweight the most informative neurons, but rather to integrate population responses that are spatiotemporally distinct.

Two-photon imaging is particularly valuable for testing V1 population-coding hypotheses of visual perceptual learning, since it is both temporally and spatially precise. Moreover, chronic two-photon imaging affords the opportunity to collect data from the same cells across days, weeks, or possibly even months (Chen et al., 2013b). This provides the opportunity to investigate not only the V1 population activity patterns that evolve with learning, but also the stability of the feature maps within V1 through learning. Investigating feature map dynamics or stability would be particularly interesting given the finding that perceptual learning affects BOLD responses in V1 differently depending on the stage of learning (Yotsumoto et al., 2008). Moreover, transient cortical map expansion has been shown to facilitate early perceptual learning in auditory cortex, and performance gains remained stable after map renormalization (Reed et al., 2011). Therefore, the first part of this thesis documents the development of chronic two-photon imaging techniques for studying perceptual learning in V1.

Chronic two-photon imaging that can be used while the animal is performing a visual perceptual learning task requires careful consideration of animal model. We contend that the ferret is uniquely well-suited for the study of perceptual learning using chronic two-photon imaging. Like the cat and primate, the ferret's primary visual cortex has been shown to exhibit maps for orientation, spatial frequency, and ocular dominance (Chapman et al., 1996; Redies et

al., 1990; Yu et al., 2005), and these maps have further been shown to be organized in a way that maintains a uniform gradient of multidimensional feature coverage across cortical space, with orthogonal relationships between feature maps at high gradient junctions (Yu et al., 2005). At the same time, ferrets are amenable to virally-mediated GCaMP6f expression, and their small body size is advantageous for stabilizing the brain while imaging. Given the apparent advantages to performing chronic two-photon imaging in ferrets, in chapter 2 we assess their visual behavioral capabilities. Ferrets proved to be strong behavioral subjects, able to perform both simple orientation discrimination tasks and more complex motion and form integration tasks with a high degree of accuracy (90% or above on the easiest condition), and their performance was well-described by standard psychometric functions. In order to perform neural recordings while the animal performs a task, we develop a novel head-fixed behavioral setup and training sequence that could be used in conjunction with two-photon imaging. Next in chapter 3, we develop a chronic two-photon imaging implant that may be used in the adult ferret. We demonstrate the stability and optical clarity of this implant, as well as the ability to visualize cells for nine weeks. Together, these chapters open a new avenue for exploring population-level effects of perceptual learning in V1.

1.3.2 Perceptual learning across the visual hierarchy

While investigating the evolution of population activity in V1 with chronic two-photon imaging will be a valuable extension of the existing literature on learning-induced plasticity within V1, the available data suggest that perceptual learning ultimately affects multiple stages of visual processing (Maniglia and Seitz, 2018). The best theoretical framework that we have to understand the far-reaching consequences of perceptual learning is the reverse hierarchy

theory, which posits that reweighting low-level inputs causes a cascade of tuning plasticity throughout the visual hierarchy. However, in order to investigate the degree to which low level inputs are reweighted, and the impact of reweighting across the visual hierarchy, it would be necessary to monitor synaptic weights between neurons at network scale.

As before, new investigative tools might offer new insight. In particular, the emergence of deep convolutional neural networks as a model for visual cortex offers the opportunity to evaluate the effects of visual perceptual learning on the tuning properties and weighted connections of all of the neurons in the network. Convolutional neural networks are loosely inspired by the transformation from simple cells to complex cells observed by Hubel and Wiesel (Hubel and Wiesel, 1962), where simple cells are thought to act as a linear filter on their inputs, and the layer above pools across a cluster of neurons that are nearby in space in a nonlinear fashion (Lindsay, 2020; Movshon et al., 1978a, 1978b; Rawat and Wang, 2017). Each neuron in a convolutional neural network is defined by its spatial receptive field, and the particular convolutional filter it applies to its inputs. The same convolutional filter is applied everywhere in space, such that each unique filter defines a feature map over the input image. The output of the convolutional filter on its inputs is passed through a rectifying nonlinearity, and the maximum activity is taken over a small region of space to achieve spatial compression. This simple set of operations – filtering, rectifying, and pooling – compose a convolutional layer, and stacking multiple layers together hierarchically creates a deep convolutional neural network.

Remarkably, the layer-wise feature transformations that develop in deep convolutional neural networks with training have been shown to be similar to the ventral stream. More precisely, the feature maps of convolutional layer 1 have been shown to strongly resemble the

tuning properties of V1 neurons (Krizhevsky et al., 2012), while the increasing complexity of feature coding across layers (Zeiler and Fergus, 2013) has been shown to predict the gradient of complexity of neural responses across areas as measured by fMRI (Güçlü and van Gerven, 2015). Moreover, the tuning properties of intermediate layers have been shown to correspond to the tuning properties of V4 neurons (Pospisil et al., 2018), as well as population coding of V4 and IT (Yamins et al., 2014), (for review see Lindsay, 2020). Of particular interest is that a deep convolutional neural network has also been shown to replicate many of the psychophysical and neurophysiological findings in the field of visual perceptual learning (Wenliang and Seitz, 2018). Taken together, these findings render deep convolutional neural networks as advantageous models for investigating the effects of visual perceptual learning across multiple stages of processing.

Therefore, chapter 4 of this thesis leverages a deep neural network to investigate the cascading effects of visual perceptual learning through a hierarchy of visual processing stages. We show that, rather than what has previously been supposed by the reverse hierarchy theory, task difficulty does not affect which layers of the network undergo the most plasticity, but instead influences the breadth of the population of neurons that contribute evidence to the classification. Additionally, we show that training on an easy task before training on a difficult task enhanced the read out from low-level inputs in subtle, distributed ways. Generally, we show that tuning plasticity increases hierarchically with learning in a way that is biased towards the trained feature, while at the same we show that the network's sensitivity to the trained stimuli depends most critically on the reweighting of mid and low-level inputs. Thus, our work contributes a valuable link between physiology data and the mechanistic explanation provided

by the reverse hierarchy theory. To our knowledge, this work provides the first comprehensive assessment of the reverse hierarchy theory in a computational model. More broadly, this work highlights the importance of considering learning-induced plasticity in a hierarchical context.

Finally, chapter 5 offers a reflection on the direction of the field of visual perceptual learning, the necessity for nuanced population level analyses, and the utility, as well as limitations, of the techniques offered in this dissertation.

2 Visual behavioral capabilities of the ferret

This chapter has been published:

Dunn-Weiss, E., Nummela, S.U., Lempel, A.A., Law, J.M., Ledley, J., Salvino, P., and Nielsen, K.J. (2019). Visual Motion and Form Integration in the Behaving Ferret. Eneuro *6*, ENEURO.0228-19.2019.

2.1 Introduction

Because of their early parturition, ferrets are uniquely suited for developmental research. Indeed, research in ferrets has contributed significantly to our understanding of the development of early visual stages (Sharma and Sur, 2014). In contrast, higher-level visual areas have received little attention in this species, even in adult animals. Behaviorally, ferrets have been shown to be capable of basic object discrimination and motion detection tasks (Doty et al., 1967; Hupfeld et al., 2006). Anatomically, ferrets have a relatively large visual system with about 19 areas (Homman-Ludiye et al., 2010), suggesting extensive processing of visual information beyond primary visual cortex. Consistent with this notion, we have recently demonstrated that one of these areas – area PSS (Philipp et al., 2006) – can be considered a higher-level motion area comparable to primate MT (Lempel and Nielsen, 2019). These findings suggest the feasibility of studying higher-level vision in ferrets, which would significantly enhance our ability to investigate its development. To further establish higher-level vision research in ferrets, we addressed two central aspects here: First, we used behavioral experiments to investigate whether ferrets are able to integrate motion and form signals, functions that are usually associated with higher-level visual areas (Ungerleider and Pasternak, 2004). Second, we tested whether PSS responses are consistent with the behaviorally observed motion integration.

Following established methods, we tested behavioral and neural motion integration using RDK (Figure 2.1). These stimuli consist of randomly placed dots, each of which can either move in a global direction (signal dots), or in a randomly chosen alternate direction (noise dots). Integration over the signal dots results in the perception of a coherently moving pattern,

the strength of which depends on the ratio of signal and noise dots (the so-called coherence level). Form integration was tested with a very similar stimulus, static Glass patterns (Glass, 1969; Glass and Pérez, 1973). These patterns are constructed from randomly distributed dot pairs (Figure 2.1). For signal dot pairs, the axis connecting the dots is oriented along a set orientation; noise pairs have a random orientation. Integration across signal pairs then reveals a global pattern, with a strength that is again determined by the coherence level.

We chose RDK and Glass patterns because they complement each other well: Processing of complex motion and form information has been associated with different visual streams in non-human primates and humans (Ungerleider and Pasternak, 2004). Yet, both stimulus types are constructed from the same elements, and can be used for quantitative measurements of integration thresholds in a highly comparable manner. In addition, both RDK and Glass patterns have been used to study the development of motion and form vision in monkeys and humans (for reviews, see Grinter et al., 2010; Kiorpes, 2016; Maurer and Lewis, 2018). Testing ferrets on RDK and Glass patterns therefore not only allows a comparison of their motion and form vision capabilities, but also provides a useful starting point for future developmental research.

Since very few visual behavioral experiments have been performed in ferrets (Doty et al., 1967; Hollensteiner, 2015; Hupfeld et al., 2006, 2007; von Melchner et al., 2000; Pollard et al., 1967; Pontenagel and Schmidt, 1980), testing their motion and form integration capacities required the development of appropriate behavioral paradigms. Here, we established a freely-moving paradigm and a head-fixed paradigm with greater control over viewing conditions. Using these paradigms, we found that ferrets show clear signs of motion and form integration. In general, ferrets were good subjects for visual psychophysics, performing tasks with low lapse

rates, and behavior that could be well described by standard psychometric functions. Furthermore, we found behavioral limits of motion integration to be in close agreement with limits imposed by responses of PSS neurons, consistent with an involvement of higher-level visual areas in these tasks. In summary, our data establish the ferret as a viable animal model for studying more complex visual processes like motion and form integration.

2.2 Methods

2.2.1 Animals

All procedures were conducted in accordance with guidelines of the National institutes of Health and were approved by the Animal Care and Use Committee (ACUC) at Johns Hopkins University. A total of six adult female ferrets aged 5 - 50 months at the start of the experiments were used for the behavioral experiments. Each ferret participated in 1 - 3 studies of 1 - 4 months each (see Table 2.1 for the tasks each ferret participated in and their sequence). An additional three female ferrets and one male ferret aged 2 - 12 months were used for electrophysiology recordings. Our previous experiments have shown no difference in PSS motion integration in this age group (Lempel and Nielsen, 2019).

Ferret	Acuity	Dots	Glass
F0	X	X	X
F4	X	X	
F2	X		
F6		X	X
F8		X	
F9		X	

Table 2.1 Tasks that each ferret performed. *All ferrets learned the acuity task followed by the RDK task and then the Glass pattern task.*

2.2.2 Freely-moving behavior: Design

Freely-moving setup

The behavioral box used for freely-moving behavioral tasks measured 100 cm long x 70 cm wide x 60 cm tall (Figure 2.1A). The walls and the floor of the box were painted black, and the box did not have a ceiling. The behavior box was enclosed in its own room such that the ambient light and noise level could be controlled. A webcam (Logitech) affixed above the box was used to observe the ferret while performing the task. A cut-out within one of the short walls of the box accommodated a 24 inch VIEWPixx/3D monitor (VPixx) for displaying visual stimuli (refresh rate 120 Hz). Museum glass (True Vue) was placed directly in front of the monitor to protect the screen and minimize reflectance. All stimuli were generated using PsychToolbox (Brainard, 1997; Kleiner,M et al., 2007; Pelli, 1997), and stimulus timing and trial events were controlled by PLDAPS (Eastman, 2012). Two reward ports were positioned to the left and right side of the screen, and a third reward port was positioned in the center of the wall opposite the screen. Reward ports consisted of a metal spout used for reward delivery, surrounded by an infrared (IR) beam emitter and detector (Medical Associates Inc.). Breaks in the IR beam were used to detect port contacts. A fourth IR beam was installed to detect crossing the halfway point between the rear reward point and the monitor. Solenoid valves (Parker Hannifin) were used to dispense water reward.

General task design

All ferrets were trained on two-alternative forced-choice (2AFC) tasks. Preceding a given trial, a red LED was illuminated above the response port opposite the screen, indicating the start of a new trial (see Figure 2.1B for task sequence). Ferrets initiated a trial by activating this

port. Trial initiation was rewarded with a small water reward (~0.05 mL). A stimulus was presented on the monitor immediately after trial initiation, independent of which direction the ferret was facing at the time. With the exception of one RDK control experiment, all stimuli were shown on gray background (50 cd/m^2). Each stimulus was associated with one of the two response ports located on either side of the screen. If the ferret selected the correct port, a high tone (1 s duration) was played through the VIEWPixx speakers and a water reward (~0.2 mL) was dispensed. If the ferret selected the incorrect port, a low tone (1 s duration) was played and no water was dispensed. After an incorrect choice, the ferret was required to activate the correct response port before it could initiate the next trial. Activation of the correct port was rewarded with a small amount of water (10 - 30% of the maximum possible reward size, dependent on the complexity of the task and stage of training). If ferrets demonstrated a significant bias towards one choice port, the amount of water reward dispensed at each port was varied by the experimenter until the ferret sampled both ports evenly.

In general, ferrets performed one session per day for 30 - 45 minutes, or about 100 trials. We imposed no constraints on reaction time (i.e., the time between trial initiation and response port activation), other than ending trials during which the ferret failed to make a choice for a long time (around 120 s), which generally tended to only occur at the end of a testing session when motivation levels were low. Because it took the ferret some time to move between the two ends of the box, the shortest reaction times were around 2 s. In general, reaction time was about 3 s. For all tasks, the stimulus presentation was tied to the reaction time of the animal. More precisely, with the exception of the acuity task, in which the stimulus was removed when the ferrets reached the half-way point between both ends of the box, the

stimulus remained visible until the ferret selected the correct port. In a subset of experiments, we measured both the time of the first response and the time of the correct response. On incorrect trials, the ferret took about 2 s to correct its choice, meaning that the stimulus was presented for a total of about 5 s.

Acuity task: Stimuli, task design, training and animal inclusion criteria

Ferret acuity was assessed with an orientation discrimination task, using horizontal and vertical gratings of different spatial frequencies and contrasts (Figure 2.1 C,D). The contrast of each grating was varied from 0.05 – 0.95 Michelson contrast, and gratings were equiluminant with the background. To limit the effects of changing viewing distance on the spatial frequency of the stimulus, the stimulus was turned off once the ferrets crossed the IR beam at the midpoint of the box. Measured from this point in the box (50 cm from the screen), gratings had a diameter of 33 deg, and a spatial frequency between 0.09 and 0.36 cycles per deg (cpd). Horizontal and vertical gratings were paired with the left and right choice port, respectively. The orientation, spatial frequency, contrast, and phase of the grating were varied pseudorandomly across trials. Five ferrets (F0, F1, F2, F3, F4) were trained on this task. Two ferrets (F1, F3) failed to perform the task above 70% correct at a spatial frequency of 0.36 cpd and were excluded from further analysis.

Motion integration task: Stimuli, task design, training and animal inclusion criteria

Ferrets were trained to discriminate between full-screen RDK with global translational motion to the left or right (Figure 2.1E). RDK remained on the screen for the entire duration between trial initiation and triggering the correct response port. Stimulus metrics below are

given from the back of the box (viewing distance 1 m). RDK measured approximately 38 x 24 deg, and were composed of black and white dots (diameter 1.5 deg) with a density of 0.12 dots/deg. Dot position and color were randomly initialized. Dots were randomly chosen to be signal or noise dots. The coherence parameter determined the percentage of signal dots on each trial, and ranged from 20% - 100%. Motion directions differed between signal and noise dots, but all dots moved at the same speed (also called "Brownian motion" noise; (Pilly and Seitz, 2009; Schütz et al., 2010)). More precisely, signal dots moved in the global stimulus direction (left or right), and noise dots in a direction randomly drawn from a uniform distribution of integers from 0 to 359 deg. On the first frame, each dot was assigned a randomly chosen lifetime that could range from 1 to 240 frames. Lifetime was decreased by one every frame. When the lifetime of a dot reached zero, the dot was probabilistically assigned to be a signal or noise dot according to the coherence parameter, and given a new lifetime of 240 frames. At this time point, noise dots were assigned new motion directions, drawn from the same uniform distribution as before. Dots that moved off-screen were re-plotted in a random position on the side of the screen opposite their direction of motion. This wrap-around was designed to maintain constant dot density. In addition, random repositioning after wrap-around and variable dot lifetime limited the subject's ability to infer the direction of coherent motion from a single dot in isolation.

Prior to training on the full motion integration task, ferrets were trained to associate a 100% coherent stimulus moving towards the right with reward at the right port, and a leftwards moving stimulus with the left port. Once ferrets mastered this task (performance at or above 95% correct for at least two consecutive sessions), increasingly lower coherence levels were

introduced systematically across days. Three ferrets (F0, F4 and F6) were trained in this manner, and all three successfully learned the task. After completion of training, psychometric motion integration functions were measured by varying coherence level and direction pseudorandomly from trial to trial. Dot speed was kept constant in each session. Different dot speeds were explored in different blocks of sessions (i.e. a new speed was tested after completion of tests with the previous one). Across blocks, speeds of 24 deg/s, 48 deg/s, and 72 deg/s (measured from the back of the box) were tested.

We ran a number of control experiments on individual ferrets (one ferret per experiment). In the first (ferret F4), we tested the impact of speed more directly by fixing the coherence at 60%, and varying dot speed pseudorandomly from 6 – 144 deg/s. In a second control experiment (ferret F0), we investigated the impact of dot lifetime by randomly setting maximum dot lifetime to either 240 or 3 frames on any given trial. In the third control experiment (ferret F6), we tested the influence of dot color by using only white dots on a black background.

Form integration task: Stimuli, task design, training and animal inclusion criteria

Ferrets were trained to discriminate static linear Glass patterns based on their orientation (horizontal or vertical). As for the RDK task, stimuli remained on the screen for the entire trial duration, and stimulus parameters are given from a position in the last quarter of the box, assuming that ferrets made their decision after having turned around from the initiation port (viewing distance 75 cm). Stimuli covered the entire extent of the screen (38 x 24 deg). Each stimulus was composed of 200 - 250 white dot pairs (dot diameter 0.7 deg), with a distance of 1.2 deg between the dots in a pair. The position of all dot pairs was randomly

initialized. At 100% coherence, all dot pairs were oriented either horizontally or vertically to create the global percept of a linear pattern (Figure 2.1F). At lower coherences, dot pairs were randomly assigned to be signal or noise pairs, with the percentage of signal pairs determined by the coherence parameter. Noise pairs were assigned a random orientation drawn from a uniform distribution of integers from 0 to 359 deg. Ferrets began training on the task with fully coherent patterns until performance was at or above 85% for two consecutive sessions. At this point, increasingly lower coherence levels were gradually introduced. In the full task, coherence varied from 20% to 100%. Both the coherence level and the orientation of the glass pattern varied pseudorandomly from trial to trial. Two ferrets (F0, F6) were trained on this on this task, and learned it successfully.

2.2.3 Head-fixed behavior

Head-fixed setup

The head-fixed setup consisted of a head-post holder, body holder, and reward delivery system (see Figure 2.4A & B). The body holder was a custom-made plastic box with adjustable sides that ferrets could comfortably fit in, but that restricted their body movements (28.5 cm long, 10 cm wide, 10 cm tall; see Dobbins et al., 2007 for a similar design). The head-post holder allowed stabilization of the animal's head by means of a head-post. This head-post was anchored in an acrylic cap attached to the skull with screws, which was implanted in an aseptic procedure under isoflurane anesthesia. The head-post holder height and position was custom to each ferret to ensure an ergonomic position.

The reward delivery system consisted of three spouts: two choice spouts, positioned 12 mm apart, and a neutral central spout that could be used for trial initiation (see Marbach and Zador, 2017 for a similar design for mice). The spouts were made from metal tubes (1 mm in diameter) bent into the correct shape. Licks were detected as changes in capacitance using an Arduino Uno board (Arduino) and the Arduino capacitive-sensing library. The spouts were electrically isolated from the rest of the setup. Each spout was mounted onto a pneumatic cylinder (McMaster-Carr), which used compressed air to retract and propel the spouts. This allowed each spout to assume two positions, one close to the animal, and one out of reach. The two choice spouts were additionally mounted on small translation stages (Newport) to control the distance between spouts. Finally, all spouts, along with the pneumatic cylinders, were mounted on a larger translation stage (Newport) to customize the distance of the spouts relative to the ferret. Solenoid valves (Parker Hannifin) were used to dispense water reward.

Stimuli were shown on the same VIEWPixx/3D monitor used in the freely-moving setup, which was placed 45 cm in front of the head-fixed setup. Stimuli again were generated using the PsychToolbox, and presentation was controlled using PLDAPS. We did not monitor eye movements during task performance for the data presented in this paper.

Task design for head-fixed paradigm

Ferrets were acclimated to the setup by receiving free water reward from each of the spouts while being head restrained. They were also permitted to freely move in and around the setup while the spouts were in motion to get comfortable with the noise of the gas pistons. This acclimation period lasted about three days. During this time, the position of the head-post

holder and the spouts (relative to the ferret) were adjusted to optimize each animal's position and access to the spouts.

Each training session was preceded by a short calibration phase (20 trials) during which the ferret was presented with a single choice spout at a time and no visual stimulus. This calibration period served to ensure that both choice spouts were treated equally by the ferret, which helped to lower response biases. How the ferret valued each spout was estimated by the lick frequency on that spout. The head-post position and the amount of water delivered on each spout were adjusted until the ferret demonstrated approximately equal lick frequency on each spout.

Two ferrets were trained on a head-fixed 2AFC task using RDK generated identically to the freely-moving paradigm. As before, RDK could move horizontally to the left or right, and ferrets had to respond to each motion direction by licking one of the two choice spouts. Each trial in the task began with an initiation phase (see below), followed by stimulus presentation (see Figure 2.4C for task sequence). Following a 200-300 ms delay, the two choice spouts were then moved close the animal, which had to lick one of them to indicate its choice. As for the freely-moving paradigm, no constraints were imposed on reaction time. In general, the first spout contact occurred after about 650 ms from stimulus onset (i.e., within 350 to 450 ms from spout availability). If the ferret made the correct choice, the incorrect spout was retracted, and the ferret collected the full possible reward (~ 0.15 mL) from the correct spout. Instead of delivering the entire amount of water at once, we divided it into a series of smaller rewards (~30 µL per lick), and delivered the entire amount over a series of licks. The total amount of water per correct trial was controlled by limiting how long the spout was available to the ferret

(1.5 s, or about 5 licks). We chose this reward strategy because ferrets tended to spill less of the smaller drops, allowing better control over reward amounts per trial. If the ferret selected the incorrect spout, it was immediately retracted, and the ferret had to correct its choice by licking the correct spout for a single drop of water (~30 µL) before moving on to the next trial. A high tone was paired with correct choices, and a low tone was paired with incorrect choices. The stimulus remained on the screen until the ferret selected the correct spout (in general, it took ferrets an additional 1 s to correct an incorrect choice). If a ferret demonstrated a significant bias towards one response port, the amount of water reward dispensed at each port was varied by the experimenter until the ferret sampled both ports more evenly.

Trial initiation differed between the two ferrets. For F9, trials were passively initiated. After the inter-trial interval (ITI), the stimulus appeared on the screen and the two choice spouts were presented. For F8, trials were actively initiated. In this case, a white square (3 x 3 deg) was presented in the center of the screen after the ITI, and the central spout was moved forward. When licks were detected on this spout, the trial began: The center spout was retracted, the stimulus appeared on the screen, and the two choice spouts were presented. Licks on the center spout were rewarded with a small amount of water (about 30 µL, divided into 2 – 3 licks performed during 0.5 s).

Prior to testing animals on the full motion discrimination task, ferrets were trained to associate 100% coherent RDK moving towards the right with reward at the right spout, and leftward RDK with reward at the left spout. Ferrets were introduced to this task by adding a fraction of instructive trials, in which only the correct spout was presented. This fraction was manually reduced both within and across sessions by the experimenter to maintain an overall

minimum reward rate of 75 - 80%, which ensured a high level of motivation to perform the task. Once ferrets performed the task at or above 90% correct with no instructive trials, increasingly lower coherence levels were gradually introduced across days. The full task used coherence levels from 20 - 100%. For F9, trials at 100% coherence were doubly represented and instructed 50% of the time, which served to increase the overall reward rate and maintain a higher motivation level. Therefore, the number of uninstructed trials at 100% coherence was the same as the number of trials at every other coherence level, and the overall fraction of instructive trials was ~14%. Instructed trials were excluded from further analysis. For F8, no trials at any coherence level were instructed, and all coherence levels were presented equally often. Coherence level and direction of motion varied pseudorandomly from trial to trial. Dot speed was fixed at 72 deg/s. The total number of trials per session that ferrets performed in the head-fixed setup was generally higher than the freely-moving behavior, but also more variable per ferret. In general (including initial training sessions at 100% coherence only), F8 would perform about 200 - 500 trials, while F9 would perform about 100 - 150 trials.

2.2.4 Behavioral data: Analysis and statistics

All data analysis was performed in MATLAB (The Mathworks). Data was concatenated across sessions for which the ferret performed at least 70 trials in the freely-moving paradigm and at least 100 trials in the head-fixed paradigm (see Tables 2.2 and 2.3 for a summary of number of trials and sessions for each analysis). This criterion was imposed because behavioral training sessions in which ferrets performed fewer trials were indicative of decreased motivation and attention. Such training sessions were rare, and nearly always followed a break

in behavioral training for a week or more. In one data set for the freely-moving motion integration paradigm, a session in which the ferret performed 187 trials was excluded. Of the six sessions performed at the specified parameters for this task, the other five sessions had a mean of 100 trials with a standard error of 7. We therefore felt that the session with 187 trials was an outlier that exerted undue influence on the fit of the psychometric function.

We characterized behavior using three measures, a sided threshold Δ and thresholds corresponding to 75% and 82% correct. To compute Δ, we first computed signed contrast or signed coherence values, where negative values indicated conditions assigned to the left port, and positive values conditions assigned to the right port. We then determined the fraction of right port responses for each condition. The resulting psychometric curves were fit with a cumulative Gaussian using the Palamedes toolbox for MATLAB (Prins and Kingdom, 2018). Separate lapse rates were fit for left and right responses. 95% confidence intervals for psychometric curves were computed for a binomial using the Clopper-Pearson method (Clopper and Pearson, 1934). Finally, Δ was defined as the change in contrast or coherence required to increase the probability of a right choice from 50% to 68% of the maximum fraction of right responses (Busse et al., 2011). To compute thresholds based on percent correct responses, we first averaged performance across the two sides. The resulting data were then fit with a cumulative Weibull function using the Palamedes toolbox, and thresholds determined as the contrast or coherence levels required to reach a performance of 75% or 82% correct.

Contrast sensitivity curves were fit using a double exponential of the form $k_s (\omega \cdot k_\omega)^\alpha \exp(-\beta \cdot \omega \cdot k_\omega)$, where ω is the spatial frequency (Kiper and Kiorpes, 1994). The parameters k_ω and k_s capture shifts along the frequency and sensitivity axes, respectively, while

α and β capture the steepness of the low and high frequency portions of the curve. This sensitivity curve was fit using an fminsearch algorithm in MATLAB. Error bars for sensitivity estimates were calculated by parametrically bootstrapping the data 1000 times, and fitting these bootstraps with psychometric functions to create a distribution of sensitivity estimates (Efron and Tibshirani, 1986). These represent 68% confidence intervals, or approximately one standard deviation from the mean.

The fidelity of the fit of a psychometric function was evaluated in two ways. First, the deviance of the fit was computed (Wichmann and Hill, 2001), which is defined as the extent to which the fit deviates from a saturated model in which there are no residual errors between the observed data and the fit. This tests how likely the fit is given the data. By convention, fits with deviance with significance less than 0.05 are rejected. The deviance and its significance were computed using the Palamedes goodness-of-fit function with 1000 simulations. Second, the mean squared error (MSE) between the model and the data was also computed.

To evaluate the statistical significance of differences between psychometric curves, likelihood ratios were computed of the form λ = (L(data | single curve) / L(data | independent curves)) (Britten et al., 1992; Hoel, P. et al., 1971). -2ln(λ) is distributed as chi-squared with degrees of freedom equal to the difference in dimensionality between the lesser and fuller model (Wilk's theorem). Differences between two thresholds were tested for significance by parametrically bootstrapping the data sets 1000 times, and generating a distribution of thresholds for each. A Welch's t-test was then used to determine whether the bootstrapped threshold distributions were significantly different. On the other hand, to test whether two thresholds were equivalent each dataset was bootstrapped 1000 times, and a distribution of

the differences in the threshold values was generated. The equivalence bound was set to 2.5%, and the probability of threshold differences falling within this equivalence bound was derived from the difference distribution. This test for equivalence (TOST) yielded the p-value (Walker and Nowacki, 2011). Tests for equivalence were always performed on data from the same animal on the same task with two different stimulus conditions, and were only performed when the difference between psychometric curves was not statistically significant.

2.2.5 Electrophysiology

Animal preparation and recordings

The electrophysiology experiments followed established methods detailed previously (Lempel and Nielsen, 2019). Briefly, experiments were performed in animals anesthetized with isoflurane (during surgical procedures: 2 – 3%, during recording: 0.5 – 1.5%). Animals were paralyzed with pancuronium (0.15 mg/kg/hr) to prevent eye movements during recordings. A number of vital parameters (EtCO2, SPO2, heart rate and EEG) were monitored continuously to maintain animals at appropriate anesthetic depths. Neural signals were detected using either custom-built tetrodes or 64-channel silicon microprobes (Masmanides lab, UCLA). Tetrodes were made using 12 µm nichrome wire (California Fine Wire Company), and were plated using a gold solution (Sifco ASC) to reach final impedances of 150-500 kΩ. Silicon probes were gold-plated to reach final impedances of 150-300 kΩ. Signals were amplified and recorded using either a CerePlex Direct amplifier (Blackrock Microsystems) or a RHD2000 amplifier (intan Technologies). Raw data was acquired at 30 kHz and filtered between 250 Hz and 5 kHz. A total of 10 penetrations were made across the 3 animals. The number of cells recorded concurrently (that were included in the analysis as significantly responsive and direction selective; see

below) ranged between 1 and 4 cells. Of the 34 neurons included in the final analysis (see below), 7 were recorded using the multichannel probes; the rest were recorded using tetrodes.

Stimuli

Visual stimuli were displayed on a gamma corrected 24" LCD monitor with a refresh rate of 120 Hz. The monitor was placed 25 – 35 cm in front of the ferret. RDK stimuli consisted of white dots shown on a black background. Otherwise, they were constructed identically to the behavioral experiments. Dot speed was fixed at 48 deg/s. For the tetrode recordings, we manually determined the preferred direction of the neuron under study in an initial experiment. The main experiment then consisted of RDK moving either in the neuron's preferred direction or in the opposite (null) direction. For multichannel probe recordings, we initially determined the preferred direction of a selected neuron, and then used this direction and its opposite for the RDK. In addition to the initially selected neuron, other neurons that also strongly responded to the chosen RDK direction and that passed our selection criteria (see below) were also included in the analysis. In 1 multichannel recording experiment, we repeated the experiment with a different set of directions to drive a second group of cells with very different stimulus preferences, making sure that nonoverlapping sets of neurons resulted from these experiments. Coherences were varied from 10 - 100%, and each coherence level and direction was repeated 20 times in a pseudo-random sequence. 20 blank trials were randomly interleaved throughout the experiment. Each RDK trial began with a static presentation of the first frame of the RDK for 2 s to control for responses to luminance changes. Dots then moved

for 1 s, before presenting the last frame statically for 0.5 s. A blank black screen was shown between trials.

2.2.6 Data analysis and statistics

Single unit isolation was performed off-line using custom MATLAB software. A spike detection threshold was set manually for each recording. Isolation was then based on multiple spike waveform characteristics (e.g., spike amplitude peak, area under the waveform, repolarization phase slope etc.) recorded on the four tetrode channels or on neighboring channels of the silicon probe. Quality of isolation was confirmed by inter-spike interval (ISI) analysis. Units that displayed ISIs below 1.2 ms were excluded.

Identified single units had to pass two criteria to be included in further analyses. First, they had to be responsive, as indicated by a significant difference in responses to the preferred direction and blanks (student's t-test, $p < 0.01$), as well as a response rate of at least 6 spikes/s for the best stimulus. Second, they had to be direction selective, quantified as a significant difference in responses between preferred and null direction (student's t-test, $p < 0.01$). 43 of 72 recorded neurons passed the responsiveness test, and 37 of the 43 neurons (86%) were considered direction selective.

We used established approaches to compute neurometric curves (Britten et al., 1992; Green and Swets, 1966). For a given single unit, the distributions of responses to its preferred and null direction were computed at each coherence level. Here, a response is defined as the number of spikes during the 1 s presentation of the moving RDK. A receiver operating characteristic (ROC) curve was then generated for each coherence level by setting a threshold,

and determining the probabilities that the preferred or null direction elicited a response exceeding the threshold. Thresholds could range from 0 to each cell's maximum response and were increased in steps of 1 impulse (similar to Britten et al., 1992). The area under the ROC curve (aROC) for a given coherence was taken to be a proxy for the fraction correct that would be obtained from listening to the neuron's responses, and used to construct a neurometric function for each neuron. Finally, a cumulative Weibull function was fit to the estimated fraction correct at each coherence level using the Palamedes toolbox. Thresholds were estimated from each of these curves using a criterion of 75% correct. 1 neuron was excluded from further analysis because the Weibull function fit failed to converge, and 2 additional neurons were excluded because their aROC at 100% coherence was below 0.75. This resulted in a total of 34 neurons for the full analysis.

2.3 Results

2.3.1 Behavioral estimates of visual acuity

Most of the existing studies on ferret visual behavior tested the animals in setups in which they could move freely and earn food or water reward for performing a particular action (such as opening a door) in response to a visual stimulus (Doty et al., 1967; Hupfeld et al., 2006; von Melchner et al., 2000; Pollard et al., 1967; Pontenagel and Schmidt, 1980). These behavioral paradigms have the advantage of closely mimicking natural foraging behavior. They also do not require the cranial implants necessary for head-fixed paradigms. Thus, they lend themselves to expedient testing of large cohorts of animals, as may be required by some

developmental studies. We therefore decided to first implement a similar freely-moving testing paradigm.

Our behavioral setup was designed for 2AFC discrimination tasks. It consisted of an open box with a screen placed on one wall for visual stimulus presentation (Figure 2.1A). This screen was flanked by two choice ports, each consisting of an IR beam emittor and detector surrounding a water spout. Every visual stimulus was associated with one of the choice ports. A similarly constructed trial initiation port was placed in the middle of the wall opposite the screen. The animal initiated each trial by breaking the beam in this port (see Figure 2.1B for task sequence). This triggered stimulus presentation, and was rewarded with a small amount of water from the trial initiation port. The animal then had to respond to the stimulus by crossing the box, and selecting one of the two choice ports. Selection of the correct port resulted in the delivery of a water reward, removal of the stimulus (depending on the task), and ending of the trial. If the animal instead chose the incorrect port, it could not advance to the next trial before activating the correct port. Once the animal corrected its choice, a small water reward (1/10 of the full amount) was delivered to maintain engagement in the task. Requiring ferrets to choose the correct port in order to complete the trial was essential in encouraging an even sampling of both ports early in learning, and was useful in preventing biased behavior during all testing stages.

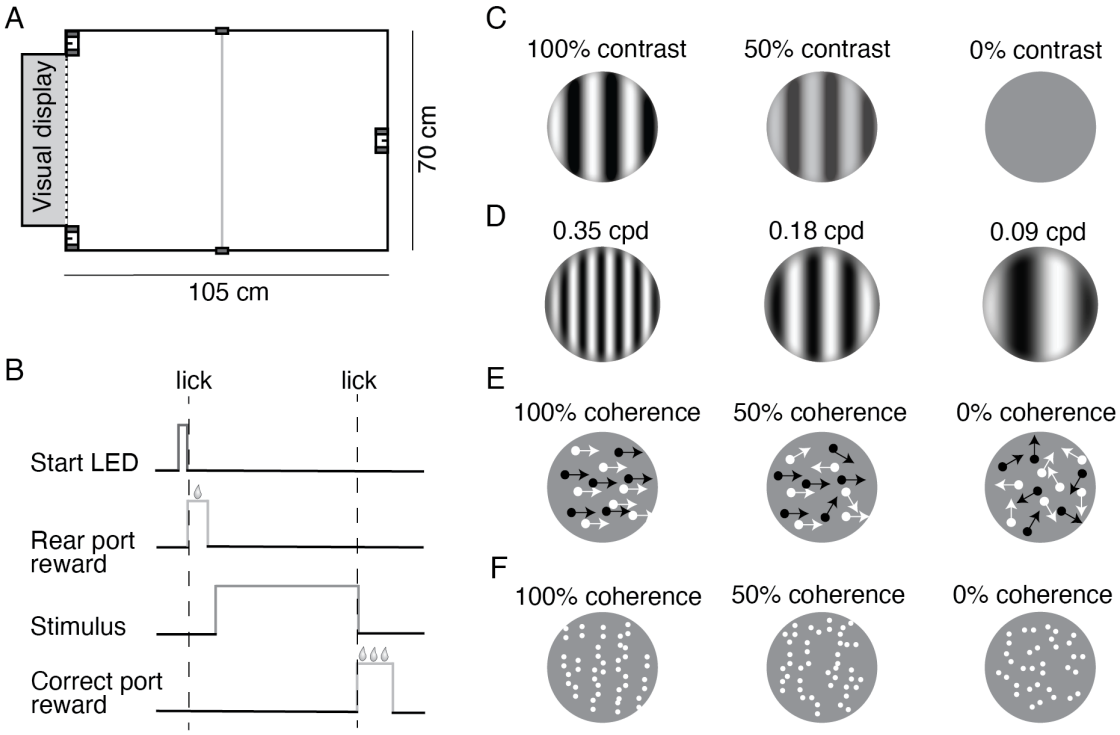

Figure 2.1 Freely-moving setup and basic stimulus design.

(A) *Schematic of freely-moving behavioral setup. The trial initiation port was centered on the wall opposite the visual display. Choice ports were on either side of the display. An IR beam was also placed across the middle of the box.*
(B) *Task structure. An LED was illuminated above the trial initiation port to signal that the ferret could initiate a trial. When the ferret broke the IR beam in that port, a small reward was dispensed, and stimulus presentation was triggered. Subsequent selection of the correct port resulted in ending stimulus presentation and reward delivery.*
(C) *Acuity task stimuli: Sinusoidal gratings with varying contrasts and spatial frequencies. The ferrets were trained to discriminate horizontal from vertical gratings.*
(D) *Motion integration task stimuli: RDK consisting of black and white dots with varying coherence levels. RDK had to be discriminated based on their direction of motion (left or right).*
(E) *Form integration task stimuli: Linear Glass patterns with varying degrees of coherence. The ferrets were trained to discriminate horizontal from vertical patterns.*

We first used this setup to estimate the ferret's visual acuity behaviorally, a necessary prerequisite for determining appropriate stimulus parameters for the experiments to follow. We therefore trained ferrets to discriminate horizontal from vertical gratings (Figure 2.1C), and varied grating contrast and spatial frequency across trials (contrast range: 0.05 – 0.95 Michelson contrast, spatial frequency range: 0.09 – 0.36 cpd). To limit changes in spatial

frequency induced by changes in viewing distance, stimuli were only shown until the ferret crossed an IR beam halfway between the trial initiation port and the screen. The spatial frequency values given above are calculated from this point.

Visual acuity was determined for 3 adult ferrets (see Methods for animal selection criteria). On average, the animals performed 103 trials per session (SEM: 4 trials) and achieved good performance for the easiest conditions (see Tables 2.1 – 3 for training history for individual animals, trial and session numbers, and statistics per animal). For the optimal spatial frequency (0.18 cpd) and the highest contrast, ferrets averaged 90% correct (SEM: 5.25% correct). In addition, their performance depended predictably on stimulus contrast and spatial frequency. This is clearly demonstrated by computing performance as a function of grating contrast for each spatial frequency (see Figure 2.2A for an example ferret): For all spatial frequencies, performance was close to chance level for low contrasts, but improved rapidly with increases in contrast. For further analysis, we captured the dependency of performance on contrast at each spatial frequency in the following way: We first computed performance as a function of grating contrast for each spatial frequency individually. To better account for potential response biases, performance was quantified as the fraction of vertical responses, and contrasts were expressed as 'sided' contrasts, with -1 indicating a full contrast horizontal grating, and +1 a full contrast vertical grating. The resulting data were fit with a cumulative Gaussian to generate a psychometric function per spatial frequency. We then determined the 'sided' contrast threshold Δ for each psychometric function, defined as the contrast increment required to go from 50% vertical responses to 68% of the maximum fraction of vertical responses (i.e. to 68% of 1 minus the lapse rate). Finally, the contrast sensitivity for a spatial

frequency was defined as the inverse of Δ. The same approach has previously been used to evaluate acuity in mice (Busse et al., 2011).

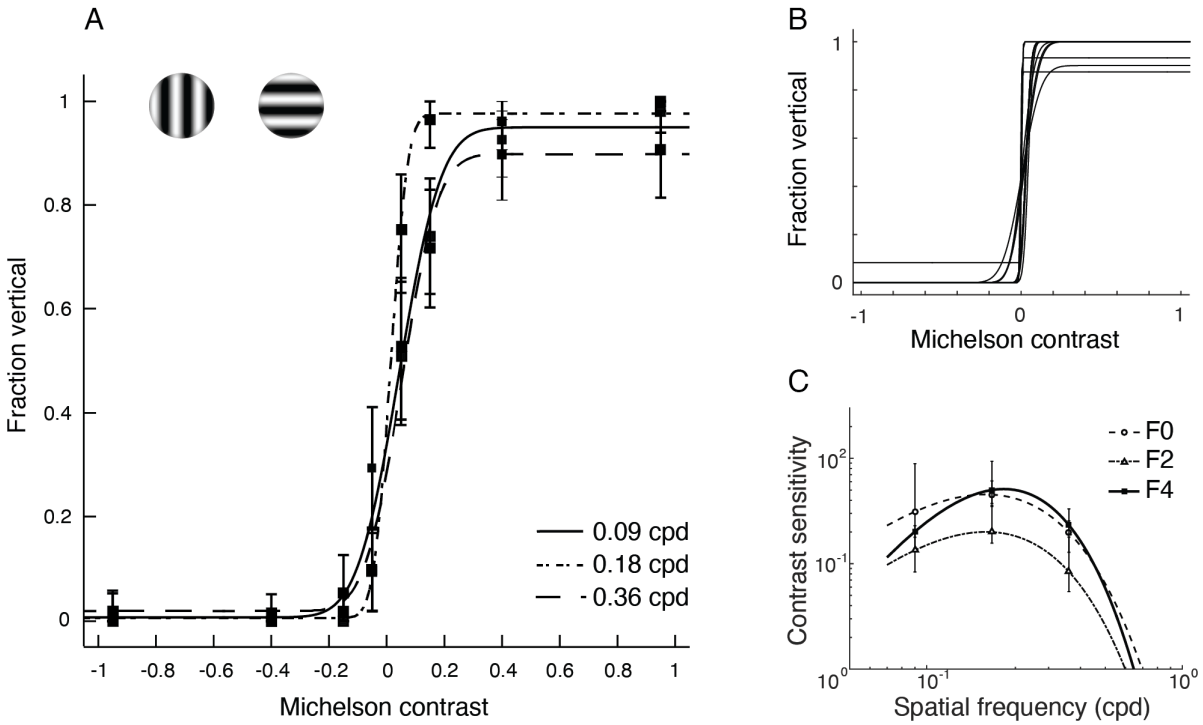

Figure 2.2 Behavioral estimates of visual acuity

(A) *Psychometric curves for one ferret (F4) for three spatial frequencies. Error bars represent 95% confidence intervals (see Methods).*
(B) *Psychometric curves fit to data from individual testing sessions using a spatial frequency of 0.18 cpd (ferret F4). 13 sessions are shown here.*
(C) *Contrast sensitivity curves for each ferret. Error bars represent 68% confidence intervals (see Methods).*

In general, fits were based on aggregating behavior across multiple sessions for each ferret (N=14 +/- 2) to improve the estimation of contrast sensitivity. However, we verified in one ferret (F4) that performance was indeed consistent across days. For this animal, we fit data of individual sessions performed at a spatial frequency of 0.18 cpd, and determined a sided coherence threshold Δ for each session. These data confirmed that thresholds were highly similar across sessions (Figure 2.2B, standard deviation of Δ: 1.28%).

Finally, we used the collected data to compute a contrast sensitivity curve for each ferret. To this end, contrast sensitivity as a function of spatial frequency was fit with a double-exponential function (see Methods for details). The fit to the contrast sensitivity curve could then be used to determine two measures for every ferret: First, peak frequency, which corresponded to the spatial frequency with maximal contrast sensitivity. Second, cutoff frequency (also called maximum visual acuity), which corresponded to the spatial frequency with a contrast sensitivity of 1, and was determined by extrapolating the fit. Contrast sensitivity curves were highly similar across ferrets (Figure 2.2C). They revealed an average peak spatial frequency of 0.18 cpd (SEM: 0.010 cpd), and average cutoff frequency of 0.65 cpd (SEM: 0.029 cpd).

Ferret	Peak Contrast Sensitivity (cpd)	Maximum Acuity Estimate (cpd)	No. Trials	No. Sessions
F0	0.17	0.70	1420	11
F2	0.17	0.60	1500	17
F4	0.20	0.65	1291	13
Mean	**0.18 +/- 0.01**	**0.65 +/- 0.03**	**1404 +/- 61**	**14 +/- 2**

Table 2.2 Peak contrast sensitivity and maximum acuity estimates.

Mean reported with standard error.

Our behavioral estimates of contrast sensitivity and acuity are in good agreement with existing data on spatial frequency tuning in ferret area 17 (Baker et al., 1998). The optimal spatial frequencies for area 17 neurons range from about 0.1 to 0.5 cpd, with a geometric mean of 0.25 cpd. Furthermore, neurons with the highest spatial frequency preference have an

average bandwidth of 1 octave. Thus, not only is the behaviorally measured peak sensitivity close to the average optimal spatial frequency for area 17, the cutoff frequency also falls within the range of spatial frequencies that can elicit responses in area 17. While there are limitations to estimating acuity based on freely-moving behavior, the good match between behavior and neural data strongly supports our measurements. We therefore used these data as a basis for selecting stimulus parameters for the following experiments, in particular the size of dots in RDK and Glass patterns.

2.3.2 Measurements of motion integration in freely-moving ferrets

Based on the success of the acuity experiment, we used the same freely-moving paradigm to probe higher-level motion processing by testing whether ferrets were capable of motion integration. RDK (Figure 2.1D) have become the standard stimulus to assess visual motion integration performance, as they can be constructed so that integration across multiple dots is required for perceiving a global direction signal. Here, 3 ferrets were trained to discriminate RDK based on their global direction (left versus right) at a dot speed of 48 deg/s. Ferrets were introduced to this task at 100% coherence (i.e. with all dots moving in the global direction), and continued with 100% coherent motion until they performed at 80% correct or above. All ferrets demonstrated rapid learning, and reached criterion at 100% coherence within 3 - 5 sessions.

At full coherence, the direction discrimination task could theoretically be solved by attending to a single dot. Lower coherences require integration of motion information across dots, and therefore more accurately reflect motion integration capabilities. In addition, systematic changes in coherence levels allow threshold measurements, and thereby a

quantitative assessment of motion integration capabilities. For this reason, we gradually introduced RDK with lower coherence once criterion performance was reached for the full coherence. After 3 – 5 additional sessions, ferrets performed the RDK task across a range of coherence levels (20 - 100% coherence). For the remaining analysis, only data from sessions in which the ferrets were assessed on the full range of coherences were included (3-12 sessions per animal).

In general, ferrets exhibited excellent performance on the easiest direction discrimination conditions: They performed on average at 98% correct for 100% coherent motion (SEM: 0.21%). These low lapse rates show that ferrets not only mastered the task, but that the behavior was under tight stimulus control. Consistent with a performance that is mainly driven by the information present in the motion stimulus, each ferret's performance systematically depended on the coherence level. Once again, performance was quantified by computing a sided performance measure to appropriately address any response bias. More precisely, for each ferret we computed the fraction of right motion responses as a function of a sided coherence measure (-100%: full coherence, direction left; +100%: full coherence, direction right). These data were then fit with a cumulative Gaussian (Figure 2.3A). Data from all ferrets could be fit well: No fits exhibited significant deviance from a saturated model (F0: deviance = 7.04, p = .143, F4: deviance = 10.02, p = .199, F6: deviance = 9.19, p = 0.128, see Methods), and on average, fits had a MSE of 2.34 (SEM: 0.078).

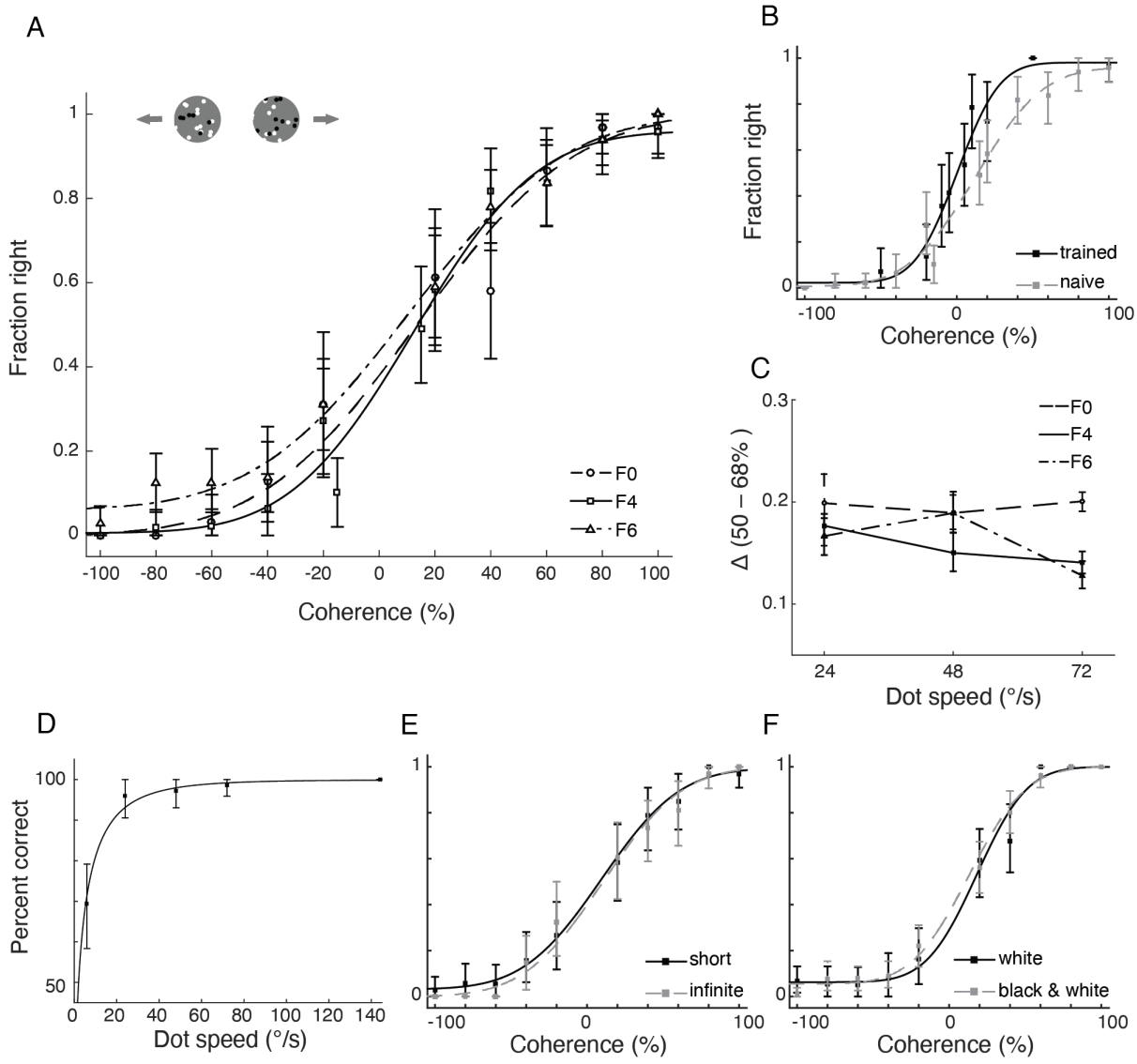

Figure 2.3 Motion integration thresholds

(A) *Psychometric curves for each ferret on the motion integration task (dot speed 48 deg/s). Error bars represent 95% confidence intervals.*
(B) *Impact of training on motion integration thresholds: Performance for F4 at the time of initial threshold measurements, and after 11 additional sessions.*
(C) *Sided coherence threshold Δ as a function of dot speed for each ferret.*
(D) *Performance of ferret F4 for RDK of 60% coherence as a function of dot speed.*
(E) *Performance comparison for short versus infinite dot lifetime (data for ferret F0).*
(F) *Performance comparison for white dots on a black background versus black and white dots on a gray background (data for ferret F6).*

Motion integration capacity was then quantified based on the fits by computing a sided coherence threshold Δ (see Table 2.3 for data from individual ferrets and alternate threshold measures). Analogous to the computation of the contrast threshold, we defined Δ as the increase in coherence required to change the fraction of right responses from 50% to 68% of the maximum. This analysis yielded an average Δ across ferrets of 17.62% (SEM: 1.30%). Note, however, that these thresholds were determined after a limited number of sessions to quantify the general motion integration capacity of adult ferrets. Thresholds could be improved significantly by additional training (Figure 2.3B): We continued to train F4 after the initial threshold measurement. A re-evaluation after 11 additional sessions resulted in a sided coherence threshold Δ of 9.44%, significantly lower than the initial value of 15.01% (log-likelihood ratio test, $-2*\ln(\lambda) = 15.83$, degrees of freedom = 2, $p = 3.6576 \times 10^{-4}$).

Performance on the RDK task might be expected to depend on dot speed. We therefore measured motion integration thresholds at 3 speeds: 24 deg/s, 48 deg/s, and 72 deg/s. No clear effect of speed on threshold was observed over this range (Figure 2.3C). To investigate further, the performance of one ferret was evaluated at a fixed dot coherence (60%) and variable speed per trial (6 - 144 deg/s). In agreement with the larger data set, the ferret's performance in the control experiment was largely independent of speed (Figure 2.3D). For speeds larger than 7.22 deg/s, the ferret performed above 75% correct, and performance was at or above 95% correct for speeds above 24 deg/s.

Finally, we performed two control experiments to test whether task performance was indeed due to integration of signals across dots, and not other stimulus factors. In the first control experiment, we tested the impact of dot lifetime, which determined how long each

individual dot could remain a signal dot. Long lifetimes might allow a ferret to solve the task based on the trajectory of a single dot, rather than through integration. Thus, in the control experiment we randomly set lifetime to either 25 ms or 2 s at the beginning of every trial. Performance on the task (Figure 2.3E) did not differ significantly between the two lifetime conditions (log-likelihood ratio test, $-2*\ln(\lambda) = 3.07$, degrees of freedom = 2, $p = .2156$), and Δ values for each condition were equivalent within 2.5% of each other (TOST, $p = 10^{-3}$), indicating that at least the ferret used in the control experiment was not following single dots to perform the task. In a second control experiment, we tested the impact of dot color. In the RDK experiments described so far, 50% of the dots were black and 50% white to provide some stimulus contrast to the animals (shown against a gray background). To rule out any effects of this color choice, we tested performance for RDK constructed from white dots only, shown on a black background (Figure 2.3F). Again, the change in stimulus parameter did not affect performance in the control experiment (log-likelihood ratio test, $-2*\ln(\lambda) = 0.945$, degrees of freedom = 2, $p = 0.6233$; Δ between conditions equivalent within 2.5%, TOST, $p = 0$). In summary, our experiments demonstrate a clear capacity for motion integration in ferrets.

2.3.3 Tests of motion integration using a head-fixed paradigm

The freely-moving behavioral paradigm used so far excels in its ease of implementation. Ferrets generally learned quickly using this paradigm, and the results of the first two experiments confirm its suitability for psychophysical experiments. The main disadvantage of freely-moving behavior is a limited control over viewing distance and head position. Variable viewing distances and head positions complicate accurate estimates of how stimulus

parameters such as stimulus speed, size, and spatial frequency influence task performance. Furthermore, freely-moving behavior does not lend itself as easily to simultaneous neural recordings, in particular using optical methods. For these reasons, we also developed a head-fixed behavioral paradigm. We then used this paradigm to measure motion integration performance in two additional ferrets, which allowed a direct comparison of behavior in the two paradigms.

The head-fixed setup consisted of a head-post holder, a body holder, and three independently movable water spouts for reward delivery (Figure 2.4A & B). Licks on the water spouts could be detected as changes in spout capacitance (see Methods for details). A screen for visual stimulus display was placed 42 cm in front of this setup. The head-post holder allowed fixation of the head by means of an implanted head post, while the body holder limited movements by the rest of the body. A similar configuration has been used for auditory studies in ferrets (e.g., Dobbins et al., 2007; Fritz et al., 2003). At the beginning of training, the relative positioning of head-post holder and body holder were customized for each ferret to ensure a comfortable posture, and the animals were slowly acclimated to the setup (see Methods). The relative position of the water spouts was optimized such that the animal could lick them easily but distinctly: in other words, the animal could not contact more than one spout at the same time.

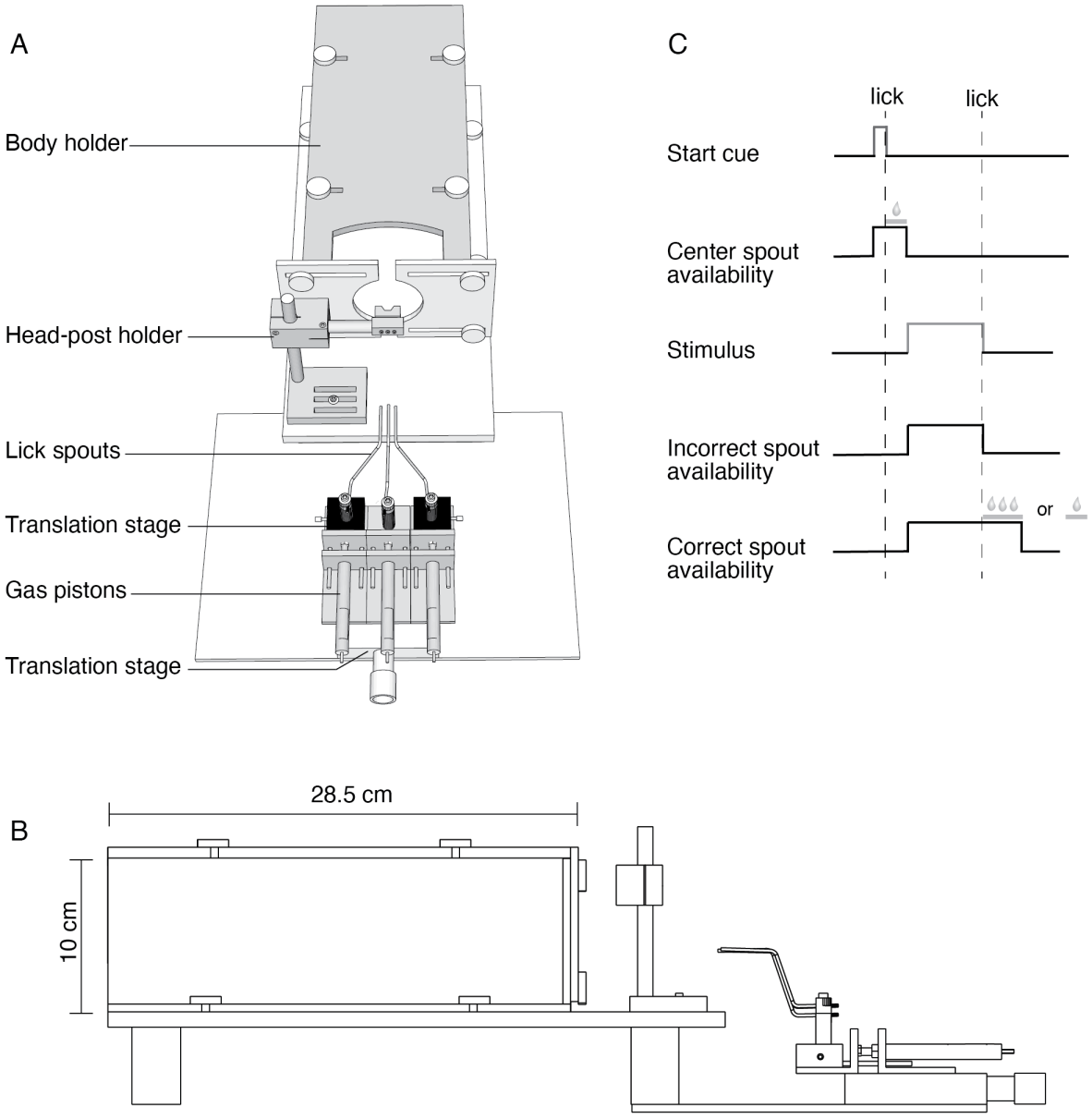

Figure 2.4 Head-fixed behavior paradigm.

(A) *Schematic drawing of the head-fixed behavior setup (top view). The setup consisted of 3 major components, a body holder, head-post holder, and the reward spouts. All three components could be moved relative to each other to allow the animal to assume a comfortable posture while in the setup, and to reach the spouts easily. Each spout could be moved independently between a retracted and a forward position by means of a gas piston. Animals could only lick the spouts when in the forward position. All spouts were mounted on a large translation stage to control their overall distance from the animal. In addition, the two peripheral spouts were mounted on two smaller translation stages to control the lateral distance between the spouts. This was necessary to make sure that animals could not activate more than one spout simultaneously.*
(B) *Side-view of the head-fixed behavior setup.*
(C) *Three-spout task design. A trial initiation cue was presented and the center spout was moved forward. When the ferret licked the center spout, a small reward was dispensed. Next, the center spout was retracted and stimulus presentation was triggered. The two choice spouts were moved forward. If the ferret licked the*

correct spout first, the incorrect spout was retracted, the stimulus removed, and the ferret received a large water reward. If the ferret contacted the incorrect spout first, it was also retracted. The ferret then had to contact the correct spout (which remained in position) to end the trial and receive a much smaller reward.

In order to mimic the structure of the freely moving behavioral paradigm, the central spout was designated as the trial initiation spout, while the two peripheral spouts were designated as choice spouts. Each spout had two positions: a retracted position, where the animal could not reach the spout, and a forward position, where the animal could lick the spout easily. Usually, ferrets did not lick while the spouts were retracted. Thus, the potential of motion artifacts throughout the trial – which could pose problems for combined behavioral and recording experiments – could be further limited by controlling the availability of the water spouts. A similar three-spout configuration, albeit with stationary spouts, has been used in mice (Marbach and Zador, 2017).

The head-fixed 2AFC task used the following design (Figure 2.4C): During the ITI, all spouts were in the retracted position. After the ITI and a trial initiation phase (see below), a visual stimulus was presented on the screen. Following a brief delay, the two peripheral choice spouts were then moved forward, and the ferret had to respond to the visual stimulus by licking one of them. As in the freely-moving paradigm, we implemented a task design that forced sampling of both ports: In the case of a correct response, water was delivered as soon as the ferret contacted the spout. At the same time, the second spout was retracted. If the ferret instead chose the incorrect spout first, this spout was immediately retracted without reward. The ferret then had to correct its choice by contacting the remaining correct spout – rewarded

with a much smaller amount of water – to end the trial. At this point, the correct spout was also retracted.

We explored two different trial initiation options with the two ferrets. In one ferret (F9), trials were passively initiated. For this animal, each trial began automatically after a fixed ITI by presenting a white square on the screen, which served to alert the animal to the upcoming stimulus presentation. In this design, the central spout was not used. In the other ferret (F8), we explored an active trial initiation. After the ITI elapsed, a white square again was presented on the screen. At the same time, the central spout was moved forward. The animal was required to lick this spout (rewarded with a small amount of water) to fully initiate the trial. The spout was then retracted, and the visual stimulus presented after a brief delay. While this full three-spout version of the task might be more challenging to learn, it offers the advantage of starting each trial with a central licking position, which could help reduce biases for the subsequent response choice.

As before, ferrets were initially trained on the RDK direction discrimination using stimuli with 100% coherence (dot speed 72 deg/s). Both ferrets learned the task, and participated well. F9 performed at 80% correct or above within 1 week of training, while F8 reached the same criterion within 3 weeks of training. F9 performed 142 trials per session on average (SEM: 14 trials), and F8 performed 469 trials on average (SEM: 15 trials). The data collected from the head-fixed task exhibited many of the same properties observed for the freely-moving paradigm (Figure 2.5). First, ferrets again performed the task with low lapse rates (3.81% +/- 1.96%, mean and SEM), comparable to the lapse rates for freely-moving animals (for 72 deg/s: 0.91% +/-0.14%, mean and SEM). Thus, despite the fact that the different setups might have

been expected to produce differences in motivational state (such as the overall willingness to perform the task, the subjective cost incurred by an error, etc.), performance was under similarly strong stimulus control in both paradigms. Second, psychometric functions were again well described by a cumulative Gaussian (F9: deviance = 1.76, p = 0.802, MSE = 0.25, F8: deviance = 3.69, p = 0.760, MSE = 0.67). Sided coherence thresholds Δ based on these fits were 18.36% for F9 and 28.35% for F8. This places F9's performance well within the range of Δ values observed for the same speed in the freely-moving paradigm (12.79% - 20.06%), while F8's performance was somewhat worse. Note, however, that since F8 performed so many trials per session, we used only 2 sessions to compute Δ for this ferret. For all other ferrets, 4 – 12 sessions were used to determine the threshold. It is possible that extra training provided by additional sessions would have lowered thresholds for F8 to be more similar to the other ferrets.

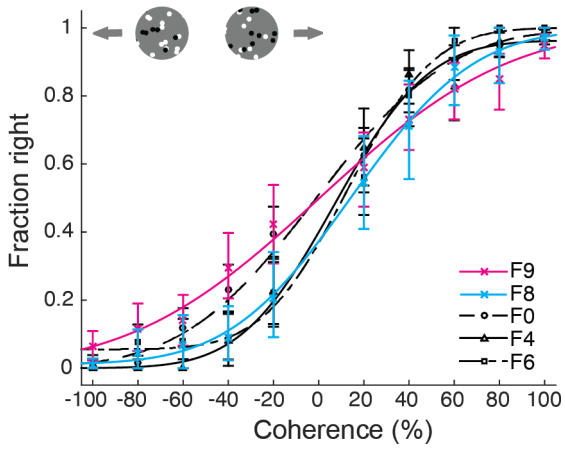

Figure 2.5 Comparison of motion integration thresholds measured using head-fixed and freely-moving paradigms.

Psychometric curves from all ferrets for the motion integration task at 72 deg/s. Colored lines show the performance of the head-fixed animals, F8 and F9. Black lines show the performance of freely moving animals (F0, F4 and F6). Error bars represent 95% confidence intervals.

Task	Δ (50 – 68%)	Threshold at 75%	Threshold at 82%	No. Trials	No. Sessions
Dots, 72°/s					
F0	20.06%	35.62%	45.07%	1371	12
F4	14.05%	23.39%	32.17%	503	6
F6	12.79%	26.74%	34.98%	778	7
Mean, free	**15.63 +/- 2.24%**	**28.58 +/- 2.65%**	**37.40 +/- 3.92%**	**884 +/- 256**	**8 +/- 2**
F9 (hf)	18.36%	30.55%	41.62%	568	4
F8 (hf)	28.35%	45.27%	59.48%	939	2
Mean, hf	**23.36 +/- 5.00%**	**37.91 +/- 7.36%**	**50.55% +/- 8.93%**	**753 +/- 186**	**3+/- 1**
Mean, all	**18.72 +/- 2.75%**	**32.31 +/- 3.83%**	**42.66 +/- 4.79%**	**832 +/- 155**	**6 +/- 2**
Dots, 48°/s					
F0	18.93%	42.96%	49.98%	308	3
F4	15.01%	25.10%	35.56%	581	5
F6	18.91%	34.51%	47.76%	707	8
Mean	**17.62 +/- 1.30%**	**34.19 +/- 5.16%**	**44.43 +/-4.48%**	**532 +/- 118**	**5 +/- 1**
Dots, 24°/s					
F0	19.89%	38.37%	50.89%	570	5
F4	17.67%	39.16%	47.37%	492	5
F6	16.67%	33.97%	44.20%	749	8
Mean	**18.07 +/- 0.95%**	**37.16 +/- 1.61%**	**47.49 +/- 1.93%**	**604 +/- 76**	**6 +/- 1**
Glass					
F0	21.32%	44.31%	66.68%	766	6
F6	23.25%	48.94%	65.45%	616	5
Mean	**22.28 +/- 0.97%**	**46.65 +/-2.34%**	**66.06 +/- 0.62%**	**691 +/- 75**	**6 +/- 1**

Table 2.3 Threshold evaluations for each complex visual task. *Hf – head-fixed behavior. Free – freely-moving behavior. Mean reported with standard error.*

The speed of task learning, low lapse rates, and fidelity of psychometric function fits demonstrate that a head-fixed 2AFC task design can be used for visual psychophysics in ferrets, thus opening the door for future work combining neural recordings with visual tasks in ferrets.

Since no major differences were observed between the three- and two-spout versions of the task, both are viable designs. Moreover, the general agreement of thresholds across paradigms suggests that they may be used to complement one another.

2.3.4 Form integration capacity of adult ferrets

The experiments described above demonstrate clearly that ferrets are capable of complex motion vision. Another important aspect of higher-level vision – at least in primates – is the ability to process form information, a function that is usually associated with different visual areas than processing of motion information (Ungerleider and Pasternak, 2004). While it is unclear whether the same holds for ferrets, at least their basic capacity to perform tasks requiring general form discrimination has been demonstrated (Doty et al., 1967; Pontenagel and Schmidt, 1980). Rather than investigating the most complex aspects of form vision (such as object recognition), we decided to study form vision at a comparable level of complexity to the RDK motion integration task. To this end, we chose Glass patterns (Glass, 1969; Glass and Pérez, 1973). In addition to consisting of similar elements as the RDK, Glass patterns offer the advantage of allowing measurements of form integration thresholds in a comparable manner to the motion integration thresholds. For these reasons, they have been used to assess the development of sensitivity to global form sensitivity in humans and monkeys, and to compare it to the development of sensitivity to global motion (Kiorpes et al., 2012; Lewis et al., 2004). Glass patterns can be constructed to yield different global patterns, including concentric, radial or linear forms. Here, we chose linear Glass patterns (Figure 2.1F), because they allowed us to continue to use a 2AFC task very similar to the task used for the RDK.

Two ferrets were trained to discriminate horizontal from vertical Glass patterns. All tests used the freely-moving paradigm because of its easier implementation. As for the RDK, Glass patterns were introduced at 100% coherence, and remained at this level until ferrets achieved a criterion performance of 80% correct. Lower coherence levels were then gradually introduced in subsequent sessions. In the following analyses, data were limited to behavioral sessions that used the full range of coherences (20 - 100%). Ferrets were able to learn the basic Glass pattern task (Figure 2.6), and achieved good performance on the easiest condition (F0: lapse rate = 91%, F6: lapse rate = 87%). Their overall behavioral data was once again well described by cumulative Gaussian functions (F0: deviance = .379, p = 0.774, MSE = 2.06; F6: deviance = 0.401, p = 0.5780, MSE = 1.31). Sided form coherence thresholds Δ were computed identically to the sided motion coherence thresholds to facilitate a comparison across tasks (see Table 2.3 for other thresholds). For F0, this analysis resulted in a threshold of Δ = 21.32%; the threshold for F6 was Δ = 23.25%. Both ferrets were previously tested on the freely-moving motion integration task, allowing a direct comparison of thresholds between the two tasks. For both ferrets, thresholds were significantly higher in the Glass pattern than the RDK task (F0: 2.38% difference in Δ between RDK at 48 deg/s and Glass pattern task, p = 7.919e-189, t = 32.77, df = 1998; F6: 4.34% difference in Δ, p = 7.169e-138, t = 27.08, df = 1998). This suggests that even though they were able to learn both tasks, the ferrets found the Glass pattern task more challenging than the RDK task. The increased difficulty may reflect genuine differences in processing of form versus motion information in ferrets. However, since both ferrets were trained on the motion before the form task, we can't rule out that the training sequence caused interference between the two tasks.

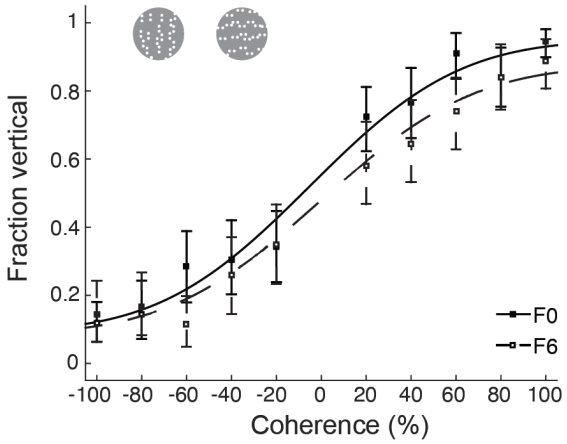

Figure 2.6 Form integration thresholds measured using Glass patterns.

Psychometric curves for Glass pattern stimuli for two ferrets. Error bars represent 95% confidence intervals.

2.3.5 Comparison of behavioral and neural motion integration limits

The experiments described above were designed to test behaviorally whether ferrets are able to integrate motion and form information, functions that are associated with mid-level visual areas such as MT and V4 in the primate (Orban, 2008; Ungerleider and Pasternak, 2004). An important aspect of establishing higher-level vision research in ferrets will be to identify the areas supporting the more complex visual behavior we observed. Little is currently known about processing of form information in ferret visual cortex outside of area 17 and 18. The same largely holds for motion processing. However, previous studies have identified one higher visual area involved in motion processing (Hupfeld et al., 2007; Philipp et al., 2006). This area – called PSS or PMLS – is located in the posterior bank of the suprasylvian sulcus (Figure 2.7A). Building on this finding, we recently demonstrated that PSS shows the same signatures of complex motion processing that are observed in primate MT (Lempel and Nielsen, 2019). This

includes a significant change in the degree of motion integration between area 17 and PSS: As in the primate motion pathway (Born and Bradley, 2005; Orban, 2008), motion processing in area 17 is concerned with local motion signals, while PSS extracts integrated, global motion signals.

This provides the opportunity to test whether the behaviorally observed motion integration is consistent with limits imposed by neural activity in higher-level area PSS. Ultimately, the contribution of PSS to visual motion integration behavior will need to be addressed by recording and manipulating neural activity during the task. However, as a first step we compared behavioral thresholds with thresholds of PSS neurons recorded in a different group of animals during anesthetized experiments. In these experiments, we used tetrodes or multi-site silicon probes to isolate responses of individual PSS neurons. For each neuron, we first determined the preferred direction. We then collected responses to repeated presentations of RDK with varying coherence levels. RDK could move either in the neuron's preferred direction, or the opposite (null) direction at a fixed speed of 48 deg/s. These data allowed us to use a signal detection theory approach to determine the likelihood of correctly detecting the preferred direction based on the firing rates of the recorded neuron (Green and Swets, 1966). More precisely, the measured firing rate distributions for preferred and null direction were used to calculate ROC curves at each coherence (Figures 2.7B & C). The probability of correctly detecting motion in the preferred direction at a coherence level could then be estimated from the area under the corresponding ROC curve (aROC). aROC values need to reach reasonably high levels for the remainder of the analysis to be meaningful. Figure 2.7D therefore shows the area under the curve (aROC) at 100% coherence for 36 responsive and

directionally selective neurons. To be included in further analysis, neurons were required to reach a minimum aROC value of 0.75. 34 neurons remained after this step, and were each fit with a Weibull function to capture the dependency of detection probability on coherence level (Figure 2.7E). This neurometric function was used to estimate the integration threshold for each neuron as the coherence required to reach 75% detection probability. A similar approach has been used previously to compare neural responses in primate MT to behavioral motion integration performance (Britten et al., 1992).

Figure 2.7F plots the resulting distribution of PSS neurometric thresholds and the matching behavioral thresholds collected from 3 ferrets tested on the same dot speed in the freely-moving paradigm. To directly compare neural and behavioral results, we recomputed behavioral thresholds as the coherence levels required to reach 75% correct, instead of the sided coherence threshold used earlier (see Table 2.3). We also collapsed the behavioral data across animals to generate an average psychometric curve, and computed its threshold. Despite the fact that neurometric and psychometric thresholds were derived in different groups of animals, the two data sets were in close agreement (Figure 2.7F). The psychophysical threshold of each individual ferret fell within the interquartile range of the neurometric distribution (26.47^{th}, 50.00^{th}, and 67.65^{th} percentiles of the distribution, respectively), and the estimated threshold of the aggregate ferret behavior data was very close to the median of the neural distribution (47^{th} percentile, average psychometric function threshold: 32.22% coherence, median neural threshold: 34.63%). Thus, neural limits on motion integration imposed by PSS are in close agreement with the behavioral observed limits. More work is necessary to fully establish the role of PSS and other visual areas in complex motion processing,

and to identify the areas involved in processing of Glass patterns in ferrets. However, our findings represent a promising sign that at least the RDK task taps into functions supported by the ferret's higher-level visual areas.

Figure 2.7 Comparison of neurometric and psychometric motion integration thresholds. (Opposite page)

(A) *Sagittal view of the ferret brain, with the suprasylvian sulcus (SS) and PSS indicated.*
(B) *Firing rate distributions for an example PSS neuron, evoked by RDK of different coherence levels moving in the neurons preferred direction (black bars) or its null direction (white bars). Each bar indicates the number of trials on which a neuron exhibited a particular firing rate.*
(C) *ROC curves generated from the distributions in (B).*
(D) *aROC values for all directionally selective and significantly responsive neurons (N = 36) at 100% coherence. Red dashed line at 0.75 indicates criterion cut-off.*
(E) *Comparison of an example neurometric function, computed for the neuron shown in (C) and (D), to the average psychometric function. The average psychometric function was generated by fitting behavioral data collapsed across all 3 ferrets tested in the freely-moving paradigm. The threshold for the average psychometric function, using a criterion of 75% correct responses, is also indicated.*
(F) *Distribution of 75% correct coherence thresholds across all directionally selective, significantly responsive neurons with aROC values of 0.75 or above at 100% coherence (N = 34). Also shown are the mean of this distribution, the threshold based on the average psychometric function (see (E)), and the thresholds of each of the three ferrets, all using the same criterion of 75% correct.*

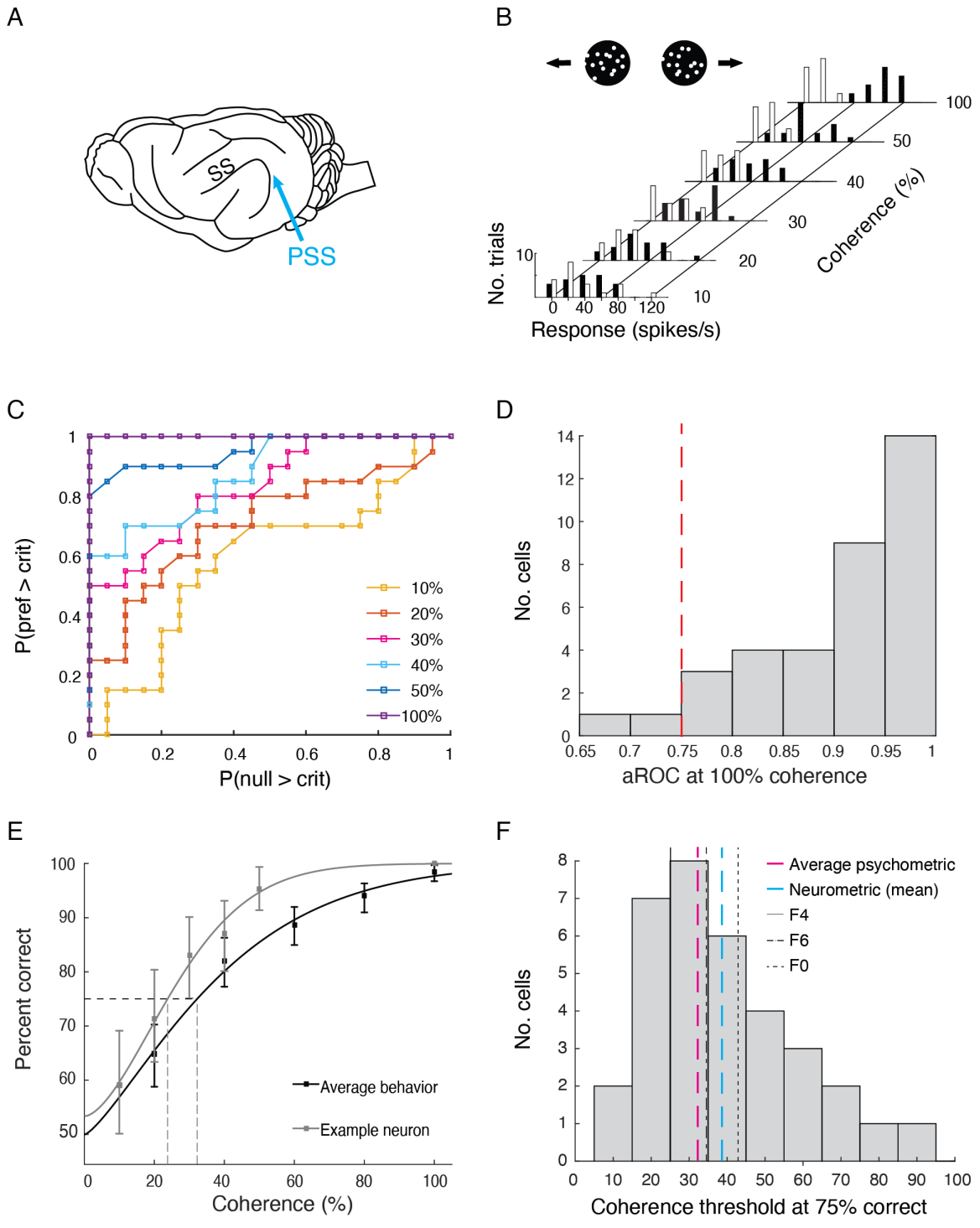
A
SS
PSS
B
100
50
40
30
20
10
Coherence (%)
No. trials
10
0 40 80 120
Response (spikes/s)
C
P(pref > crit)
P(null > crit)
10%
20%
30%
40%
50%
100%
D
No. cells
aROC at 100% coherence
E
Percent correct
Coherence (%)
Average behavior
Example neuron
F
No. cells
Coherence threshold at 75% correct
Average psychometric
Neurometric (mean)
F4
F6
F0

2.4 Discussion

To date, there have been few detailed behavioral studies on the visual capabilities of ferrets. Here, we systematically tested their ability to discriminate simple gratings and more complex stimuli requiring integration. The first important conclusion derived from our experiments is that ferrets are good subjects for visual psychophysics. For all stimulus types tested, their performance systematically depended on critical stimulus parameters such as spatial frequency or coherence level, in a way that was well captured by standard psychometric functions. In addition, performance was reliable across days, and ferrets usually performed a reasonable number of trials per day. Ferrets consistently were able to perform tasks with low lapse rates. This is important, as it confirms that behavior is tightly controlled by the stimulus. It is worth noting that to reliably achieve these low lapse rates, attention needed to be paid to any response bias exhibited during training and testing. Individual animals at times developed a preference for one of the two response ports, and chose it regardless of the stimulus. Requiring the animals to end each trial by choosing the correct spout helped to significantly reduce the occurrence of response biases. For the head-fixed behavior, it was additionally important to ensure that all spouts were equally reachable by the animal. Any remaining biases could then be eliminated by temporarily changing the reward ratio of the response spouts.

So far, head-fixed paradigms have not been used to investigate visual behavior in ferrets. Here, we demonstrate that head-fixed and freely-moving behavior can be used equally well for vision research in this species. The two paradigms have different advantages and disadvantages: While the freely-moving paradigm lacks complete control over certain stimulus parameters (including viewing distance), it mimics natural behavior, requires no cranial

implants, and animals usually take to it quickly. It thus lends itself to studies requiring screening of larger cohorts of animals. The head-fixed paradigm, on the other hand, requires implants and takes longer to train, but provides complete control over viewing conditions. Because of the fixed head position, it also lends itself more easily to combined recording and behavior experiments, in particular if neural activity is to be recorded optically (e.g. using two-photon calcium imaging).

In the experiments described here, we controlled the animal's head position and distance relative to the screen, but did not attempt to monitor eye position. If the head-fixed setup is to be used to record neural activity in visual cortex while animals perform a task, maintaining the relative position of stimulus and center of gaze will be crucial to ensure that stimuli remain within the receptive fields of the neurons under study. Tracking of eye position is feasible in ferrets and could be added to the setup (Stitt et al., 2018). This – at the minimum – would allow monitoring of eye position during an experiment, which could be used to eliminate trials contaminated by saccades or large deviations in eye position from a desired location. Monitoring of eye position might also enable tasks in which ferrets are trained to fixate a target, which would more tightly control stimulus position. Fixation tasks likely will also be required to be able to present stimuli peripherally. Whether ferrets can indeed be trained to fixate a stimulus remains an open question to be investigated in future experiments. In any case, the addition of eye tracking to the setup will require the development of efficient strategies to calibrate the eye tracking signal, either by developing tasks that require ferrets to fixate targets presented at different positions, or through other automated procedures like the ones developed for eye tracking in rats (Zoccolan et al., 2010).

The second important conclusion derived from our experiments is that ferrets show clear behavioral evidence of higher-level visual processing, as indicated by their ability to perform motion and form tasks that require integration of information across multiple elements. The motion integration thresholds measured here are consistent with the results of a previous ferret study, in which animals were tested on their ability to discriminate coherent from random motion (Hupfeld et al., 2006). In this task, ferrets achieved a performance level of 75% correct for coherence levels of around 20%. These thresholds are lower than the thresholds of 30 - 37% determined here, most likely because of the simpler discrimination task. The studies also differ in other parameters such as the lapse rates and the number of trials performed per day, which might have affected the measured psychometric functions. Motion integration thresholds have also been measured in the cat, a carnivore like the ferret, using stimuli very similar to the ones employed here. Across two studies, motion integration thresholds for cats (measured either at 70 or 75% correct performance) ranged from 5 to 15% (Mitchell et al., 2009; Rudolph and Pasternak, 1996). These thresholds are lower than the ones measured for ferrets here, which could indicate that cats are better able to integrate motion signals, but might also be due to differences in the amount of training animals received in the different studies.

Ferrets were similarly able to perform a form integration task. Note that we chose to use linear rather than concentric Glass patterns here to more closely match motion and form tasks. In human subjects, thresholds for linear Glass patterns differ from those for more complex patterns containing curvature, such as concentric Glass patterns (Wilson and Wilkinson, 1998; Wilson et al., 1997). It has been proposed that this difference arises because

Glass patterns containing curvature tap into the curvature tuning in higher-level areas like V4 (Gallant et al., 1993; Pasupathy and Connor, 1999, 2001). Yet, these conclusions might be confounded by effects of viewing Glass patterns through circular apertures, as is commonly the case (Dakin and Bex, 2002). Nonetheless, probing form integration in ferrets with curved Glass patterns remains an interesting topic for future investigations.

Generally, processing of RDK and Glass patterns has been associated with higher-level visual areas. In monkeys, area MT in particular has been considered central for the processing of RDK (Britten et al., 1992; Newsome and Pare, 1988; Salzman et al., 1990). One important reason for this conclusion is the close agreement between neurometric functions of MT neurons and behaviorally measured psychometric functions (Britten et al., 1992; Shadlen et al., 1996). In contrast to the primate studies, we have not yet recorded neurons and behavior simultaneously in ferrets. As we have recently shown, PSS is a higher-level motion area exhibiting similar degrees of motion integration as MT (Lempel and Nielsen, 2019). These findings, combined with the close agreement of psychometric and PSS neurometric thresholds observed here, support the notion that performance on the RDK task indeed depends on higher-level visual areas in ferrets as in primates. This would also be consistent with the observation that PSS lesions impact ferrets on a motion detection task using RDK (Hupfeld et al., 2007). Comparisons to the cat further support this argument, as lesions of cat suprasylvian sulcus – a region containing motion areas that are likely closely related to ferret PSS (Philipp et al., 2006)– similarly disrupts motion integration thresholds (Rudolph and Pasternak, 1996). Ferrets ability to perform the form integration task then raises the intriguing possibility that

there is a matching higher-level visual area for form processing, to be located in future experiments.

Finally, it should be noted that testing ferrets on RDK and Glass patterns required certain adjustments – in particular an increase of the dot sizes – relative to experiments in humans and non-human primates to accommodate their poorer visual acuity. Our own experiments estimated peak contrast sensitivity to fall around 0.18 cpd, and a maximum acuity of 0.65 cpd. As discussed above, these behavioral acuity estimates are consistent with spatial frequency tuning curves of area 17 neurons in ferrets (Baker et al., 1998). They also agree with an earlier behavioral study testing the ability of ferrets to detect gratings of different spatial frequencies and contrasts (von Melchner et al., 2000).

In conclusion, our experiments firmly establish the feasibility of visual psychophysics in ferrets, including on experiments thought to tap into higher-level visual functions. RDK and Glass patterns have been used previously to study the development of motion and form vision pathways in monkeys and humans (Grinter et al., 2010; Kiorpes et al., 2012; Maurer and Lewis, 2018). Our findings open the door to perform similar experiments in ferrets. Because of their early birth (Sharma and Sur, 2014), and the ability to systematically alter visual experience during development (e.g., Chapman and Gödecke, 2000; Chapman and Stryker, 1993; Li et al., 2006; Van Hooser et al., 2012; White et al., 2001), this presents exciting opportunities for future developmental research.

3 Chronic two-photon imaging in the ferret

3.1 Introduction

Since its invention 30 years ago, two-photon microscopy (Denk et al., 1990) has become an invaluable tool to neuroscientists. Specifically, the combination of genetically encoded calcium indicators and two-photon imaging has permitted high temporal and spatial resolution of neural activity in living tissue for up to several months (Chen et al., 2013b). Thus, two-photon imaging has offered neuroscientists unique opportunities, including the ability to collect spatial temporal profiles of neural population activity, and the ability to visualize dendritic spines and axonal branching.

These features of two-photon imaging render it an especially useful tool for studying learning and development, where neural plasticity is of paramount interest. A rising animal model in both of these fields is the ferret. The ferret is highly altricial, with litter sizes of 5-12 kits, making the ferret an advantageous model for studying both normal development and developmental disorders (Lohse et al., 2019; Sharma and Sur, 2014). Additionally, ferrets have been shown to be capable of complex visually-guided behaviors (Doty et al., 1967; Dunn-Weiss et al., 2019a; Hupfeld et al., 2006; Pollard et al., 1967) and decision making tasks (Zhou et al., 2016), which makes them a good model for studying learning.

Two-photon imaging has been leveraged in the ferret previously in order to study visual development (Chang et al., 2020; Li et al., 2008; Smith et al., 2015, 2018) using a chronic implant that has led to highly successful imaging in ferret kits (<45 days old) for up to two weeks (Smith and Fitzpatrick, 2016). Yet, imaging in the adult ferret faces substantial additional challenges. In general, ferrets have an opaque dura, which needs to be removed prior to

imaging. In the adult ferret, the dura is thicker than in the kit, and once it is removed, thick tissue originating from the borders of the durotomy and craniotomy will grow over the exposed brain. To further complicate matters, while developmental epochs are contained to 1-2 week periods, the time-course of learning, as well as the investigation into its long-term effects, often require a substantially longer period of study. Thus, the health of any chronic cranial window must be maintained for a longer period of time. Therefore, we developed a chronic imaging implant that was specifically designed for long-term imaging on the order of months, and which was optimized for use in adult ferrets. Here, we present the design specifications and considerations for our imaging chamber implant, outline the implant procedure, and demonstrate imaging of neurons in area 18 of an awake ferret across 9 weeks. This work lays important technical groundwork for future chronic two-photon imaging studies in the adult ferret.

3.2 Methods

3.2.1 Animals

All procedures were approved by the Johns Hopkins University Animal Care and Use Committee and conducted in accordance with the guidelines given by the National Institute of Health. A total of four ferrets were implanted with iterations of the chronic imaging chamber design, and the data of one ferret is shown in the results.

3.2.2 Artificial dura & imaging chamber design

Each artificial dura (Figure 3.1A-C) was made out of KE-1300T/CAT-1300 silicone (Shin-Etsu Silicones) using a custom mold made from stainless steel and plastic (Figure 3.1D,E). 1mL

of KE1300T was mixed with 0.1mL of CAT-1300, and the mixture was de-gassed via a centrifuge at 3500 rpm for 2-3 minutes. The silicone was then poured into the mold and secured with a clamp. The silicone was cured at 50°C for 2 hours. After curing, the artificial dura was removed from the mold using forceps, placed on transfer paper, and stored in a dust-free environment. Before implantation, each artificial dura was gas-sterilized.

The imaging chamber, stabilization ring, cap, and canula were custom made out of stainless steel (Figure 3.2A). The canula additionally had a 5mm #1 thickness glass coverslip (Warner Instruments, CS-5R) at the base, which was glued with Norland Optical Adhesive 61 (Thor Labs). The thickness of the canula flange, as well as the thickness of the base of the imaging chamber, were 0.25mm. Before implantation, the imaging chamber, stabilization ring, cap, and canula were sterilized in a steam autoclave.

3.2.3 Survival surgical procedure

All implant surgeries were performed under isofluorane anesthesia and followed sterile procedures. Anesthesia was induced with ketamine (40mg/kg, IM) and maintained with isofluorane (2-3%). Atropine (0.04mg/kg, IM) and Buprenex (0.015mg/kg) were administered pre-operatively. The ferret was intubated to maintain a clear airway under anesthesia and to monitor the CO2 waveform. EKG, SPO2, temperature, and jaw tone were also monitored continuously and recorded manually every 15 minutes. Lactated-ringer solution was delivered IV or subcutaneously to maintain appropriate electrolyte balances under anesthesia. Ferrets were given wet food post-operatively for the first 1-3 days after the implant surgery, and were treated with pain-relieving drugs (Buprenex at 0.3mg/kg, BID, IM, and Ostilox, PO) for 3 days post-operatively. The Ostilox dosage was 0.2mg/kg SID on the first post-operative treatment

day and 0.1mg/kg SID for the following two days. Antibiotics were administered for a total of five days, beginning the day before the surgery. Clavamox (15mg/kg, BID, PO) was administered for the head-post implant surgery, and Trimethoprim/Sulfamethoxazole (30mg/kg, BID, PO) was administered for the artificial dura and imaging chamber implant. Dexamethasome (1mg/kg, SID, IM) was also administered during the artificial dura implant and tapered off afterwards by halving the dose over two days. Additionally, the animal's food intake, weight, hydration, mood, and behavior were observed daily. In general, ferrets did not show signs of pain following either the head-post implant or imaging chamber implant procedures.

All virus injections were performed under anesthesia, induced and maintained as described above. We performed two types of virus injection surgeries. For ferrets with chronic imaging implants, virus injections were performed through the artificial dura after the chronic imaging window was implanted. Other than Ketamine, Atropine, and isofluorane, no additional drugs were administered. Two weeks prior to acute imaging experiments, a virus injection surgery proceeded as follows. A craniotomy was made over V1, 8mm lateral to the midline and 5mm anterior to the occipital ridge. A durotomy was made for each injection site. After virus was injected, the craniotomy was closed with tecoflex (Specialty Extrusion Inc.) and gelfoam (Pfizer), and the skin was closed with 4-0 vicryl sutures (MWI Veterinary Supply). Ferrets were treated with pain-relieving drugs (Buprenex at 0.3mg/kg, BID, IM, and Ostilox, PO) for 3 days post-operatively. The Ostilox dosage was 0.2mg/kg SID on the first post-operative treatment day and 0.1mg/kg SID for the following two days. Clavamox (15mg/kg, BID, PO) was administered for a total of five days, beginning the day before the surgery.

3.2.4 Viral injections

GCaMP6f was expressed by injecting AAV1.syn.GCaMP6f.WPRE.SV40 (University of Pennsylvania Vector Core) into visual cortex, or alternatively by injecting a 1:1 mixture of AAV5.TRE3.GCaMP6f and AAV5.mThy1PSs.TtAad (Salk Institute vector core) (Sadakane et al., 2015). 5uL of virus were diluted with 2uL of sterile saline and mixed with approximately 0.3uL of a 5% solution of Fast Green (Sigma-Aldrich). Approximately 2uL of the diluted virus solution were injected into visual cortex across 2-3 different injection sites spanning approximately 2-4mm. At each site, virus was injected at 3-4 different depths spaced 100-300um apart, with the most superficial depth approximately 100-200um below the cortical surface. AAV1.syn.GCaMP6f.WPRE.SV40 was used for the acute experiments and AAV5.TRE3.GCaMP6f + AAV5.mThy1PSs.TtAad was used for the chronic experiments. Imaging was performed two weeks after the virus injection in acute experiments and beginning one week after the virus injection in the chronic imaging experiments.

3.2.5 Implant maintenance

The imaging implant was maintained through daily cleaning. First, the inside of the 3D printed well - and therefore the area outside and around the imaging chamber – was cleaned with alternating rounds of betadine and alcohol, applied with a sterile cotton swab. Next, the screw to the cap was removed to release any pressure inside the implant. Then the chamber cap was removed and dropped in a mixture of Alconox and water. Remaining debris was removed from the cap using a swab, and the cap was subsequently soaked in 70% ethanol. The inside of the chamber was cleaned with a sterile cotton swab and ethanol, taking care not to allow ethanol to enter into the craniotomy. Finally, the chamber was flushed with

approximately 20cc of sterile saline using a sterile syringe and a sterile glass pipette for suction. When imaging was performed, the implant was flushed both before and after imaging.

3.2.6 Imaging

Two-photon microscopy was performed with a Neurolabware microscope coupled to a Ti:Sapphire laser (Coherent Chameleon Ultra II). Scanbox (Dario Ringach, Neurolabware) was used for data acquisition. A 16x water-immersion objective (Nikon; 0.8NA) and a 20x dry objective (Edmund Optics; 0.6NA) were used. A moveable stage with three translational degrees of freedom and one rotational degree of freedom was used to position the objective perpendicular to the imaging region. Imaging was performed at an excitation wavelength of 920nm and a frame rate of 15.5Hz. Emission was collected using a green (510 nm center, 84nm band) filter (Semrock).

For acute experiments, two-photon imaging was performed under anesthesia following surgical preparatory procedures described previously (Lempel and Nielsen, 2019). Briefly, anesthesia was induced with ketamine (40mg/kg) and maintained with isofluorane (1-3%). A tracheostomy was performed, and an IV catheter was inserted into the jugular vein for fluid (2.5% dextrose in lactated Ringer's solution) and drug delivery. The animal was paralyzed with pancuronium bromide (15mg/kg/hr) and respiration was maintained with a ventilator (Ugo Basile). Neosynephrine and atropine eye drops (MWI Veterinary supply) were administered, and contact lenses (Robin Platt) were fitted to protect the animal's eyes. A craniotomy and durotomy was made over the injection site, and the brain was stabilized with a 5mm coverslip (Warner Instruments, CS-5R) and a drop of a 1.5% solution of agarose and water.

For chronic experiments, two-photon imaging was performed while the animal was awake. Before imaging, the animal was habituated to the setup for several weeks as described previously (Dunn-Weiss et al., 2019a). Briefly, habituation consisted of exploring the setup while unrestrained, and then spending brief periods of time in the setup while receiving reward to form a positive association with the setup. After habituation, the animal would sit calmly in the setup for up to 30 minutes.

All imaging was performed in a darkened room. Spontaneous neural activity was recorded, and eye position was not monitored.

3.3 Results

3.3.1 Artificial dura design

The adult ferret has a skull thickness of about 1.5mm, a subdural space of at least 0.5mm, and an opaque dura. Thus, unlike in murine species, where imaging may be performed through thinned skull and/or through the dura, imaging in the ferret requires both a craniotomy and a durotomy above the imaging region. The two greatest challenges to maintaining an imaging implant are protecting the brain from infection, and protecting the imaging region from unwanted tissue growth. We resolve these challenges with an artificial dura (Figure 3.1A). The artificial dura consists of a 0.5mm cylindrical wall of silicone that encases the craniotomy, attached to a sheet of thin silicone that slips under the bone (Figure 3.1B). We designed the flange (or brim of the 'top-hat') to be relatively thick in order to make the artificial dura more secure after implantation, and designed the center of the artificial dura to be thin so as to preserve optical clarity and permit injection through the artificial dura (Figure

3.1A). We found a thickness of approximately 22.5mils (0.54mm) to be optimal for the flange, while a thickness of approximately 10mils (0.24mm) worked well for the center of the imaging region. This 'top-hat' shape prevents the cortex from being exposed, and significantly contains unwanted tissue growth over the imaging region. In particular, leaving the walls of the artificial dura taller than the top of the skull ensures that new tissue growth, originating from either the periosteum or the dura, grows around the walls of the artificial dura without growing above it. We found a height of 3mm to work well for this purpose.

Figure 3.1 Artificial dura design (Opposite page)

(A) *Example artificial dura. The silicone in the flange of the artificial dura is approximately twice as thick as the silicone in the center of the artificial dura.*
(B) *Schematic of the artificial dura implant. The flange of the artificial dura slips under the bone, and the walls of the artificial contain the dura and bone, preventing tissue growth over the imaging region.*
(C) *Schematic of the artificial dura mold. Left: cross section of the mold, illustrating the insert which sets the height and thickness of the walls of the artificial dura. Right: Top view of the mold.*
(D) *Photos of the two-part mold base for the artificial dura. The outer donut sets the outer diameter of the wall, and the middle insert sets the wall thickness and height.*
(E) *Entire artificial dura mold assembled. The top of the mold is a flat plastic block with stacked pieces of clear tape that determine the thickness of the artificial dura.*

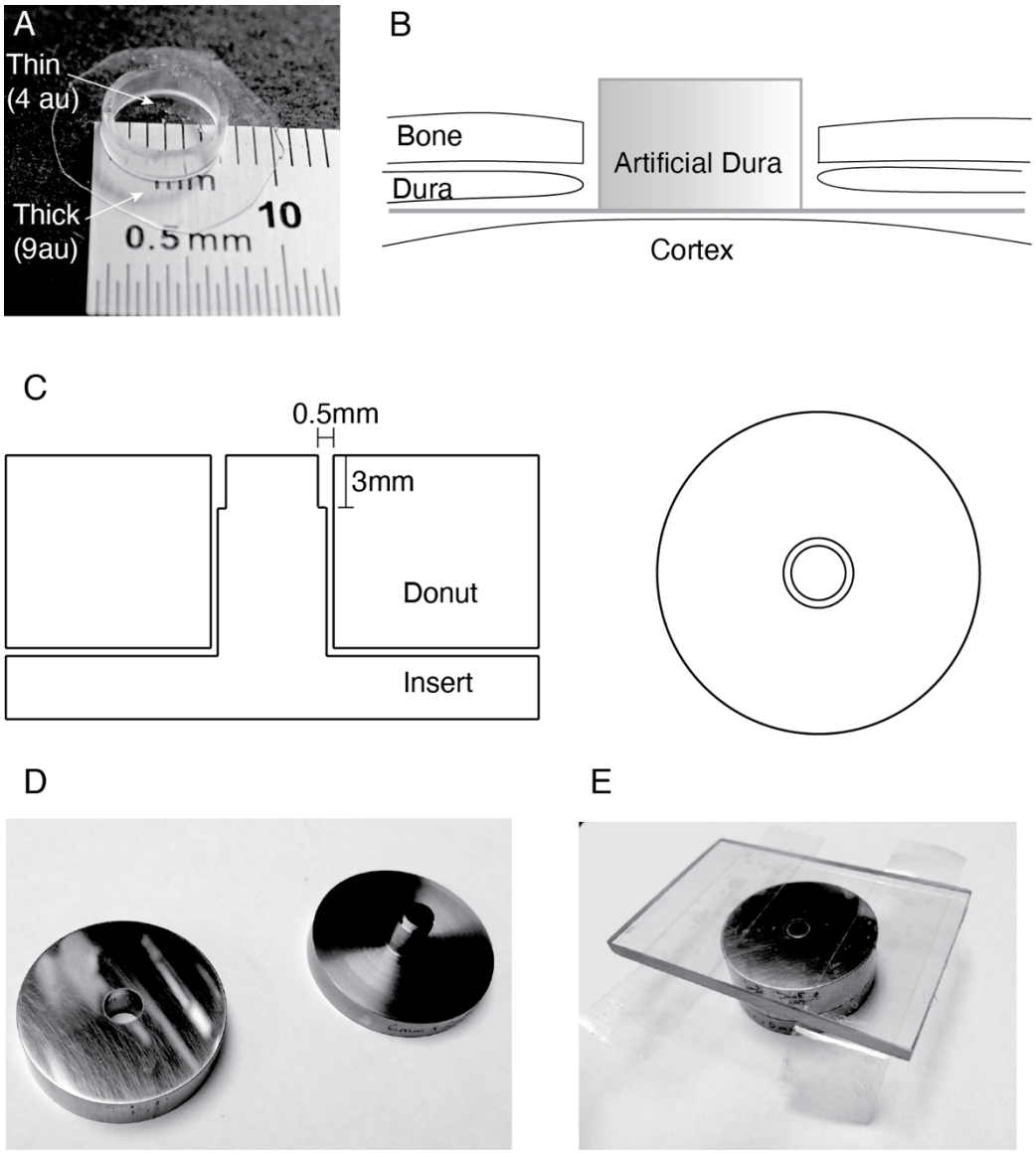

A custom mold is used to create the artificial dura. The custom mold consists of two parts: an outer donut, which sets the diameter of the outer wall of the artificial dura, and an insert that sets the height and inner diameter of the wall (Figure 3.1C,D). A piece of flat, clear plastic with layers of clear tape (Scotch® Transparent Tape) completes the mold, and is used to set the thickness of the artificial dura (Figure 3.1E). The thickness of the flange of the artificial

dura is equivalent to 9 pieces of transparent Scotch tape. To vary the thickness of the sheet of silicone between the center of the artificial dura and the flange, a 5mm diameter glass coverslip is taped to the center of the plastic block with transparent scotch tape. We use tape to adhere the glass coverslip to the plastic block for several reasons. First, the glass coverslip is fragile, and can shatter with pressure. Thus, adhering the coverslip with tape makes it easy to replace, and prevents glass shards from affecting the rest of the mold. Second, the height of the glass coverslip can be precisely controlled with tape, where glue applications could add more variation in height. Third, taping over the coverslip created a taper from the thinnest to thickest silicone. We found that using clear tape was important for ensuring that the surface of the artificial dura over the imaging region was smooth and uniform.

3.3.2 Chamber design

To complement the artificial dura, we designed an imaging chamber (Figure 3.2A). The imaging chamber performs two functions. First, the imaging chamber provides additional protection from unwanted tissue and bone growth into the imaging region. The base of the imaging chamber drops into the craniotomy (Figure 3.2B), providing a physical barrier between the periosteum and the artificial dura. Second, the imaging chamber provides a means of stabilizing the brain during imaging. We used a canula to apply even pressure on the imaging surface. To stabilize the canula, we designed a threaded stabilization ring that screws into the walls of the base of the imaging chamber (Figure 3.2C). Because the stabilization ring is threaded, the height, and therefore the amount of pressure applied by the canula may be manually adjusted. The canula in our design is adapted from Smith and Fitzpatrick to match the height of our artificial dura (3mm, Figure 3.2C) (Smith and Fitzpatrick, 2016).

In between imaging experiments, the canula is removed, and the chamber is closed with a lid, which threads into the stabilization ring (Figure 3.2A,B). The walls of the artificial dura fit within the inner walls of the lid so that the top of the lid does not press on the artificial dura (Figure 3.2B). Thus, the lid provides a means of protecting the cranial window of external debris while avoiding adding any pressure on the brain. The lid also features a pressure relief port, which ensures that the lid can always be removed safely.

Figure 3.2 Imaging chamber design (Opposite page)

(A) *Imaging chamber parts.*
(B) *Schematic of the imaging chamber when closed in between experiments. The base of the artificial dura slips under the dura and bone. The top of the artificial dura fits inside of the chamber lid such that the lid does not press down on it.*
(C) *Schematic of the imaging chamber parts for stabilization. A canula fits inside of the artificial dura, and is stabilized by a stabilization ring that screws into the imaging well.*

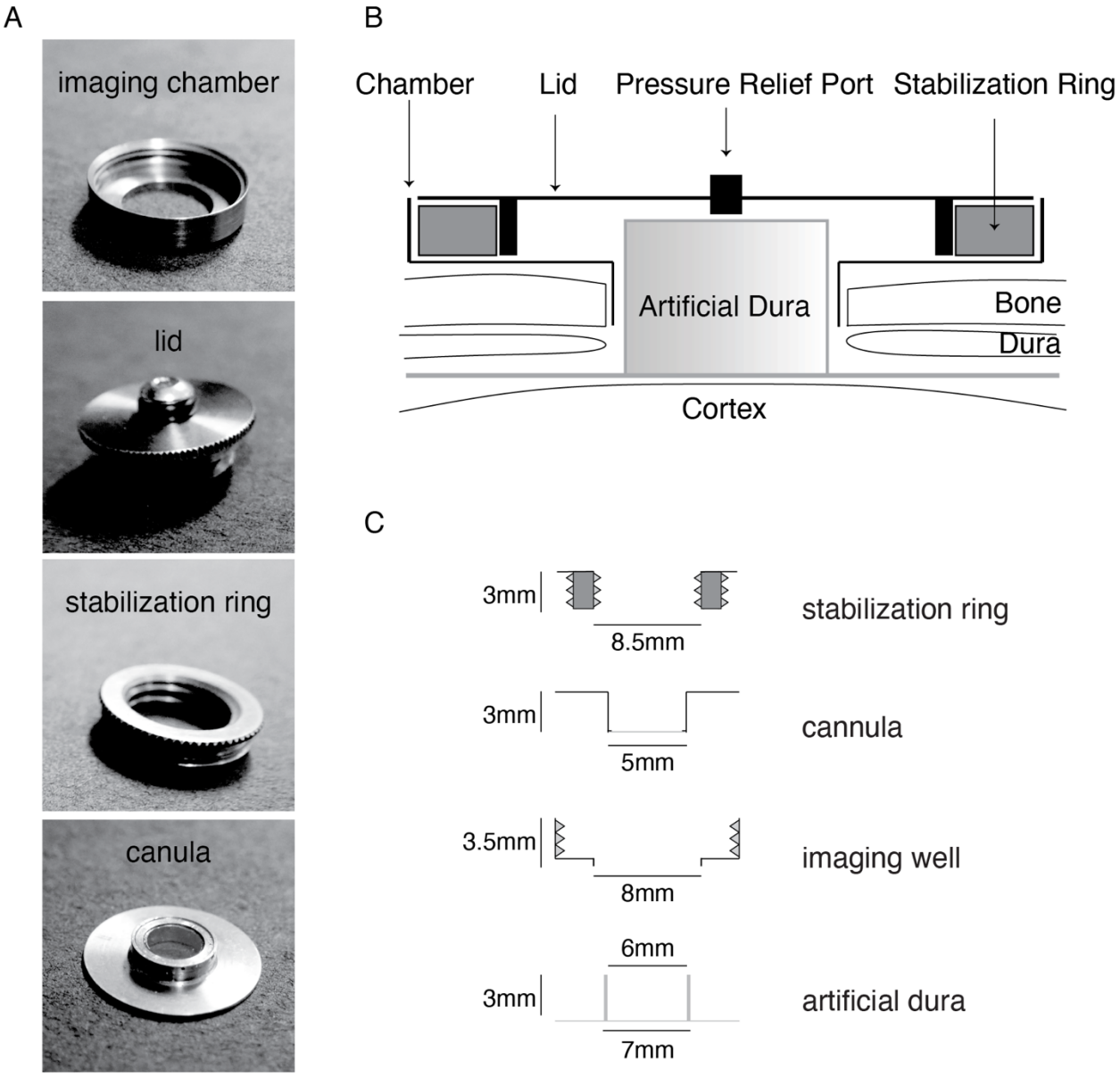

3.3.3 Design validation

Before implementing our design chronically, we set out to verify that, under ideal conditions, the optical quality of the imaging region was not compromised by the artificial dura and canula. We therefore implanted our design in a series of terminal experiments and imaged

under anesthesia. This ensured that no tissue had grown over the imaging region and avoided the possibility of body movement artifacts.

We first verified that imaging could be performed through the combination of a short 1.4mm artificial dura and canula with a Nikon 16x 0.80 wet objective. The Nikon 16x 0.80 objective is one of the most common objectives for two-photon imaging because of its combination of high numerical aperture and suitable magnification factor. We found that imaging through the artificial dura and canula produced crisp, clear images of cells, with high enough resolution and stability to visualize axons (Figure 3.3A).

Figure 3.3 Design validation and objective comparison (Opposite page)

(A) Imaging through the artificial dura and canula with the Nikon 16x 0.80. Cells and processes were clearly visualized.
(B-C). Comparison between the Nikon 16x 0.80 and the Edmund Optics 20x 0.60. **(B)** Imaging with the Nikon 16x 0.80. **(C)** Imaging the same region with Edmund Optics 20x 0.60. Boxes highlight clusters of the same cells that were visualized clearly with both objectives.

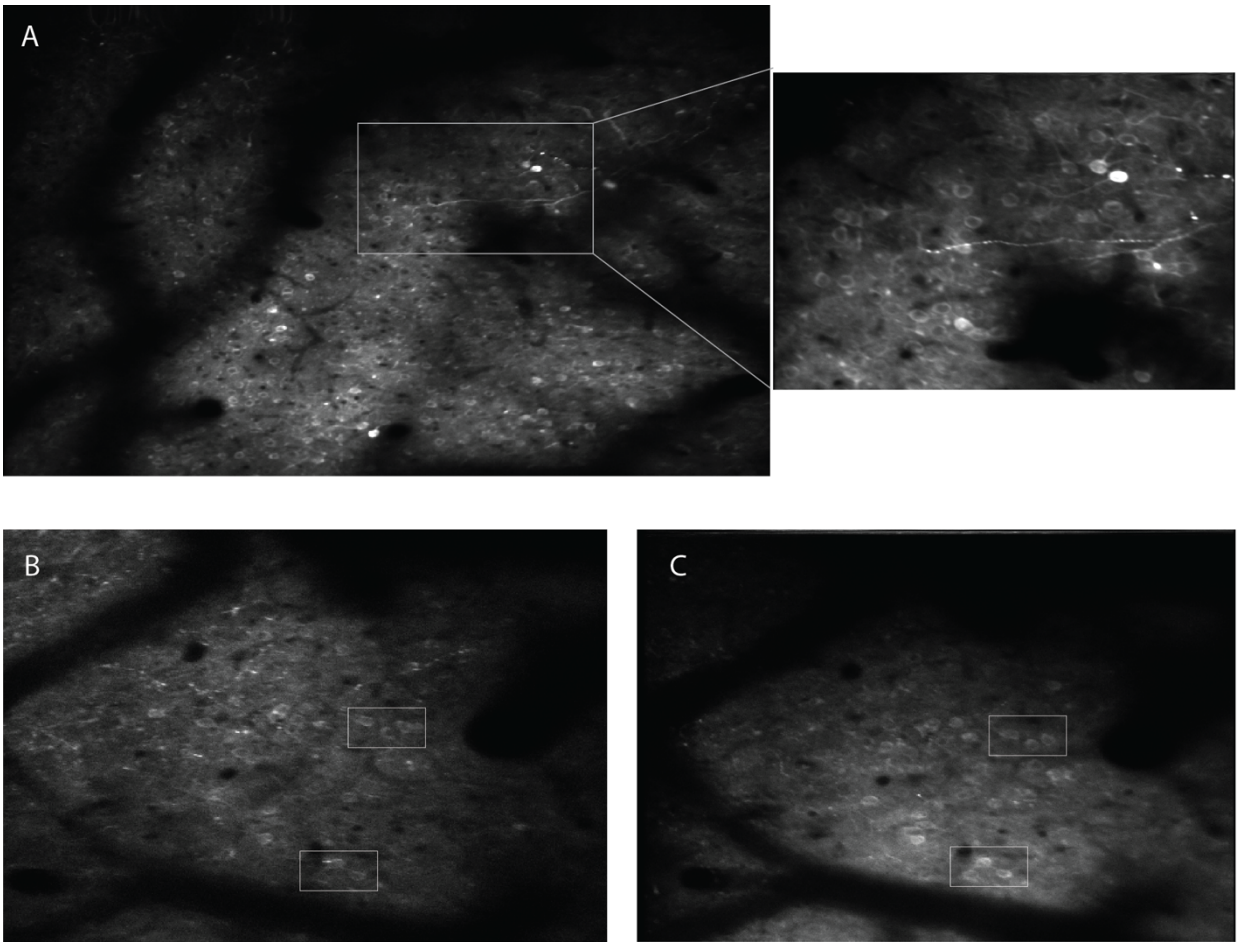

However, the Nikon 16x 0.80 objective has a working distance of 3mm, which significantly constrained the design possibilities for the imaging chamber. Most importantly, the working distance of the Nikon 16x 0.80 substantially limits the allowable height of the artificial dura. A tall artificial dura could prevent the front lens element of the objective from getting within 3mm of the imaging region, thus making it impossible to bring the imaging region into sharp focus. However, the shorter the artificial dura, the less effective it is at preventing unwanted tissue from growing into the imaging region.

To investigate whether this limitation could be circumvented, we compared the performance between an Edmund Optics 20x 0.60 dry objective and the Nikon 16x 0.80 wet

objective. While the Edmund Optics objective has a lower numerical aperture and consequently a lower optical resolution, it has a much higher working distance of 13mm. We found that this objective provided comparable optical quality to the Nikon 16x 0.80 wet objective in our in vivo application, which only required visualization of cell somata (Figure 3.3B,C). Specifically, when we compared the images taken with the Nikon 16x 0.80 with the images taken with the Edmund Optics 20x 0.60, we were able to visualize many of the same cells (Figure 3.3B,C), and observed comparable cell density. We therefore used the Edmund Optics 20x 0.60 objective for subsequent chronic imaging experiments.

3.3.4 Surgical procedure for chronic implantation

The surgical procedure for a cranial implant suitable for two-photon imaging consists of three parts. The first is to implant a head-post (Figure 3.4A) that could be used to head-fix the animal while performing imaging. The second is to implant the artificial dura and chronic imaging chamber. The last is to inject a viral vector driving expression of GCaMP6f into the imaging region. Dividing the implementation of the imaging chamber into three separate surgeries reduces the time that the ferret is continuously under anesthesia, which we found to be safer for the animal. Additionally, separating the head-post implant into its own surgery is advantageous for acclimating the animal to the head-fixed setup, or training on a behavioral task, before performing awake imaging (for a description of the head-fixed set-up used in this study, see Dunn-Weiss et al. 2019a). The following sections provide notes for each surgery, including details of the implant parts, positioning notes and general recommendations.

Head-post implant:

The first surgical procedure is the head-post implant. The head-post is secured in place using dental cement and anchored in place using T-bolts (Figure 3.4B) and anchoring screws. The T of the T-bolt drops into a linear craniotomy, is rotated 90° and is secured in place by a nut. This way, the T-bolt grips the bone firmly from above and below, providing a stronger hold than the threads of the anchoring screws alone. We implant T-bolts in the anterior portion of the skull where the bone is thickest (Figure 3.4C) and use anchoring screws otherwise. We found that it was best to implant head-posts with T-bolts in animals that are at least 12 weeks of age. In younger animals, the skull is thinner, and still growing.

Figure 3.4 Full implant schematics (Opposite page)

(A) *Images of the head-post.*
(B) *Left: Images of the T-bolts. Right: Schematic of T-bolt implantation. Top: The T of the T-bolt (black line) drops into a linear craniotomy, is rotated 90° (indicated by the dashed line), and then secured in place with a nut (gray square). Rotating the T-bolt 90° and securing it with a nut 'locks' the T-bolt in place. Bottom: T-bolts drop below the bone, so that together, the nut (gray rectangle) and the T of the T-bolt grip the bone securely from two sides. To ensure that the T-bolt stays securely in place, the nut is embedded in acrylic.*
(C) *Drawing of the position of the head-post, T-bolts, anchoring screws, and imaging chamber on the ferret skull. The occipital ridge and midline are used as visual landmarks (dashed black lines). Squares indicate T-bolts, filled in circles indicate anchoring screws, the open circle indicates the imaging chamber craniotomy, and the inverted T indicates the head-post.*
(D) *Image of the 3D-printed well. The cut-out accommodates the original head-post implant, and the shape is designed to mimic the natural curve of the muscle.*
(E) *Schematic drawings of the 3D printed well. The height of the well was designed to be as short as possible.*

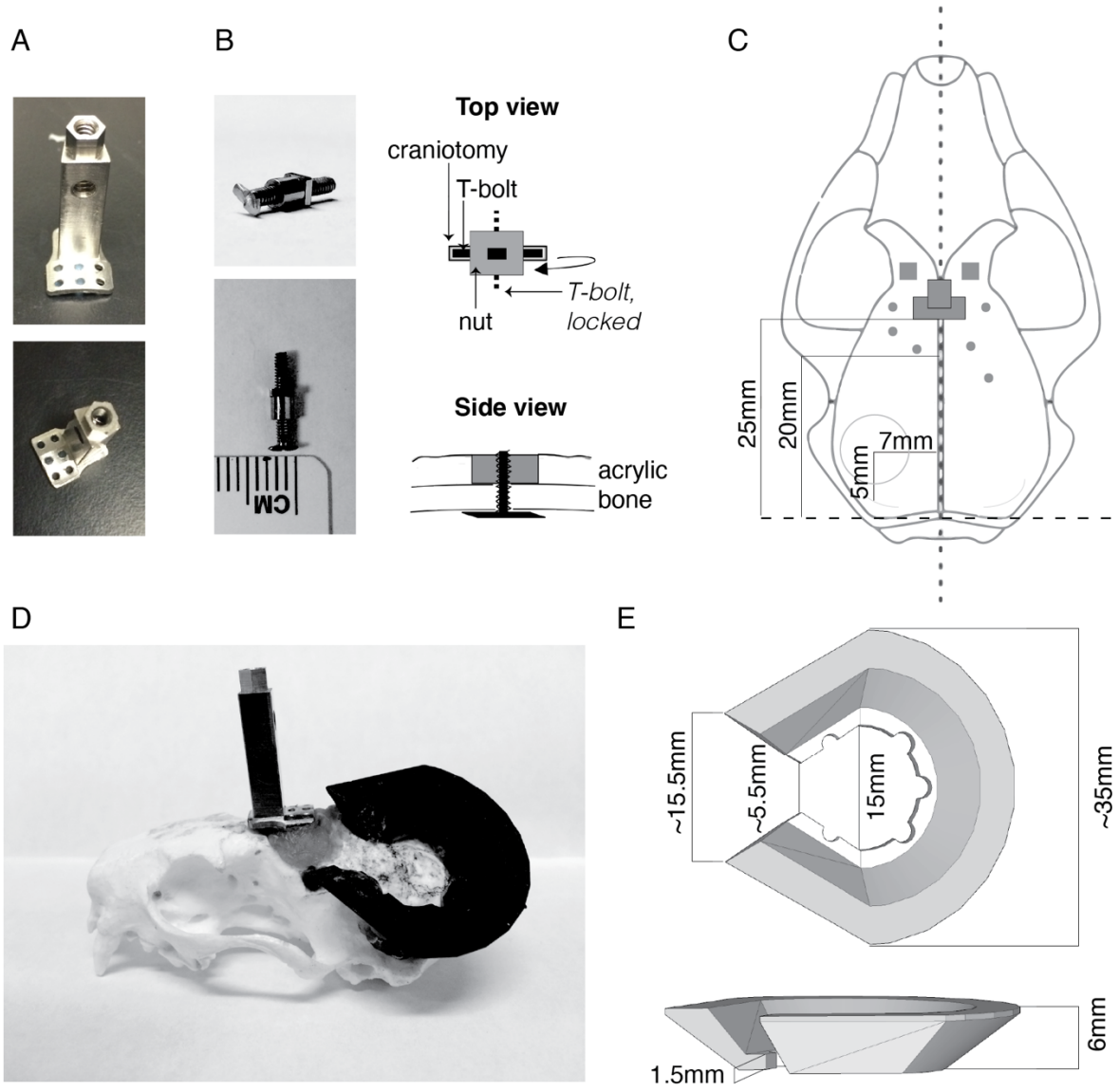

The T-bolts are custom made, derived from 0-80 3/8" head cap screws (McMaster-Carr). The anchoring screws (McMaster-Carr) should be approximately 3mm in length, and rounded at the end to minimize the risk of irritation or injury. With a length of 3mm, the screw can be secured such that the thread spans the thickness of the skull, while the head of the screw remains above the surface of the skull. The height of the head of the screw (approximately 1.5mm) is such that the dental cement can securely attach to it, while the overall implant does

not have to be particularly tall in order to embed the screws entirely in dental cement. We found that Metabond (Parkell Inc.) was an ideal cement for securing the head-post in place. It has a long work-time, is easy to shape into smooth implants, and is especially strong. We treated the bone with Copalite (Henry Schein Dental) before applying Metabond as an extra measure to inhibit tissue growth.

For imaging over area 17/18 of visual cortex, the head-post should be positioned as anteriorly as possible to avoid mechanical interference with the imaging chamber implant. In our experience, the optimal position of the head-post was approximately 2.5 cm anterior to the occipital ridge (3. 4C, dashed horizontal black line). The optimal location for implanting the T-bolts is just posterior to the 'V' formed by the external sagittal crest in the rostral portion of the ferret skull (Figure 3.4C). Anchoring screws should be positioned around the lateral and posterior perimeter of the head-post to minimize the footprint of the implant, particularly on the hemisphere where the imaging chamber will be implanted. In our implants, the most posterior screw on the imaging hemisphere is positioned 2 cm anterior to the occipital ridge.

With this design and protocol, we found that the head-post implant could last for a year or longer without any complications. The head-post implant on its own requires minimal maintenance. In many implants, the hair that grows back around the head-post actually protects the wound edge. By keeping a small footprint for the head-post implant, which minimally exposes the posterior lateral portion of the skull, the integrity of the bone is well-preserved, and no new tissue growth is typically observed over the posterior lateral portion of the skull. Copalite and Metabond cement also seem to be particularly effective at preventing

tissue growth beneath the cement. Post-mortem evaluation of the skulls of ferrets with implants showed minimal decalcification under the implant.

Imaging chamber implant:

The second surgical procedure is the imaging chamber implant. The craniotomy for the imaging chamber implant must be as precisely circular as possible in order to match the outer diameter of the imaging chamber (8.5mm). One way to achieve this is to lightly mark the perimeter of the craniotomy with a trephine, and to finish the craniotomy with a standard drill bit. Alternatively, an 8mm coverslip may be used as a guide for tracing the perimeter of the craniotomy. For this approach, an 8mm coverslip is loosely attached to the bone with bonewax, and its perimeter is traced in pencil. Drilling just within the pencil line typically produces a good fit with the chamber. For imaging over area 17/18, the center of the craniotomy should be approximately 7mm lateral to the midline and 5mm anterior to the back of the brain (Figure 3.4C). Once the craniotomy for the imaging chamber is made, the chamber is secured in place with Metabond dental cement.

After the imaging chamber implant is in place, a durotomy is made and the artificial dura is inserted. There are three important elements for a successful artificial dura implant. First, because the outer diameter of the artificial dura is smaller than the inner diameter of the imaging chamber, it is useful to leave excess dural tissue that may be used to secure the position of the artificial dura. Leaving excess dural tissue also makes it easier to visualize the flange of the artificial dura slipping below the surrounding dura. Second, it can be useful to customize the flange of the artificial dura according to where it will be implanted. For our

application, it was helpful to trim the portion of the flange of the artificial dura that was inserted towards the back of the brain to be short, approximately 1mm in length. Customizing the flange of the artificial dura can be done easily by cutting through the artificial dura and its transfer paper backing at the same time with fine surgical scissors. Finally, to further secure the position of the artificial dura and prevent tissue from growing into the space between the artificial dura and the inner perimeter of the chamber, a thin bead of Kwik-Sil silicone (World Precision Instruments) should be added around the outer perimeter of the artificial dura at the point where it meets the imaging chamber.

The entire imaging chamber implant is embedded in a cement cap, which is integrated into the original head-post implant footprint. To expedite the process of building this cap, we designed a well that could be 3D-printed and incorporated into the head-cap (Figure 3.4D,E). The well is designed such that the inner diameter of its footprint is just larger than the imaging chamber, with a scalloped edge that increases its adherence to the skull with cement. The height of the well is 6 mm, which is short enough to accommodate the working distance of the Edmond Optics 20x 0.60. The well is tear drop shaped to mimic the curve of the muscle. A cut out at the top of the tear drop accommodates the base of the headpost. Finally, because the well is 3D printed, it may be printed in black, which increases its contribution to light shielding. However, for the data shown in this paper, the well was printed in white (Objet Printer, VeroWhitePlus).

Viral injection:

The last surgery in the sequence is the virus injection surgery used to express GCaMP6f. A noteworthy feature of our artificial dura is that the glass pipettes that we commonly use for

virus injections are able to penetrate the material without permanently damaging or breaking the seal of the artificial dura (Figure 3.5). Therefore, the virus injection is performed after the artificial dura is implanted, allowing approximately one week of recovery between surgeries. We use glass capillaries (World Precision Instruments, 1B120F-4) to pull pipettes using a horizontal pipette puller (Sutter Instruments), and cut tips to approximately 25um. We then beveled the pipettes at approximately a 20-30° angle. These sharpened pipettes were able to easily penetrate the artificial dura, and the silicone of the artificial dura resealed itself upon withdrawal of the pipette. By mixing Fast Green with the viral vector (less than 0.5uL mixed with 5uL of virus and 2uL of sterile saline), the spread of the virus injection could be visualized easily through the artificial dura (Figure 3.5).

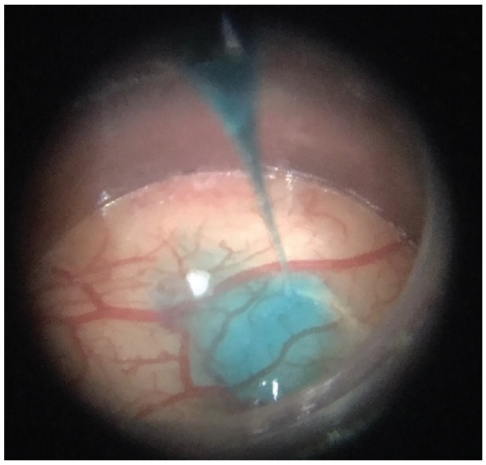

Figure 3.5 Viral injection through the artificial dura

Image of the virus pipette penetrating the artificial dura during a virus injection. Fast Green was used to visualize the spread of the virus.

The imaging results shown below are the results of a single virus injection, performed one week after implanting the imaging chamber. However, because the artificial dura is permeable to injection pipettes and resealable, repeated injections are possible.

3.3.5 Chronic implant results: Implant health & visualization of cells over time

Figure 3.6A shows the implant after 1 week, immediately after injecting virus (AAV5-TRE-GCaMP6f + AAV5-mThy1S-tTA). The imaging region remained clear for approximately 8 weeks after implantation, at which point a vascularized neomembrane began to grow over the region. However, the neomembrane could be removed, and the artificial dura replaced. Figure 3.6B shows the implant after 10.5 weeks, immediately after the neomembrane was removed and the artificial dura was replaced.

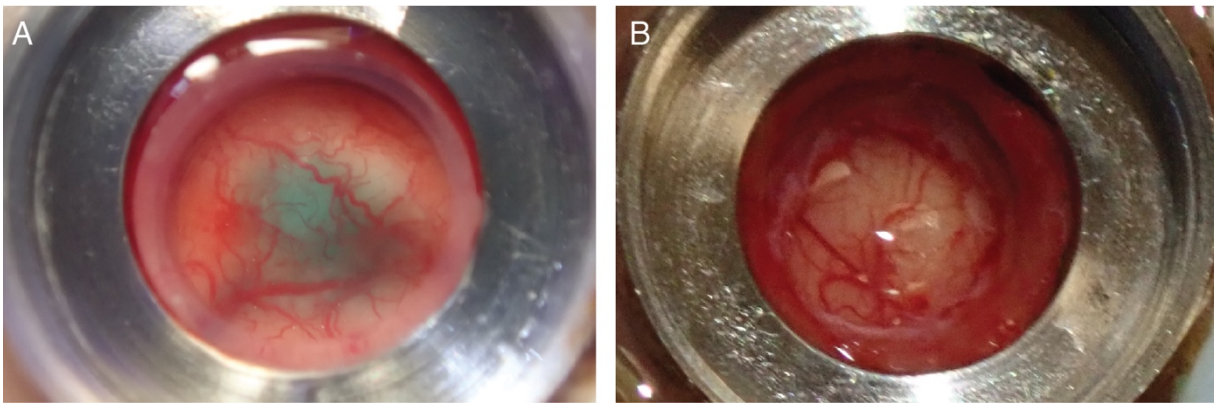

Figure 3.6 Implant health over time

(A) *Photo of the cortex taken immediately after injecting virus, approximately 1 week after the artificial dura and imaging chamber were implanted.*
(B) *Photo of the cortex taken 10.5 weeks after the implant surgery, immediately following surgical removal of the neomembrane.*

In addition to monitoring implant health, we also performed awake chronic two-photon imaging of spontaneous neural activity to see how long we were able to visualize cells. During

imaging, the ferret was head-fixed in the behavioral setup described in Dunn-Weiss et al. 2019a. After cleaning the implant and inserting the canula, the room was darkened, black out material was draped around the ferret for light shielding, and cells were located under the two-photon microscope while the ferret rested in the setup. Two-photon imaging grabs of 300-500 frames were collected of each imaging region, and the mean florescence across these frames was used to generate images of cells. Figure 3.7A-C shows images of cells collected at 3 weeks, 6 weeks, and 12 weeks after the injection, respectively. Cells were visualized clearly during these three months. However, by 12 weeks it was more difficult to distinguish cells against the background fluorescence of the tissue, fewer cells were visible overall, and there appeared to be more apoptotic cell fragments.

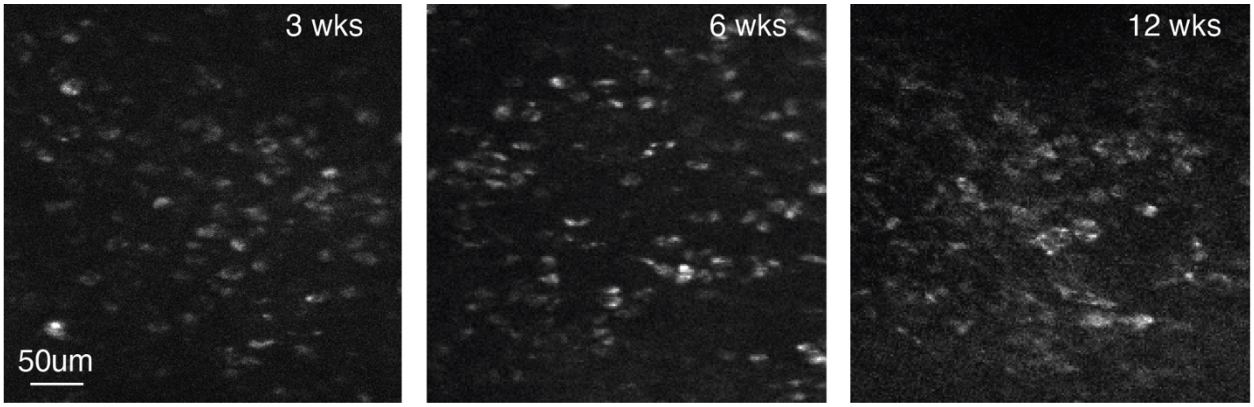

Figure 3.7 Two-photon data over time

(A) *Two-photon imaging of cells 3 weeks after injecting virus.*
(B) *Two-photon imaging of cells 6 weeks after injecting virus.*
(C) *Two-photon imaging of cells 12 weeks after injecting virus. Scale bar is 50 um.*

3.4 Discussion

Here, we present an imaging chamber implant design and surgical procedure for the adult ferret, and provide the first demonstration of long-term, awake chronic imaging in the ferret over several months. Our design is distinguished by two important features: an artificial dura that protects the imaging region from tissue growth, and a threaded stabilization ring that allows for variable pressure on the brain to reduce motion artifacts during imaging.

3.4.1 Features and design considerations of the artificial dura

One of the central challenges of chronic imaging in larger animals is establishing and maintaining a clear optical window. In large animals such as ferrets and primates, the dura is opaque, and must be removed prior to imaging. Approaches to sealing the durotomy can broadly be divided into two categories: sealing the durotomy with a glass coverslip (Ikezoe et al., 2013; van Kerkoerle et al., 2018; Sadakane et al., 2015; Santisakultarm et al., 2016; Smith and Fitzpatrick, 2016), or sealing the durotomy with an artificial dura (Arieli et al., 2002; Chen et al., 2002; Heider et al., 2010; Shtoyerman et al., 2000; Yamahachi et al., 2009). The artificial dura and coverslip have also been combined into a single approach: Li and colleagues created a titanium ring with a coverslip to fit into the craniotomy, and attached an artificial membrane around the external perimeter to slip under the dura (Li et al., 2017).

The primary advantage of an artificial dura is that it slips under the dura, which can prevent tissue originating from the dura or periosteum from growing into the imaging region. We therefore elected to incorporate an artificial dura into our design. We chose to incorporate

an artificial dura that is made entirely of flexible material, thereby limiting the amount of pressure on the cortex between imaging experiments. Our implementation of an artificial dura is similar to artificial dura implants developed for macaques (Arieli et al., 2002; Chen et al., 2002; Shtoyerman et al., 2000). Notably, we use a moldable silicone for the artificial dura that permits penetration with fine beveled glass pipettes. Such penetrations leave the artificial dura intact: the silicone reseals itself once the pipette is removed. In the present work, we leveraged this feature in order to inject adeno-associated virus for local expression of GCaMP, but it could also be used to express other constructs, such as opsins that could then be stimulated through the cranial window (Ruiz et al., 2013).

There are two important considerations when implementing the artificial dura: determining how thick the silicone above the imaging region should be, and determining the height of the artificial dura. Here, we show that imaging through silicone with a thickness of approximately 10mils yields crisp images of neural cell bodies and even processes. In addition to optical clarity, we found that a thickness of at least 7.5mils helped the artificial dura lie flat above the cortical surface and provided sufficient tensile strength for easy handling prior to insertion. However, because the thickness of the artificial dura is set by stacked pieces of clear tape, our design allows the thickness of the artificial dura to be varied for other applications.

The height of the artificial dura used to collect the data shown here was chosen to be 3mm. Earlier iterations of our design implemented a shorter artificial dura, with a height of approximately 1.5mm. However, we found it more difficult to manage tissue growth with this shorter artificial dura. Incorporating a taller artificial dura, and adding a bead of Kwik-Sil to seal

the gap between the artificial dura and the walls of the imaging chamber slowed tissue growth around the artificial dura overall.

However, a tall artificial dura with a relatively small inner diameter (i.d.) requires an objective with a relatively large working distance. We found the Edmund optics 20x 0.60 dry objective, with its 13mm working distance, to be a good option for our application. Though the Edmund optics objective has a lower numerical aperture than the more standard Nikon 16x 0.80NA, we found that its ability to resolve cell somata was comparable to the Nikon objective. Nevertheless, the lower numerical aperture, and the corresponding resolving power limit of 56um, might pose a challenge for more fine scale imaging of dendritic spines. Thus, unless a dry objective with a high numerical aperture and a sufficiently long working distance becomes available, future implementations of our design that require higher resolving power might incorporate a shorter artificial dura, or one with a larger inner diameter.

Independent of these design considerations, a unique and innovative element of our artificial dura is that the flange is thicker than the center. A relatively thin center to the artificial dura is necessary for optical clarity. At the same time, the thick flange makes the artificial dura much more secure when it slips under the dura and bone, and further closes the gap where tissue could grow. To our knowledge, our artificial dura is the first to exhibit both of these features. With this design, we show that we are able to maintain a healthy implant for up to three months.

3.4.2 Stabilization methods

Performing two-photon imaging requires a stabilization method to prevent motion artifacts. Even minor fluctuations of the position of the brain that result from cardiac and

respiratory rhythms are large enough to move the imaging region out of the focal plane. In our design, we stabilize the brain using a canula and an adjustable stabilization ring. The canula offers the advantage of applying pressure directly to the surface of the artificial dura with little to no degradation in optical clarity (Smith and Fitzpatrick, 2016). Alternative stabilization approaches have used a simple glass coverslip and a retaining ring (van Kerkoerle et al., 2018; Li et al., 2017; Smith and Fitzpatrick, 2016), and filled the space between the cortex and the coverslip with agarose, silicone, stacked glass coverslips, or have left the space unfilled. However, these alternatives allow for less control over the pressure applied to the brain, and in some cases could introduce optical aberrations. For optimal stabilization, depressing the imaging region slightly by about 0.5mm is required (Smith and Fitzpatrick, 2016). Therefore, our design uses a threaded stabilization ring that can modulate pressure by modulating the height of the canula.

With this stabilization method, we were able to collect highly stable images of cells. In our experience, small shifts in the ferret's body position did not change the plane of cells that were in focus, and the imaging plane of interest remained stable for imaging sessions that lasted up to 20 minutes. Additionally, small lateral displacements within the focal plane were correctable through offline image processing with Scanbox. Even large-amplitude motion artifacts (e.g. larger scale body movements during certain phases of the trial such as reward collection) caused only a temporary disruption in the alignment between the imaging plane of interest and the focal plane. Thus, our stabilization method appears to be effective at mitigating many movement-related artifacts.

Nevertheless, the movements of awake animals can be unpredictable, and our stabilization system does not eliminate motion artifacts altogether. For body-movements that displace the imaging region along the Z-axis, additional motion correction methods are needed. Volumetric scanning – collecting imaging data as a stack of imaging planes along the Z-axis – has been used to align the imaging volume to a fixed reference during imaging (Chen et al., 2013a; Griffiths et al., 2020; Laffray et al., 2011), or to perform motion correction offline post-hoc through 3D cross-correlation analysis (Andermann et al., 2010; Kerlin et al., 2010). Future work implementing our design in an awake and behaving ferret would benefit from the addition of one of these motion correction methods. In particular, recent advances in inertia-free 3D random access pointing and scanning present an exciting opportunity for online motion correction with a minimal time cost (Griffiths et al., 2020).

3.4.3 Limitations and future directions

The main focus of the present work was to develop the basic implant and test its long-term health and viability for two-photon imaging. However, there are two notable aspects to long-term two-photon imaging that are not addressed by this work. First, future work is needed to demonstrate the ability to return to the same cells across days. Mounting the head-fixed setup on a series of stages, and using of kinetic markers on the canula that could be used for manual or automatic alignment (Choi et al., 2018) is one possible avenue. As an alternative or to complement these mechanical efforts, volumetric scanning could allow for post-hoc localization of the same cells. A data plane intersecting a volume of imaging data could be defined at any angle, and therefore need not be parallel to the imaging surface. However, the

temporal resolution of volumetric scanning is less than planar scanning. Thus, volumetric scanning is not ideal for all applications.

The second limitation of our results is that our data was collected while the ferret was resting, in the absence of visual stimulation. Although the ability to image cells for up to 9 weeks demonstrates that the implant could be maintained free of infection or unwanted tissue growth, the health of the neurons in the imaging region is unknown. Long-term chronic expression of AAV2/1-GCaMP6 or AAV2/1-GCaMP3 has been shown to disrupt calcium homeostasis in some of the transfected cells, the proportion of which grows over time (Chen et al., 2013b; Tian et al., 2009). These cells are distinguished by nuclear fluorescence, and exhibit aberrant response properties. In our data, we observed a notable proportion of cells with nuclear fluorescence across the entire duration of our experiments (Figure 3.7). Thus, follow up investigations are needed in order to investigate the response properties of neurons transfected with GCaMP over time in the ferret, and how different serotypes – which impact the extent of expression and the amplification of the fluorescent signal – impact long-term neuronal health.

3.4.4 Conclusion

Our implant design allowed us to maintain a healthy chronic cranial window in an adult ferret for 3 months, and to visualize cells across 9 weeks. Our results contribute a significant step forward for chronic two-photon imaging in ferrets across all ages. This opens the door for research into learning, the long-term effects of abnormal development, and slowly-evolving developmental trajectories such as aging. Finally, our design allows for optogenetic

manipulations in the awake ferret, thus opening the door for experiments that probe the relationship between neural activity and behavior with far-reaching applications.

Acknowledgements: This work was supported by NeuroNex NeuroTechnology Hub-Nemonic: Next generation multiphoton neuroimaging consortium; NSF; 1707287. We thank W. Nash and W. Quinlan for machining our chamber and artificial dura mold and working with us through the design process. We also thank Y. Guo in Xiaoqin Wang's lab for helpful discussions about the artificial dura, especially with respect to the choice of silicone.

4 Cascading effects of perceptual learning through a deep neural network

4.1 Introduction

Despite being one of the most studied visual behaviors, the neural underpinnings of visual perceptual learning – learning to perceive small differences in visual stimuli through repeated practice – remain unclear. Though the specificity of perceptual gains to the orientation, spatial frequency, retinotopic position, or ocularity of the trained stimulus (Crist et al., 1997; Fahle, 2004; Fiorentini and Berardi, 1981; Karni and Sagi, 1991) led many to hypothesize that plasticity within primary visual cortex (V1) formed the basis of perceptual learning (Gilbert et al., 2001), the locus of learning-induced plasticity has since been debated (Watanabe and Sasaki, 2015). Electrophysiology reports of V1 plasticity have been mixed (Ghose et al., 2002; Schoups et al., 2001), while plasticity has been observed reliably in V4 (Raiguel et al., 2006; Yang and Maunsell, 2004). Yet, despite the fact that V4 exhibits more tuning plasticity than V1, the responses of V4 neurons never become as sensitive to the trained stimulus features as V1 neurons (Raiguel et al., 2006; Yang and Maunsell, 2004). Moreover, neither the plasticity observed in V4 nor the more limited plasticity observed in V1 can account for perceptual gains (Raiguel et al., 2006; Schoups et al., 2001).

Not only has the observed tuning plasticity in V1 and V4 appeared insufficient to account for perceptual learning gains, but moreover, the hierarchical nature of visual processing challenges the idea that perceptual learning can be confined to a single area at all. More precisely, plasticity could arise either from plasticity within or between neurons in an area, or it could arise from the refinement of feedforward inputs (Bejjanki et al., 2011; Yang and

Maunsell, 2004). Thus, it is nearly impossible to discern whether tuning plasticity in a given area is important in its own right, or merely a snapshot of a signal as it is progressively refined across the visual hierarchy before reaching a sensory-motor decision area (Felleman and Van Essen, 1991). In other words, if we posit that perceptual learning depends on activity of neurons in V1, or even in V4, then the only way to understand the function of plasticity in these areas is to understand how their inputs are amplified or refined downstream. For this, a hierarchical computational model of visual processing is needed.

In this respect, deep convolutional neural networks present a unique opportunity. Deep convolutional neural networks have been shown to exhibit functional organizational similarities to the human visual cortex after training on object classification (Cichy et al., 2016; Eickenberg et al., 2017; Güçlü and Gerven, 2015), as well as tuning similarities to neurons in V1 and V4 (Pospisil et al., 2018; Zeiler and Fergus, 2013). Moreover, a deep network based on AlexNet (Krizhevsky et al., 2012) that was trained on an orientation discrimination task has previously been shown to exhibit many of the reported findings in the visual perceptual learning field, both in terms of behavior and tuning plasticity (Wenliang and Seitz 2018). Thus, deep neural networks are an ideal class of computational models for rigorously examining the effects of visual perceptual learning across a hierarchy of visual processing stages.

Here, we leverage an AlexNet-based deep neural network trained on an orientation discrimination task (Wenliang and Seitz, 2018) to investigate the cascading effects of learning-induced plasticity. More precisely, we develop a framework that selectively isolates learning-induced weight changes within each image-processing layer of the network and tests the effects of this plasticity on the population tuning of artificial neurons downstream. We then use

this framework to analyze the influence of task difficulty and training history on perceptual learning in the network, since these two task manipulations are thought to affect the locus of learning-induced plasticity. We find that, contrary to the field's current understanding of perceptual learning, neither task difficulty nor training history affect the locus of plasticity within the deep neural network. However, through examining the distributed effects of learning-induced plasticity across these different training conditions, we see that task difficulty and training history do profoundly influence how informative low-level neurons are to the classification, and the impact of low-level plasticity on downstream tuning. In all, our work advances a new framework for understanding visual perceptual learning, which may inspire future experiments.

4.2 Methods

4.2.1 Model

A modified version of AlexNet (Krizhevsky et al., 2012) was used for this study. AlexNet can be broadly divided into eight feedforward layers, where the first five layers are convolutional layers and the last three layers are fully connected layers. Within a convolutional layer, each artificial neuron acts as a linear filter on its inputs. The weights and biases that construct each linear filter are shared across space: consequently, image transformations are spatially uniform. Following the filtering step, the activity of each artificial neuron is passed through a rectified linear activation function, which preserves positive activations but sets negative activations to zero. Additionally, in convolutional layers 1, 2, and 5, the layer output is

passed through a max-pooling step, which spatially compresses the output by taking the maximum activation over a small area.

We used the PyTorch (Paszke et al., 2019) implementation of AlexNet, which was pre-trained on object classification using ImageNet. PyTorch's implementation of AlexNet is a single tower model (Krizhevsky, 2014), with 64, 192, 384, 256, 256 unique neurons in convolutional layers 1 through 5, respectively. We followed previously established methods for training AlexNet on an orientation discrimination task (Wenliang and Seitz, 2018). In brief, the three fully connected layers of AlexNet were discarded. A new sixth layer was created, which was fully connected to convolutional layer 5. This layer produced a scalar representation of the fifth convolutional layer. The network accepted pairs of images as inputs, where the first image in the pair was treated as a reference and the second image in the pair was treated as a test. A scalar representation of each image was obtained by passing each image through the network. Finally, the difference (Δ) between the representation of the reference (h_r) and the representation of the test (h_t) was passed through the following logistic function (Equation 1):

$$p = \frac{\exp(\Delta h)}{\exp(\Delta h) + 1} \quad (1)$$

This function determined the network's confidence that the test was rotated clockwise relative to the reference.

4.2.2 Stimuli

All stimuli were 8-bit 227x227 pixel Gabors, masked with a Gaussian window with a standard deviation of 50 pixels, and centered on a gray background. The wavelength of the Gabors was 10 pixels, which was chosen to optimize the drive to neurons in convolutional

layers 1 and 2. In particular, one cycle of the sinusoid could be fully contained within the spatial receptive field of a convolutional layer 1 neuron. All reference stimuli were orientated at 0°. All test stimuli were rotated clockwise or counterclockwise relative to the reference by some offset (see *Task design* below). On each trial, the contrast of the stimulus varied randomly, assuming values of 20%, 30%, 40%, or 50%. In addition, isotropic Gaussian noise was added to each stimulus, the standard deviation of which randomly varied from trial to trial and assumed values of 5, 10, or 15. Both the variable contrast and addition of random noise were modeled after Wenliang and Seitz 2018, and are implemented to compensate for the absence of sensory noise generated by the network itself, as well as the short stimulus presentation period for human subjects. Noise was generated independently for each stimulus presentation. The results are collapsed across contrast and noise.

4.2.2.1 *Training Procedure*

The network was initialized such that the weights to the convolutional layers were inherited from PyTorch's AlexNet, pre-trained on ImageNet, and the weights to layer 6 were zero-initialized as has been done previously (Wenliang and Seitz, 2018). We refer to this network as the 'novice' network. On each trial, pairs of Gabor stimuli (a reference and test) were fed into the network, and the network output a classification probability that the test was rotated more clockwise relative to the stimulus. This probability was compared to the true label (1 for clockwise, 0 for counterclockwise), and the discrepancy between the network's output and true label was used to train the weights of the network. More precisely, on each epoch, a batch of 50 pairs of reference and test stimuli were divided into three mini-batches. Each mini-batch was used to perform gradient descent: the cross-entropy loss l was computed as a

function of the network's classification of the mini-batch I_t, the correct labels $L_t$and the network's parameters θ_t. The negative gradient over θ_t of l was used to update the network parameters on the following mini-batch (Equations 2 & 3), and the appropriate adjustments to the weights were made through backpropagation. Moreover, the rate at which the network updated its parameters was further mediated by the learning rate, α = 0.0001, and the momentum μ = 0.9 (Wenliang and Seitz, 2018).

$$\theta_{t+1} = \theta_t + v_{t+1} \quad (2)$$

$$v_{t+1} = \mu v_t - \alpha \nabla_{\theta_t} l(\theta_t, I_t, L_t) \quad (3)$$

Epoch loss was computed as the average cross-entropy loss across the three mini-batches.

In addition, two steps were taken to prevent overfitting. First, the learning rate (α) was decremented by 50% every 200 epochs. Second, if the task difficulty was set to easy (see *Task design* below), early-stopping was implemented in the following way: For a given training epoch, if the epoch loss was lower than the previous epoch, the model parameters were saved as the best model weights. If the epoch loss did not decrease for 20 consecutive epochs, then training stopped, and the final trained model used for analysis was loaded with the best model weights, i.e., the weights that led to the lowest loss.

4.2.3 Task design

The novice network was trained on an easy discrimination task, a difficult discrimination task, and sequentially on an easy then difficult discrimination task. Each is described below.

Easy Task

In the easy task, the novice network was trained on a 20° orientation discrimination task, where the test stimuli were rotated by 20° relative to the reference stimulus oriented at 0°. Counterclockwise and clockwise stimuli were shuffled and presented pseudorandomly on each trial. The network that trained exclusively on the 20° discrimination is referred to as the 'Easy_net' in the text.

Hard Task

In the hard task, the novice network was trained on a 1° orientation discrimination task, where the test stimuli were rotated by 1° relative to the reference stimulus oriented at 0°. Counterclockwise and clockwise stimuli were shuffled and presented pseudorandomly on each trial. The network that trained exclusively on the 1° discrimination is referred to as the 'Hard_net' in the text.

Sequential Task

In the sequential task, a copy of the Easy_net received additional training on the 1° discrimination task. This network is referred to as the 'Easy-Hard_net' in the text.

4.2.4 Performance testing

During performance testing, gradient descent was disabled - in other words, learning was prevented from occurring following testing. The network was tested on 50 pairs of stimuli that were generated at the time of testing and thus were distinct from the set of training stimuli. The network was evaluated at 18 logarithmically spaced intervals from 0 to 500 epochs during training. All evaluations were made at the end of the training epoch.

The network's behavioral performance was quantified as the network's mean classification confidence (see equation 1) across all validation classifications within an epoch. The network's mean epoch accuracy was also measured. We evaluated mean epoch accuracy to make sure that classification confidence appropriately reflected the network's performance. However, we used classification confidence as our behavioral output because it is a more robust and sensitive measure than classification accuracy.

4.2.5 Analysis

Weight change

Weight change following training was evaluated both at the layer-level and at the level of individual units. To calculate the weight change of a given layer, the sum of individual weight changes (δw_i) was divided by the sum of the weights (w_i) in the layer before learning the task (Equation 4) (Wenliang and Seitz, 2018).

$$\frac{\Sigma_i^N |\delta w_i|}{\Sigma_i^N |w_i|} \tag{4}$$

The weight change of an individual neuron was computed using the same equation, but restricted to the weights within a given filter (Wenliang and Seitz, 2018). For layer-wise weight change, *N* is the total number of connections to its lower layer. For the weight change of an individual neuron, *N* is the size of the filter.

Tuning curves

The activation strength of each neuron with spatial receptive fields at the center of the image was measured for 100 Gabors, with orientations evenly spaced from 0 to 180°. The

stimuli used for measuring orientation tuning functions were presented at 100% contrast and with a noise standard deviation of 15. Each stimulus was presented to the network for 50 repetitions, with noise generated independently for each presentation, and each neuron's tuning function was taken as the mean activation across these 50 stimuli. We specifically computed tuning functions as a mean across repetitions of noisy stimuli to follow the approach used by Wenliang and Seitz 2018. This approach has the advantage of measuring the aspects of each neuron's tuning that are relatively robust to the noise encountered in the training stimuli. Neurons that did not exhibit a response to any of the test orientations after training on the perceptual learning task were excluded from further analysis.

In addition, the following summary metrics were computed on each neuron's tuning curve:

(1) Tuning curve correlation: the Pearson *r* correlation between the neuron's tuning curve before and after perceptual learning.

(2) Orientation preference: the vector sum of the neuron's response to all orientations.

(3) Shift in orientation preference: the angular distance between the neuron's orientation preference before and after training on the orientation discrimination task.

(4) Slope: the neuron's change in response at a given orientation. Slope was quantified as percent change per degree (Schoups et al., 2001; Wenliang and Seitz, 2018). Accordingly, the neuron's tuning curve was first normalized to its peak response before slopes were computed.

(5) Response magnitude: the strength of the neuron's response at the trained reference orientation

Weighted evidence

To estimate the contribution of a neuron to the classification, the parameters (weights and biases) of that neuron were marginalized out (Equation 5), and the resulting impact on the classification output was evaluated (Robnik-Sikonja and Kononenko, 2008; Scholte et al., 2018; Zintgraf et al., 2017) (see Scholte et al. 2018 Appendix A for a full derivation).

$$p(y|x, \Theta \setminus \theta) = \sum_{\theta} p(y|x, \Theta)\, p(\theta) \quad (5)$$

Here, $p(y|x, \Theta)$ is the probability of a stimulus x belonging to a class y in a network with parameters Θ, and $p(y|x, \Theta \setminus \theta)$ is the probability of x belonging to class y when the parameters of a particular neuron $\theta \in \Theta$ are unknown. For a given neuron in the network, we assumed that θ was normally distributed with uniform variance and mean equal to the observed weight and bias of θ in the network. $p(\theta)$ is the prior probability on θ, and is approximated by sampling θ 100 times. The impact on classification of marginalizing out the parameters of each unique neuron was quantified in weighted evidence (Robnik-Sikonja and Kononenko, 2008), and measured in bits. To reduce the possibility of noise contamination, we restricted our analysis only to neurons with non-zero responses to the center of the trained stimuli.

Influence of layer-wise weight change

At each test epoch during training as well as after training completed, the parameters of the network were saved in a state dictionary. Typically, to load a trained model, an instance of the novice network was created, and the full state dictionary of the trained model was loaded

into the novice network, overriding the parameters with which it was initialized. However, the parameters stored in the state dictionary could also be loaded into the novice network individually, or layer by layer. Thus, to investigate the impact of weight change within a single layer, an instance of the novice network was instantiated, and the weights and biases of a particular convolutional layer were replaced with the weights and biases of the same convolutional layer in the trained network of interest. To investigate the impact of excluding plasticity in a single convolutional layer of the network, the weights and biases of all convolutional layers of the trained network of interest except one were loaded into the novice network. To quantify the impact of these manipulations on the discriminability of conv5, we computed the ratio of the slope at the trained reference in the novice network where perceptual learning-induced plasticity had selectively been injected to the slope at the trained reference in the network that had undergone perceptual learning.

Statistics

Hierarchical trends were measured with Spearman's rank correlation. To test for significance, a t-statistic was computed using the equation $t = r\sqrt{(n-2)/(1-r^2)}$, where *r* is Spearman's rank correlation coefficient and *n* is the number of samples. This t-statistic was compared to a Student's t-test look up table with *n*-2 degrees of freedom (WILLIAM H. PRESS et al., 1992). Differences between distributions were tested for significance using a Mann-Whitney *U* test. Where *p* = 0, the magnitude of *p* exceeded machine precision and is therefore approximately 0.

4.3 Results

4.3.1 Perceptual learning-induced plasticity in a deep neural network.

Following previously established methods (Wenliang and Seitz, 2018), we constructed an AlexNet-based DCNN to study visual perceptual learning. This network included the first five convolutional layers of AlexNet, with weights and biases inherited from training on object recognition using ImageNet. We refer to this network as the 'novice' network, since it has developed basic tuning properties from training on object recognition but has not yet trained on a visual perceptual learning task.

We trained the novice network on a high precision, 1° orientation discrimination task, in which the network classified a Gabor test stimulus as rotated clockwise or counterclockwise relative to a Gabor reference stimulus oriented at 0° (Figure 4.1A). Because high precision tasks have been theorized to induce plasticity at early stages of visual processing (Ahissar and Hochstein, 2004; Sagi, 2011), investigating this task presented the opportunity to explore the ramifications of low-level plasticity on higher levels of the network. We refer to the network that has learned the 1° discrimination task as the 'Hard_net'.

Figure 4.1A shows that the Hard_net successfully learns the task. The dashed line shows the network's classification accuracy across epochs, and the solid line shows the network's confidence in its classification. More precisely, the network's accuracy reflects whether the network correctly classified a test stimulus as clockwise or counterclockwise relative to the reference, while the network's confidence is the network's estimate of the probability that the classification was correct. We used classification confidence as a metric for the network's performance as it as more reliable metric for how much the network has learned.

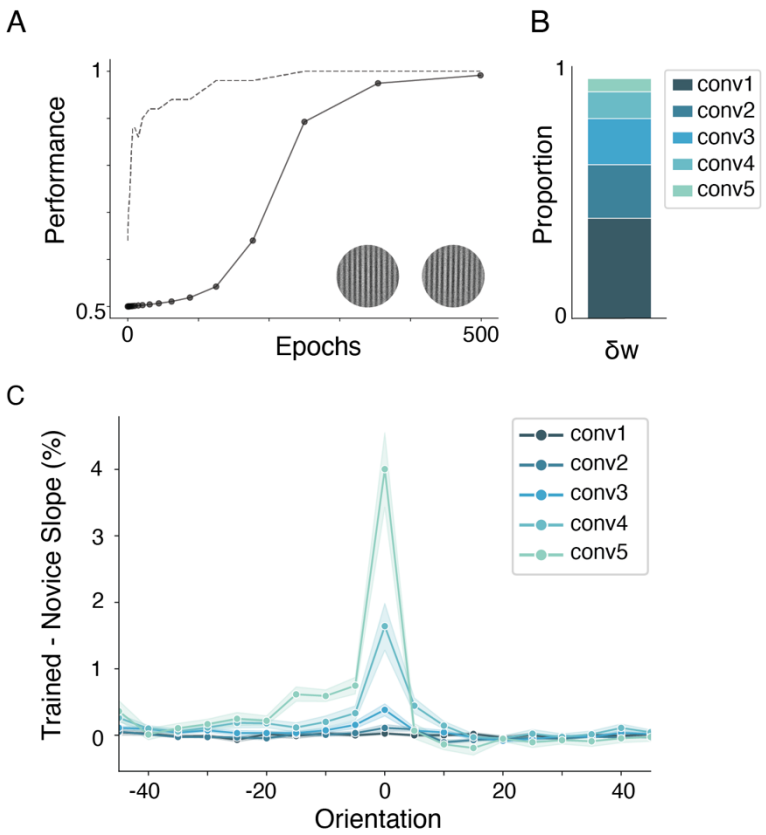

Figure 4.1 Learning-induced plasticity in the Hard_net.

(A) *Performance on the difficult discrimination task across training. Dashed line indicates classification accuracy, and solid line indicates classification confidence. Example reference stimulus (0°) and test stimulus (1°). Classification confidence was tested at logarithmically spaced intervals throughout training.*
(B) *Layer-wise proportion of weight change relative to the novice network.*
(C) *Mean change in slope (percent per degree) as a function of orientation by layer.*

Before investigating the cascading effects of learning-induced plasticity through the network, we first made a baseline characterization of the degree of plasticity exhibited in each convolutional layer. Specifically, we measured plasticity as both changes in the weighted connections between neurons, as well as changes in the tuning properties of neurons. This characterization of learning-induced plasticity establishes an important benchmark for comparisons with neurophysiology studies, which have examined the effects of visual

perceptual learning in V1 (Ghose et al., 2002; Schoups et al., 2001), V4 (Adab and Vogels, 2011; Raiguel et al., 2006; Yang and Maunsell, 2004), and PIT (Adab et al., 2014).

We first measured the amount of weight change within each convolutional layer. More precisely, each neuron in each convolutional layer derives its response though a weighted sum of the activity of all of the neurons in the convolutional layer below. Thus, measuring the amount that these weights change with learning is one metric for evaluating how much plasticity occurred within a given convolutional layer (Wenliang and Seitz, 2018). To compare the relative proportion of weight change across the network, we normalized the weight change within each layer by the sum of the weight change in all layers. Similar to previous reports (Wenliang and Seitz, 2018), we found the extent of weight change weight change was highest at the early layers of the network and diminished hierarchically. (Figure 4.1B, Spearman's ρ = -1 + 1.11e-16, p = 1.4e-24).

Next, we compared the tuning curves of neurons before and after learning using three metrics: change in orientation preference, change in slope at the trained orientation, and the overall correlation between the tuning curves of neurons in the Hard_net and the novice network. More precisely, we computed the mean change in orientation preference to investigate how much perceptual learning affected the distribution of orientation preferences in the network (Table 4.1, Column 1). Tuning preferences have been shown to shift in primary auditory and somatosensory cortices following perceptual learning (Gilbert et al., 2001), but have been shown to be stable in V1 (Ghose et al., 2002; Schoups et al., 2001). We computed the mean change in slope of the tuning curves of neurons at the trained orientation to measure how much each neuron's sensitivity to the trained orientation has changed with learning (Table

4.1, Column 2). This sensitivity has been shown to increase with perceptual learning in V1 and in V4 (Raiguel et al., 2006; Schoups et al., 2001). Finally, we measured the mean correlation between the tuning curves in the novice network and the tuning curves of neurons in the Hard_net, which had undergone perceptual learning. We use this metric as tool to estimate overall tuning plasticity while being agnostic to the form that that plasticity should take.

In contrast to the distribution of weight changes, the extent of tuning plasticity increased hierarchically across all metrics (Table 4.1). Specifically, the mean shifts in each neuron's orientation preference, the increase in sensitivity at the trained orientation, and the change in the overall shape of the tuning curves of neurons at each layer increased hierarchically. To evaluate whether neurons developed tuning curves that were biased to enhance discrimination at the trained orientation in particular, we computed the average change in tuning curve slope at 36 orientations spanning 0 to 180°. We found that changes in slope were largest at the trained orientation, and increased nonlinearly in magnitude hierarchically (Figure 4.1C). The finding that that tuning plasticity increases hierarchically in the deep neural network is consistent with electrophysiology studies in V1, V4, and PIT (Adab and Vogels, 2011; Adab et al., 2014; Ghose et al., 2002; Raiguel et al., 2006; Schoups et al., 2001; Yang and Maunsell, 2004). Strikingly, the population tuning curve of conv5 developed a steep slope at the trained reference, and the development of this population tuning bias evolved with behavioral improvements (Figure 4.2). The steep slope around the trained reference orientation suggests that readout relies on the difference in the overall response between the two test stimuli, rather than differentially weighting of two distinct populations of neurons that have tuning preferences on either side of the trained reference.

Layer	Mean change in orientation preference (°)	Mean change in slope at the trained orientation (%)	Mean tuning curve correlation
Conv1	1.5	0.026	0.89
Conv2	2.14	0.11	0.94
Conv3	7.69	0.38	0.87
Conv4	22.31	1.64	0.61
Conv5	33.81	4.0	0.34
Rank correlation (Spearman's ρ)	1 - 1.11e-16, p = 1.4 e-24	1 - 1.11e-16, p = 1.4 e-24	-0.9, p = 0.037

Table 4.1 Summary of learning-induced tuning curve changes in the Hard_net across the hierarchy.

Column 1: Mean change in the orientation preference of neurons after perceptual learning. Column 2: Mean difference in slope at the trained orientation, measured in percent change per degree. Column 3: Mean correlation between the tuning curves of neurons in each convolutional layer before and after perceptual learning.

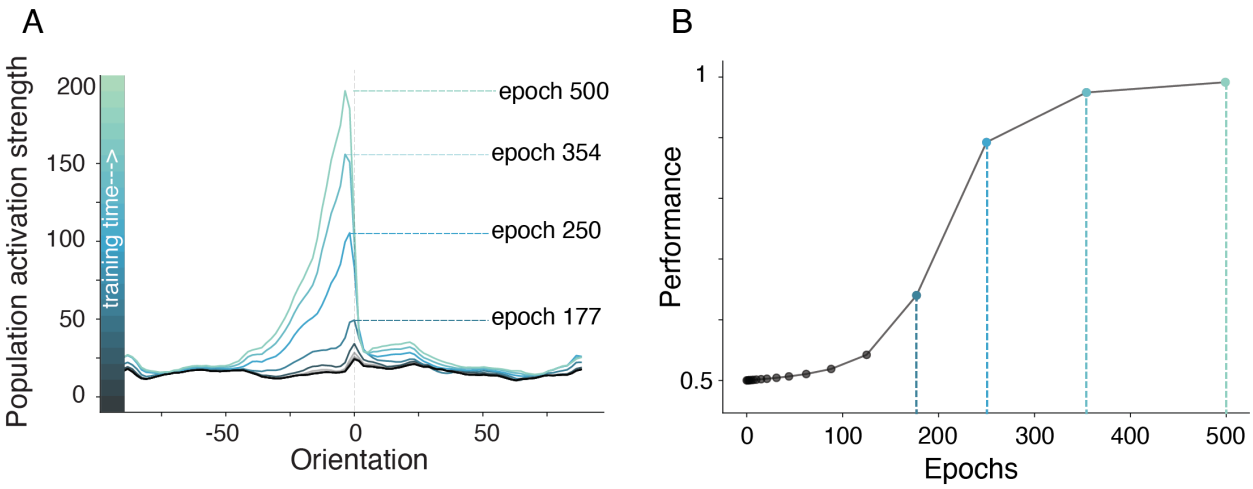

Figure 4.2 Evolution of conv5 population tuning across learning in the Hard_net

***(A)** Evolution of the population tuning in conv5 across training. The population tuning is the sum of the tuning curves of all neurons in conv5. Population tuning was evaluated at logarithmically spaced test intervals during training. Dashed line indicates the trained reference orientation.*
***(B)** For reference, the network's performance on the discrimination task is replotted, where the dashed lines correspond to the training epochs highlighted in (A). Performance is quantified as classification confidence.*

4.3.2 Cascading effects of learning-induced weight change

Thus far, we have shown that learning-induced tuning plasticity in the DNN increases hierarchically, following the same trends as learning-induced tuning plasticity in the primate. At the same time, we showed that the distribution of weight plasticity is highest at low levels of the network and decreases hierarchically, suggesting that the degree of tuning plasticity exhibited by a particular layer might not reflect the degree of plasticity within the layer itself. We next sought to understand how weight plasticity within each layer of the network affected the tuning properties of neurons downstream. In particular, we examined the impact of weight change within each layer of the network on the population tuning in conv5, because its activity provides direct input to the classifier.

For this analysis, we first investigated how weight changes limited to a single convolutional layer affected the population tuning of conv5. Effectively, this analysis examines how the population tuning of conv5 would change if the plasticity within a particular convolutional layer was the only plasticity that occurred. This analysis provides insight into how weight changes within a particular layer influence conv5 within the constraints of the weighted connections that already existed within the novice network.

To understand the impact of plasticity within a single layer of the network, we selectively loaded the trained weights of single layer of the Hard_net into the novice network, and measured the resultant population tuning in conv5 (Figure 4.3). For comparison, we plotted the population tuning in conv5 of the novice network on the same axis. Limiting weight change to conv3 or conv4 alone substantially influenced the shape of the population tuning curve in conv5 (Figure 4.3C-D). In contrast, limiting weight change to conv1 or conv2 did little to

influence the population tuning curve in conv5. The weight change within conv5 itself produced only negligible effects on the population tuning in that layer (Figure 4.3A-B,E). Notably, however, no single layer's plasticity on its own could account for more than 3% of the discriminability in Hard_net conv5 that arose from the combined plasticity of all layers, as measured by the slope at the trained reference (Table 4.2).

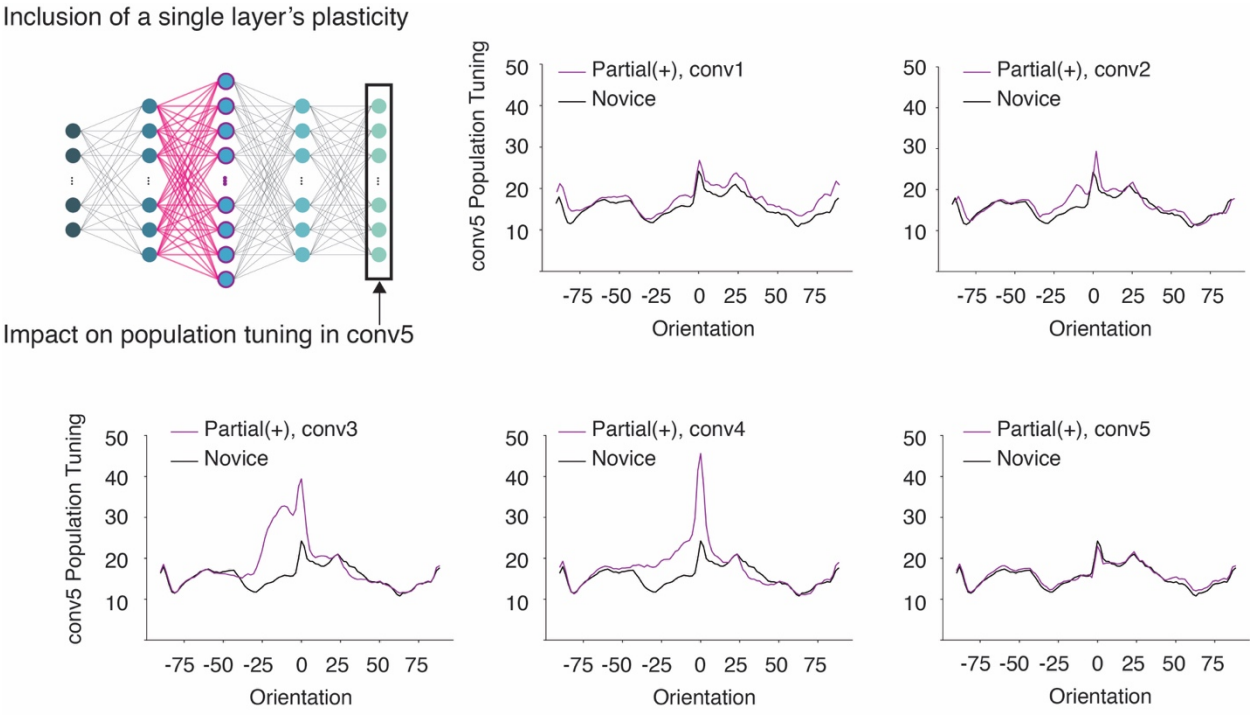

Figure 4.3 Downstream effects of single layer weight change on conv5 of the Hard_net.

Population tuning curves of conv5 for the novice network (black line) and for conv5 of a modified novice network where the weights of a single convolutional layer have been replaced with the weights from the Hard_net that developed through perceptual learning (Partial(+),purple line). The layer in the legend refers to the layer of the novice network where the weights were replaced with weights from the Hard_net.

Layer	% slope at the trained orientation in conv5 with a single layer's weight change	% slope at the trained orientation in conv5 without a single layer's weight change
Conv1	1%	68%
Conv2	0.2%	53%
Conv3	3%	22%
Conv4	2%	30%
Conv5	2%	83%

Table 4.2 Effects of plasticity within each layer of the Hard_net on the discriminability of conv5.

Left column: Percent of the slope at the trained orientation in conv5 of the Hard_net that can be achieved when the learning-induced weight changes from a single convolutional layer is selectively loaded into the novice network. Right column: Percent of the slope at the trained orientation in conv5 of the Hard_net that can be achieved when weights of a single convolutional layer are replaced with the weights of the novice network.

Second, we investigated how the population tuning of conv5 was affected by excluding weight change from a single convolutional layer of the network. This analysis sheds light into how the plasticity within a particular convolutional layer works in concert with plasticity within other layers in the network. More precisely, examining the effects of excluding plasticity within low-levels of the network effectively asks how low-level plasticity is amplified or refined by plasticity downstream, while examining the effects of excluding plasticity within intermediate and late layers of the network asks how low-level plasticity is gated by those layers. We achieved this by selectively replacing the weights in a single layer of the Hard_net with weights from the novice network and re-measuring the population tuning curve of conv5 (Figure 4.4).

For comparison, we plotted the population tuning of conv5 from the unperturbed Hard_net on the same axes.

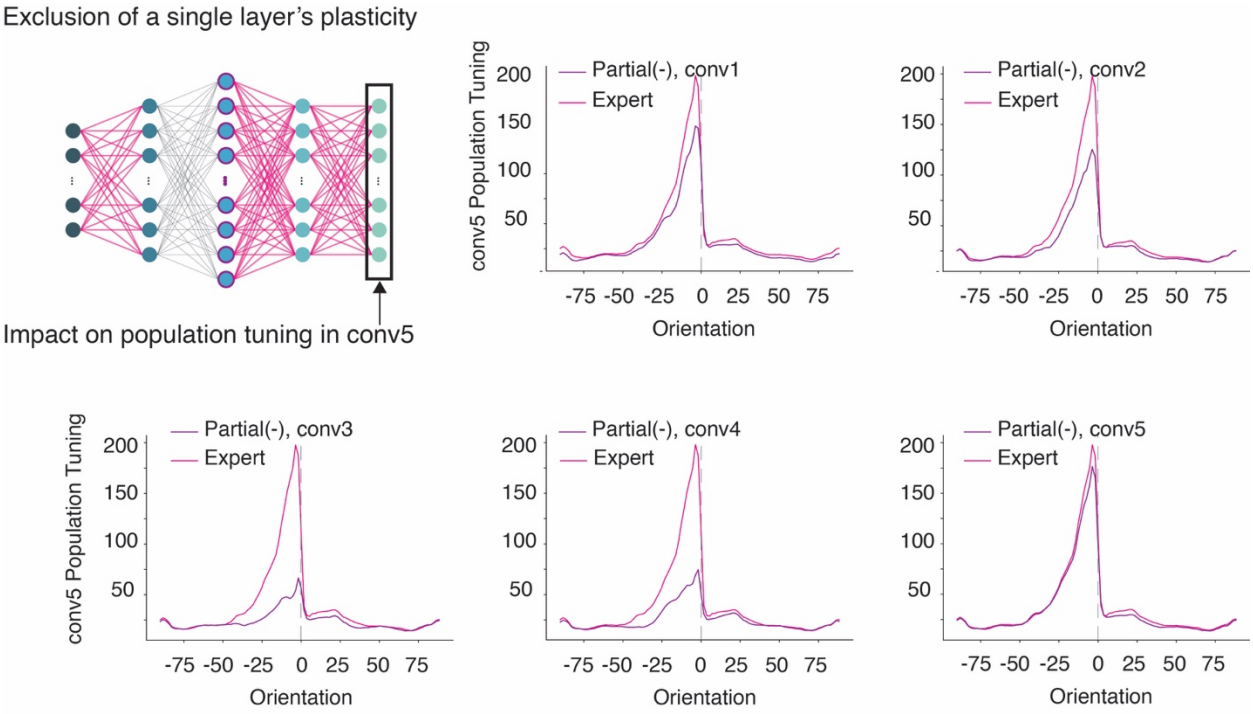

Figure 4.4 Consequences of excluding plasticity within a single convolutional layer on the population tuning in conv5

Population tuning curves of conv5 for the Hard_net (pink line), and for conv5 of the Hard_net where the weights of a single layer are replaced with the weights of the novice network (Partial(-), purple line). The layer in the legend refers to the layer of the Hard_net where weights were replaced with weights from the novice network.

Although the effects of weight change in conv1 and conv2 exerted relatively little influence on population tuning in conv5 on their own, the effects of weight change in these layers were substantially amplified by plasticity at subsequent processing stages. Selectively excluding learning-induced weight changes in conv1 and conv2 led to a 32% and 47% reduction in discriminability at the trained reference orientation, respectively (Table 4.2). Thus, although

weight plasticity limited to conv1 or conv2 produces little impact on the novice network, their plasticity is substantially amplified by the plasticity of neurons in downstream layers of the network. The most dramatic effects on the population tuning of conv5 were observed with novice weights in conv3 and conv4 however (Figure 4.4C-D), which each led to a 78% and 70% reduction in discriminability, respectively. This suggests that plasticity within conv3 and conv4 gate the efficacy of plasticity upstream.

The finding that the population tuning of conv5 depended strongly on the plasticity of conv3 appears particularly noteworthy: Plasticity within conv3 reflects changes in how conv3 neurons weigh the input of conv2 neurons. The representation of visual features in conv2 most closely resembles primate V1 (Güçlü and Gerven, 2015; Khaligh-Razavi and Kriegeskorte, 2014). Furthermore, learning-induced tuning plasticity in conv2 has been shown to correspond well with electrophysiology studies of visual perceptual learning in macaque V1 (Wenliang and Seitz, 2018). Because conv5 is read out by the classifier, our results suggest that, in the deep network, selectively reweighting neurons with V1-like activity is especially important for behavioral gains.

Still, the most important conclusion from this analysis is that the plasticity of any particular layer can only be understood in the context of plasticity within the rest of the network. The tuning plasticity exhibited in conv5 depended minimally on weight plasticity within the layer itself, but rather reflected plasticity across all layers. Moreover, weight change limited to any single layer of the hierarchy had much less influence on the population tuning of conv5 than the absence of weight plasticity within a single layer, revealing the coordinated amplification and refinement of plasticity through the hierarchy.

4.3.3 The influence of task difficulty

The results that we have presented thus far have challenged the notion that perceptual learning has a singular origin. We therefore investigated whether task manipulations that have been hypothesized to change the locus of learning-induced plasticity actually affect the layer-wise distribution of plasticity in the deep network, or whether they instead more subtly affect the way that neurons are reweighted across all layers of the hierarchy. Specifically, we compared the effects of learning an easy discrimination task versus learning a difficult discrimination task. Because easy, low precision tasks exhibit more transfer of performance gains than difficult tasks – in other words, because learning an easy perceptual task generalizes more readily across stimulus features such as orientation and retinotopic position - mastering an easy task has been thought to originate from plasticity at a mid or late visual stage. By the same token, mastering a high precision task has been thought to require low-level plasticity where the receptive fields of neurons are more selective (Ahissar and Hochstein, 1997, 2004). We therefore trained the novice network on a 20° orientation discrimination task with a reference of 0° and compared it to the Hard_net. Herein, we refer to the network that has learned the 20° discrimination task as the 'Easy_net'.

We first established that, like human subjects, the network learned the easy task more rapidly than the difficult task and exhibited more transfer of performance gains across reference orientations. Indeed, consistent with psychophysical studies (Ahissar and Hochstein, 1997; Liu and Weinshall, 2000; Rubin et al., 1997) as well as previous reports of perceptual learning in a deep neural network (Wenliang and Seitz, 2018), the novice network learned the easy discrimination task much more rapidly than it learned the difficult discrimination task

(Figure 4.5A, Easy_net performance plateaus by epoch 88 while the Hard_net performance does not plateau until epoch 354). Importantly, the Easy_net exhibited more transfer than the Hard_net, again consistent with psychophysical reports. We quantified transfer as the classification confidence for a reference 45° away from the trained reference divided by the classification confidence for the trained reference. The Easy_net had a transfer index of 0.87, while the Hard_net had a transfer index of 0.51. Thus, behaviorally, the grounds for the hypothesis that learning an easy discrimination task should elicit less plasticity in the low levels of the hierarchy than learning a difficult discrimination task hold in the deep network.

We therefore measured the distribution of plasticity across layers in the Easy_net using the same analysis employed above for the Hard_net. In contrast to the idea that low task precision should lead to less plasticity at low levels of the network, the relative layer-wise weight change in the Easy_net was greatest at the lowest layers, and decreased hierarchically, just like the Hard_net (Figure 4.5B, Spearman's ρ = -1 + 1.11e-16, p = 1.4e-24). Thus, at least in a deep network, the differences in the generalizability of learning cannot be explained by differences in the layer-wise distribution of weight change throughout the hierarchy.

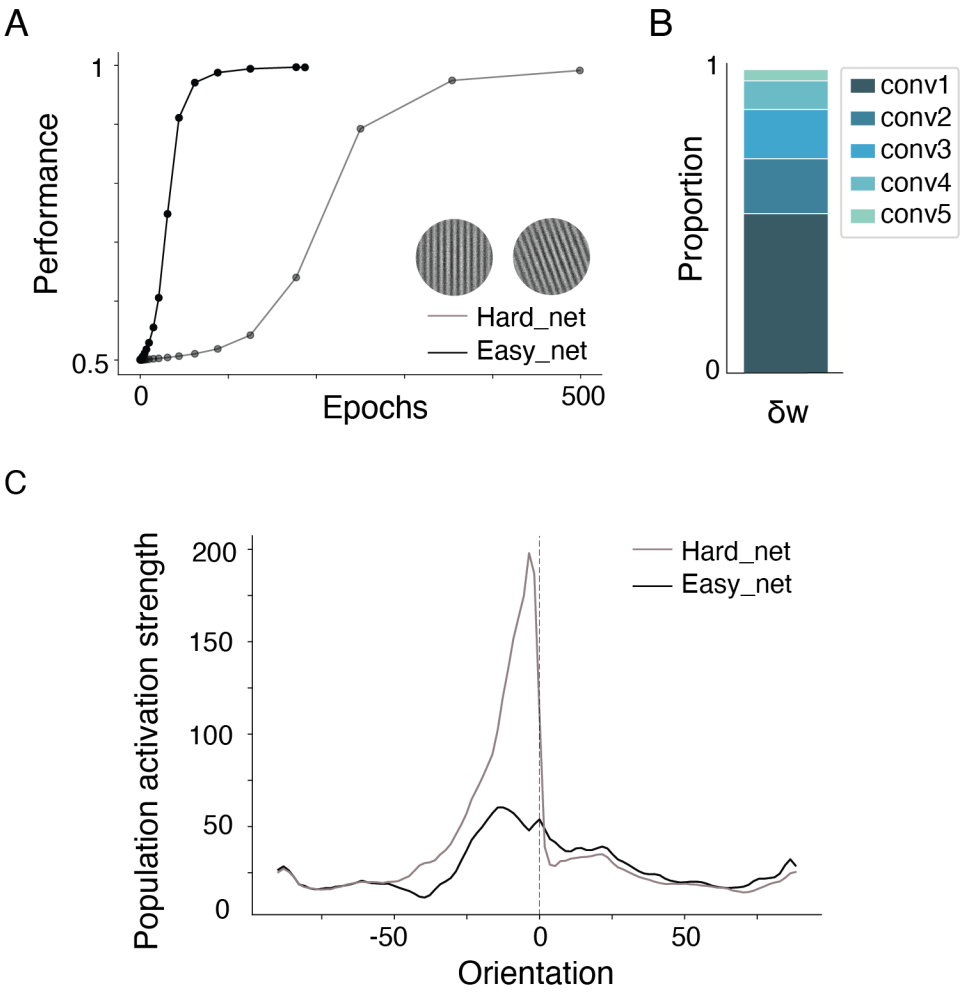

Figure 4.5 Learning-induced plasticity in the Easy_net.

(A) *Performance of the Easy_net versus the Hard_net across training. The Easy_net learned the 20° discrimination task faster than the Hard_net learned the 1° discrimination task. Bottom right: example stimuli for the easy discrimination task.*
(B) *Layer-wise proportion of weight change in the Easy_net relative to the novice network.*
(C) *Summed population response of neurons in convolutional layer 5 of the Easy_net compared to the Hard_net.*

We next investigated learning-induced tuning plasticity within the Easy_net and compared it with the Hard_net. As before, we evaluated learning-induced tuning plasticity by measuring the mean shift in orientation preference, mean change in slope at the trained orientation, and mean tuning curve correlation between neurons in each layer of the network

before and after training. Like the Hard_net, tuning plasticity increased hierarchically in the Easy_net (Table 4.3). However, the extent of tuning plasticity in the Easy_net was less than the extent of tuning plasticity in the Hard_net. Most notably, the tuning curves of neurons in conv5 changed much more with learning in the Hard_net than the Easy_net, as evidenced by a greater change in slope at the trained orientation and a lower correlation between the tuning curves of neurons before and after training. Across the population, conv5 of the Hard_net exhibited a much greater degree of sensitivity to the trained stimulus than the Easy_net (Figure 4.5C). The shallower population tuning of conv5 in the Easy_net as compared to the Hard_net is consistent with the fact that the Easy_net exhibits more transfer of performance gains across orientations than the Hard_net.

Layer	**Mean change in orientation preference (°)**	**Mean change in slope at the trained orientation (%)**	**Mean tuning curve correlation**
Conv1	1.52	0.002	0.91
Conv2	1.82	0.016	0.94
Conv3	6.10	0.085	0.90
Conv4	15.82	0.14	0.76
Conv5	15.52	0.47	0.61
Rank correlation (Spearman's ρ)	0.9, p 0.037	1 – 1.11e-16, p = 1.4 e-24	-0.9, p = 0.037

Table 4.3 Summary of tuning curve changes across the hierarchy after training on the 20° discrimination task.

Column 1: Mean change in the orientation preference of neurons after perceptual learning. Column 2: Mean difference in slope at the trained orientation, measured in percent change per degree. Column 3: Mean correlation between the tuning curves of neurons in each convolutional layer before and after perceptual learning.

Thus far, we have shown that although the Easy_net and the Hard_net exhibit different levels of behavioral and neural sensitivity to the trained orientation, they are not readily distinguishable by a change in locus of plasticity, where one would expect the layers that exhibit the greatest plasticity to differ between the two networks. As an alternative hypothesis, we posited that the difference between the networks instead lay in how selectively neurons at each stage of the hierarchy were reweighted to enhance the network's performance. In other words, rather than supposing that learning an easy task leads decision areas – corresponding to the classifier in the deep network – to selectively weigh inputs from neurons with broad receptive fields residing in mid or late stages of the hierarchy, it might instead be the case that easy tasks lead decision units to gather information from a broader population of neurons across all layers of the hierarchy.

We therefore investigated how much evidence individual neurons provided for the classification in both the Easy_net and the Hard_net (see *Methods: Analysis: Weighted evidence*). Intuitively, this analysis replaces the inputs of each neuron with noise, and measures how much the behavioral performance of the network is degraded as a result. Neurons with weighted evidence greater than 1.6 contribute substantial evidence to the classification (Jeffreys, 1998). Therefore, if the Easy_net recruited from a broader population of neurons than the Hard_net to perform the classification, we would expect that the Easy_net would have more neurons with weighted evidence greater than 1.6. Indeed, this prediction holds in every layer except conv1, where the difference between the networks is negligible (Figure 4.6).

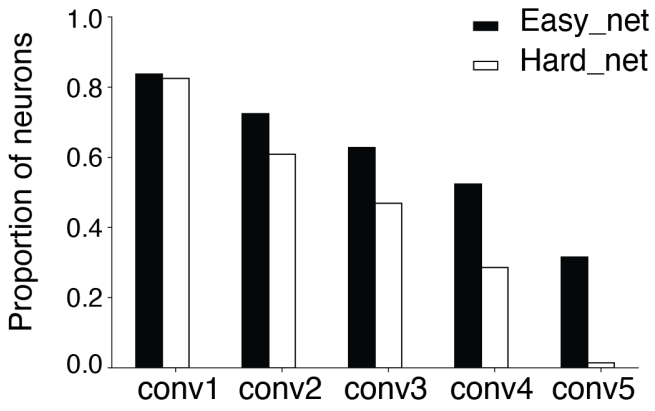

Figure 4.6 Proportion of neurons in the Easy_net and the Hard_net with weighted evidence greater than 1.6 bits.

Black bars: Easy_net. White bars: Hard_net.

Finally, we investigated whether signatures of task difficulty were apparent in the way that plasticity of individual layers affected the population tuning in conv5. Specifically, we investigated whether plasticity within individual layers of the Hard_net more selectively affected the population tuning in conv5 than plasticity within individual layers of the Easy_net. Since more neurons contributed meaningful evidence to the classification in the Easy_net than in the Hard_net, we predicted that the weight plasticity within individual layers of the Easy_net would similarly affect the population tuning of conv5 more broadly in the Easy_net as compared to the Hard_net.

Therefore, just like we did with the Hard_net, we selectively loaded weights from individual layers of the Easy_net into the novice network and measured the resultant population tuning in conv5. To more readily visualize the extent to which the responses to specific orientations were enhanced, we divided the resultant population tuning in conv5 by the population tuning curve of the novice network. This analysis estimated the multiplicative

gain at each orientation that was achieved through the plasticity of a single convolutional layer. We did the same for the Hard_net, and plot the multiplicative gain on the conv5 population response for both networks in Figure 4.7. We then quantified the breadth of the influence that each layer's plasticity had on conv5 by measuring the span of orientations *S_ori* for which conv5 exhibited more than a 10% increase in response (as reflected by a multiplicative gain greater than 1.1), and compared this breadth between the Easy_net and the Hard_net.

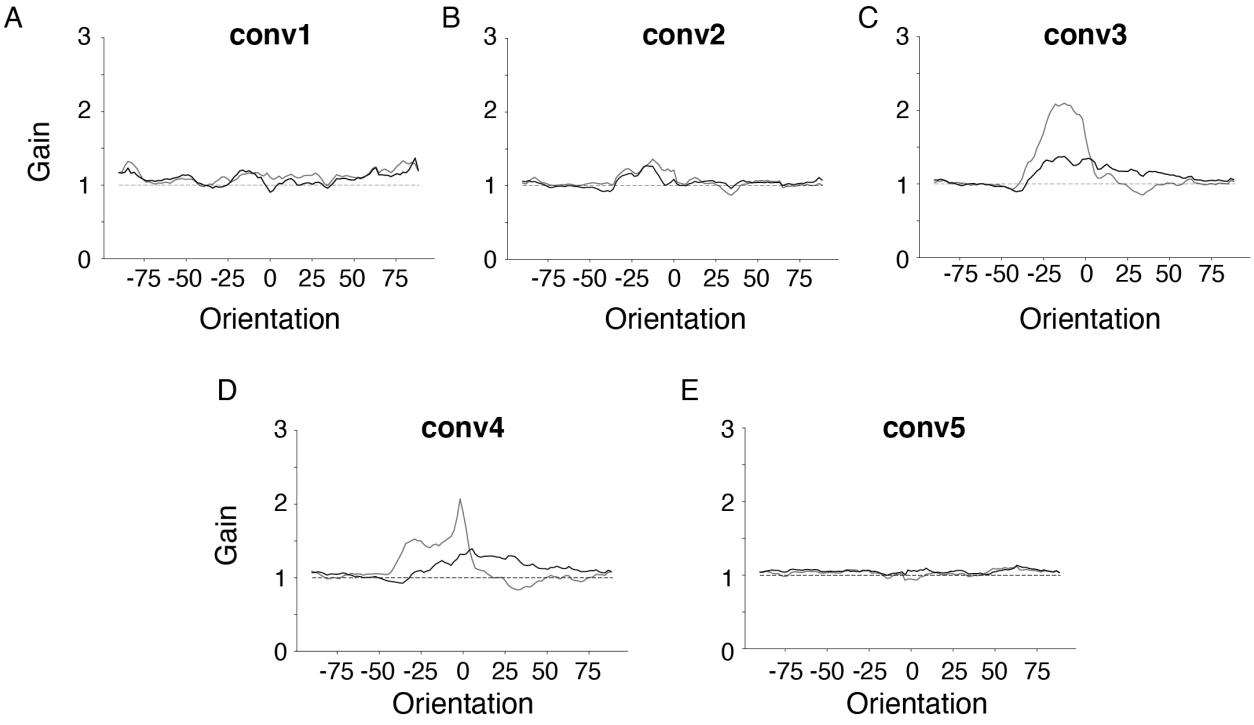

Figure 4.7 Multiplicative gain on the novice network induced by single layer plasticity.

Multiplicative gain across orientation space when weights from a layer of the Easy_net (black lines) or Hard_net (gray lines) are selectively loaded into the novice network.

The effects of weight plasticity in conv1, conv2, and conv5 were comparable between the two networks (Figure 4.7A-B,E). However, the effects of weight plasticity in conv3 and

conv4 were distinctly different between the two networks. Weight plasticity in conv3 and conv4 acted much more selectively in the Hard_net, where *S_ori* was 50.4° from conv3 plasticity and 52.2° from conv4 plasticity. By contrast, *S_ori* was 90.0° from conv3 plasticity and 93.6° from conv4 plasticity in the Easy_net. Thus, as predicted, we see that the distributed effects of plasticity in conv3 and conv4 acted more broadly on conv5 in the Easy_net than the Hard_net.

4.3.4 The distributed effects of training history

Finally, we explored how training on an easy task influenced subsequent learning of a difficult task. Psychophysical studies have shown that training on an easy task expedites learning of a more difficult task (Ahissar and Hochstein, 1997; Liu and Weinshall, 2000; Rubin et al., 1997), but besides these behavioral results, there is no corresponding data, nor a clear hypothesis, for how training on an easy task before training on a difficult task would manifest at the neural level. We therefore investigated learning-induced plasticity in a network that was first trained on the 20° orientation discrimination task, and then trained on the 1° orientation discrimination task. More precisely, we trained a copy of the Easy_net on the 1° discrimination task. Herein, we refer to the network that was trained on both the 20° discrimination and the 1° discrimination as the 'Easy-Hard_net'. We posited that the effects of training history might be subtle and distributed throughout the network in ways that have not hitherto been measurable in the brain but would be accessible in a deep network through the analytical framework we have developed thus far. More specifically, we wondered whether training on an easy task before training on a difficult task would affect the pattern of weight plasticity throughout the network, and consequently influence the cascade of evidence for the classification through the hierarchy.

First, we established that training on an easy task before training on a more difficult task enhanced learning in a deep network. Indeed, consistent with human psychophysical experiments, training on an easy 20° discrimination task clearly expedited learning of the 1° discrimination task (Figure 4.8A). We observed an accelerated learning trend towards peak classification confidence, as well as an initial classification confidence that was higher than the classification confidence of the Hard_net at epoch 0.

Figure 4.8 Performance and weighted evidence comparison between the Easy-Hard_net and the Hard_net *(Opposite page)*

(A) *Performance of the Easy_Net on the 20° discrimination, and of the Easy-Hard_Net and Hard_Net on the 1° discrimination. Training on the 20° discrimination before training on the 1° discrimination accelerated the rate at which the Easy-Hard_Net learned the difficult discrimination task.*
(B – F). *Cumulative distribution functions of weighted evidence by layer for the Easy-Hard_Net and the Hard_Net for layers conv1-conv5 respectively. Weighted evidence was measured in bits.*

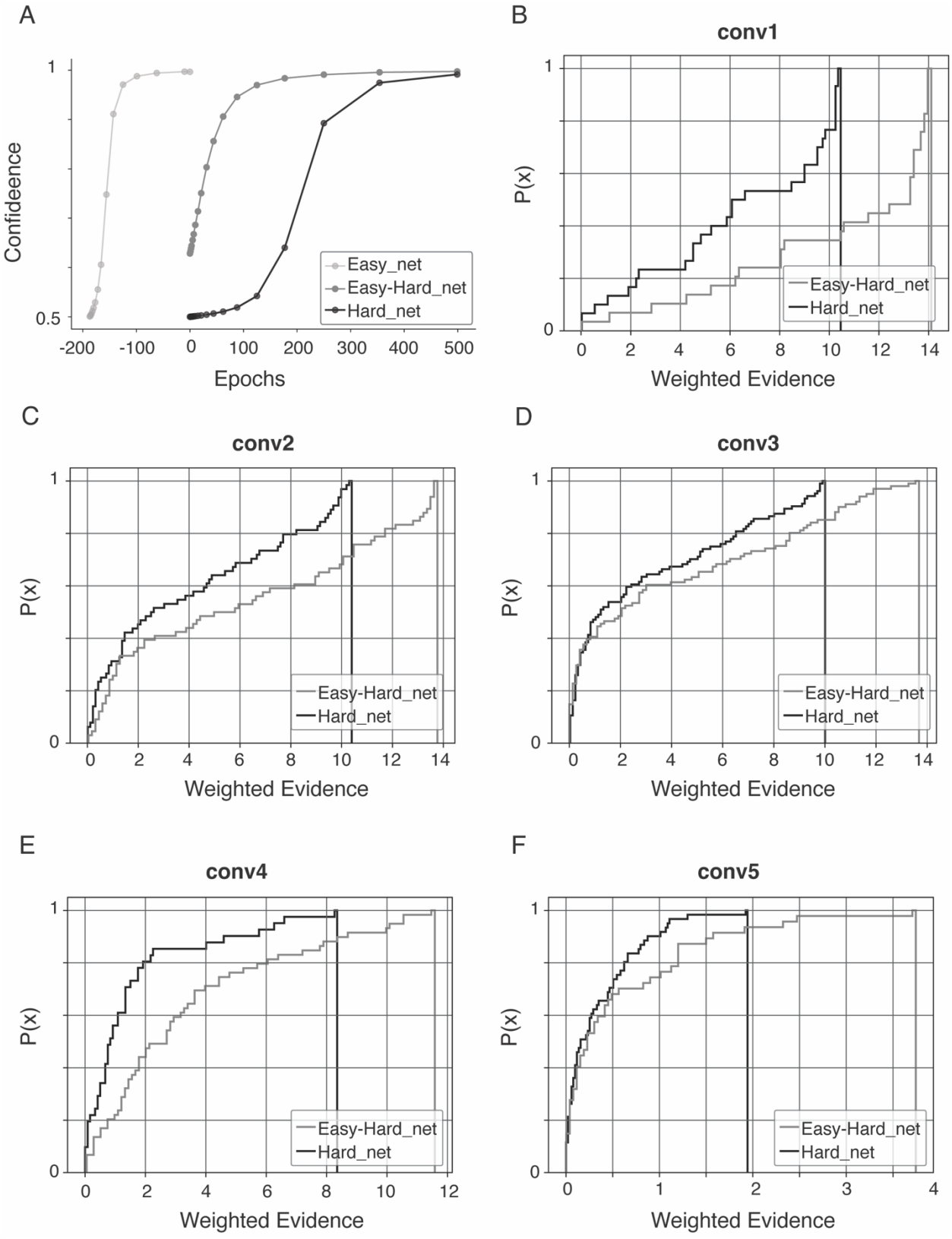
A
Confideence
Epochs
Easy_net
Easy-Hard_net
Hard_net
B
conv1
P(x)
Weighted Evidence
C
conv2
D
conv3
E
conv4
F
conv5

We next investigated whether training on the 20° discrimination before training on the 1° discrimination had impacted the sensory representation of the trained stimuli by comparing tuning properties of neurons in the Easy-Hard_net and the Hard_net. To characterize the tuning properties of neurons in the two networks, for each layer, we measured the slopes of neurons at the trained orientation, the responses of neurons to the trained reference, and the distribution of orientation preferences in each of the two networks. We chose these metrics because they have been used previously to investigate the impact of perceptual learning (Gilbert et al., 2001). We observed no significant differences between the tuning properties of neurons in Easy-Hard_net and the Hard_net in conv1-conv4 (Table 4.4, $p >> 0.01$, student's *t*-test). The only significant difference that we observed was in the distribution of orientation preferences that developed in conv5.

Layer	**Slope at the trained orientation**	**Response to the trained reference orientation**	**Distribution of orientation preference**
Conv1	$t = -0.06$ $p = 0.95$	$t = 0.018$ $p = 0.99$	$t = -0.41$ $p = 0.68$
Conv2	$t = 0.29$ $p = 0.77$	$t = -0.06$ $p = 0.95$	$t = 0.028$ $p = 0.98$
Conv3	$t = -0.039$ $p = 0.97$	$t = -0.73$ $p = 0.47$	$t = -1.48$ $p = 0.14$
Conv4	$t = -0.14$ $p = 0.89$	$t = -0.56$ $p = 0.57$	$t = 0.93$ $p = 0.35$
Conv5	$t = -0.40$ $p = 0.69$	$U = -0.58$ $p = 0.56$	$t = -4.37$ $p = 0.00022$

Table 4.4 Student's t-tests comparing the tuning properties of neurons in the Easy-Hard_net and the Hard_net by layer.

Though the orientation tuning of neurons in the two networks was comparable, it might still be the case that the way that way that sensory evidence was weighted downstream differed between the two networks. In order to investigate this, we first estimated how much information neurons in each of the networks contributed to the classification. Like we did in the previous section, we estimated the weight of evidence that neurons provided by estimating the impact of replacing the input of a particular neuron with noise (see *Methods: Analysis: Weighted evidence*). This time, we asked whether neurons were overall more informative in the Easy-Hard_net than the Hard_net by comparing the distributions of weighted evidence in each convolutional layer. We found that the distribution of weighted evidence in the Easy-Hard_Net was greater for all layers (Figure 4.8B-F), and significantly greater in convolutional layers 1, 2, and 4 (Table 4.5, $p < 0.01$, Mann-Whitney *U* test). Taken together, these analyses suggest that training a deep network on an easy task before training on a difficult task enhanced the readout of sensory evidence without requiring significant differences in tuning.

Layer	**U**	**p**
Conv1	543	0.0068
Conv2	1834	0.0072
Conv3	6059	0.16
Conv4	819	0.00035
Conv5	1843	0.23

Table 4.5 Mann-Whitney U test comparing the distributions of weighted evidence at each convolutional layer of the Easy-Hard_net and the Hard_net.

We next investigated whether training on an easy task before training on a difficult task affected the way that plasticity within each convolutional layer cascaded through the network to impact the population tuning of conv5. As before, we selectively loaded weights from individual convolutional layers of the Easy-Hard_net into the novice network to measure the efficacy of plasticity within each individual layer of the Easy-Hard_net, and we selectively replaced layers of trained weights in the Easy-Hard_net with weights from the novice network to investigate the effects of excluding plasticity within an individual layer. The resultant impact on the discriminability of conv5 are shown in Figure 4.9.

Figure 4.9 Distributed effects of layer-wise weight change on conv5 of the Easy-Hard_net. *(Opposite Page).*

(A-E) *Population tuning curves of conv5 for the novice network (black line) and for conv5 of a modified novice network where the weights of a single convolutional layer have been replaced with the weights that develop through perceptual learning in the Easy-Hard_net (Partial(-),purple line). Rows indicate the convolutional layer that has the trained weights.*
(F-I) *Population tuning curves of conv5 for the Easy-Hard_net (pink line), and for conv5 of the Easy-Hard_net where the weights of a single convolutional layer are replaced with the weights of the novice network (Partial(+),purple line). Rows indicate the convolutional layer that has the novice weights.*

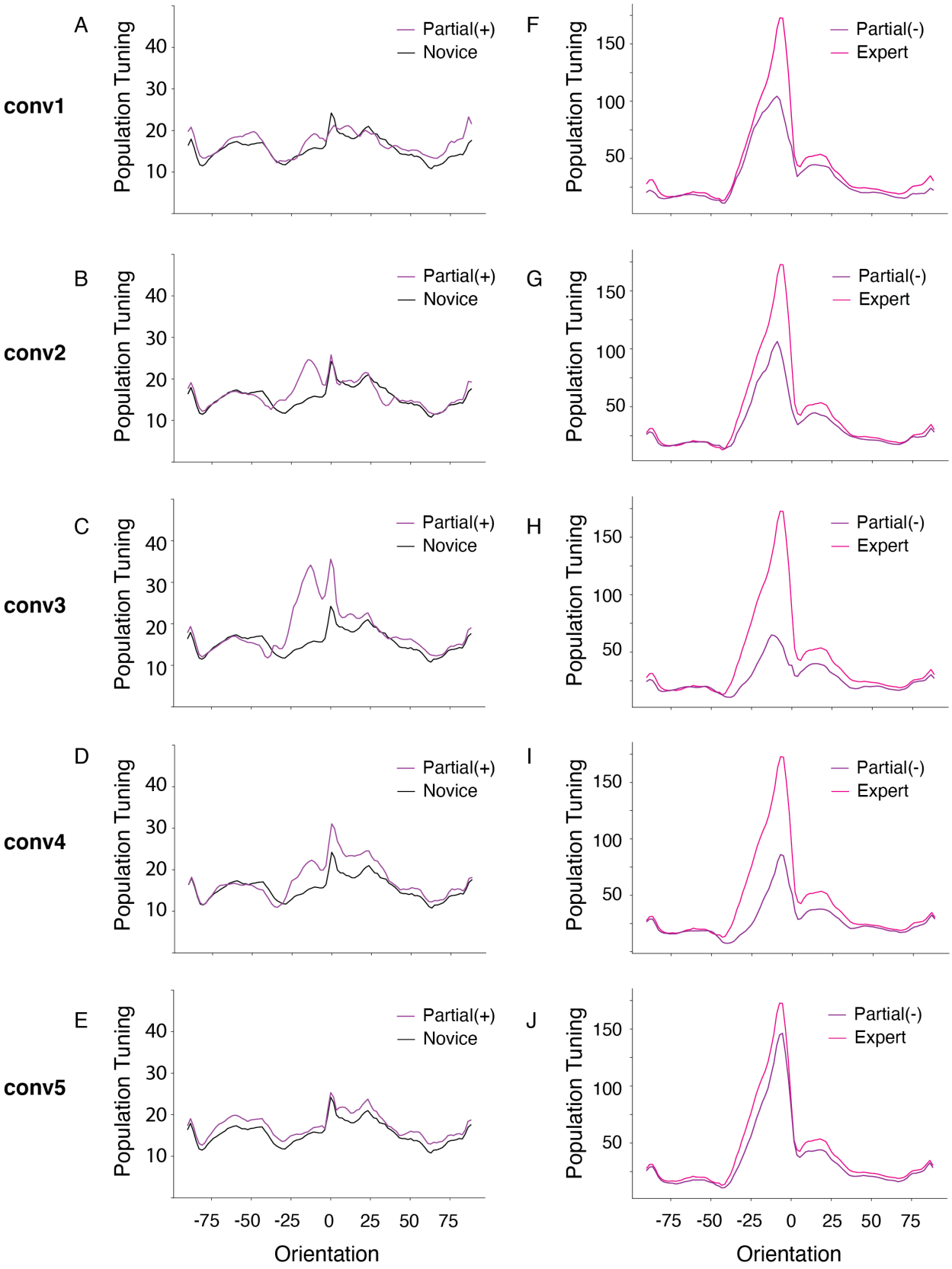
A
B
C
D
E
F
G
H
I
J
conv1
conv2
conv3
conv4
conv5
Population Tuning
Partial(+)
Novice
Partial(-)
Expert
Orientation
-75 -50 -25 0 25 50 75
10 20 30 40
50 100 150

Intriguingly, we observed a dramatic difference between the Easy-Hard_net and the Hard_net in the extent to which weight plasticity in conv1 and conv2 was leveraged. In the Easy-Hard_net, the absence of perceptual learning-induced weight change in conv1 led to a 68% reduction in the slope of the conv5 population at the trained reference, and the exclusion of plasticity in conv2 reduced discriminability by 70% (Figure 4.9F-G, Table 4.6). The same perturbations led to only a 32% and 47% reduction in discriminability in Hard_net conv5 (Figure 4.4A-B, Table 4.2). Thus, the Easy-Hard_net relied more heavily on plasticity within conv1 and conv2 than the Hard_net.

In both networks, the absence of weight plasticity in conv3 most strongly impacted the discriminability of conv5, though this impact was greater in the Easy-Hard_net than the Hard_net (87% and 78% reduction in discriminability in the Easy-Hard_net and Hard_net, respectively). Interestingly, although the absence of plasticity in conv4 led to a comparable deficit in both the Easy-Hard_net and the Hard_net (66% and 70%, respectively), the impact of conv4 plasticity alone on conv5 was much more broadly distributed in the Easy-Hard_net than the Hard_net (Figure 4.9D vs Figure 4.3D). Moreover, the relative influence of excluding conv4 plasticity was comparable to the influence of excluding plasticity from conv1 and conv2 in the Easy-Hard_net, whereas the influence of excluding conv4 plasticity overshadowed the influence of excluding conv1 and conv2 plasticity in the Hard_net.

Layer	% slope at the trained orientation in conv5 with a single layer's weight change	% slope at the trained orientation in conv5 without a single layer's weight change
Conv1	3%	32%
Conv2	2%	30%
Conv3	4%	13%
Conv4	5%	34%
Conv5	4%	79%

Table 4.6 Effects of plasticity within each layer of the Easy-Hard_net on the discriminability of conv5.

Left column: Percent of the slope at the trained orientation in conv5 of the Easy-Hard_net that can be achieved when the learning-induced weight changes from a single convolutional layer was selectively loaded into the novice network. Right column: Percent of the slope at the trained orientation in conv5 of the Easy-Hard_net that can be achieved when the weights of a single convolutional layer were replaced with weights from the novice network.

Thus far, we have investigated the consequences of training on an easy task before training on a difficult task. As a final analysis, we sought to gain insight into how training on an easy task enhanced subsequent learning. Conceptual frameworks (Ahissar and Hochstein, 2004), and signal detection theory-based computational models (Liu and Weinshall, 2000), have posited that learning an easy task facilitates learning of a more difficult task by pre-determining which neurons are the most informative to the classification, and subsequently guiding plasticity to begin with these neurons. Thus, we investigated whether training history influenced which neurons underwent the most plasticity in the difficult discrimination task.

For this analysis, we measured the weight plasticity of individual neurons before and after training in the Easy_net and in the Easy-Hard_net (see *Methods: Analysis: Weight change)*.

For the Easy_net, this resulted in the difference between the weights as they were initialized in the novice network and the weights learned by the end of training on the 20° discrimination task. For the Easy-Hard_net, this resulted in the difference between the Easy_net weights that were used to initialize the Easy-Hard_net and the weights acquired after subsequently learning the 1° discrimination. We then plotted the weight change of neurons in the Easy-Hard_net against the weight change of neurons in the Easy_net (Figure 4.10), and quantified the strength of the relationship between weight change in the two networks as the ratio of the eigenvalues of the covariance matrix (Table 4.7). The first eigenvector of the covariance matrix represents the vector that points in the direction of the greatest spread in the data, and its corresponding eigenvalue represents the degree of that spread. The second eigenvector is orthogonal to the first, and the second eigenvalue represents the spread of the data along this orthogonal dimension. Thus, the ratio of the eigenvalues of the covariance matrix represent the ellipticity of the data – intuitively, how much the data is different from a cloud of white noise. For nonzero covariance, this ellipticity may be used as a metric for how strongly the two variables vary together in a particular direction.

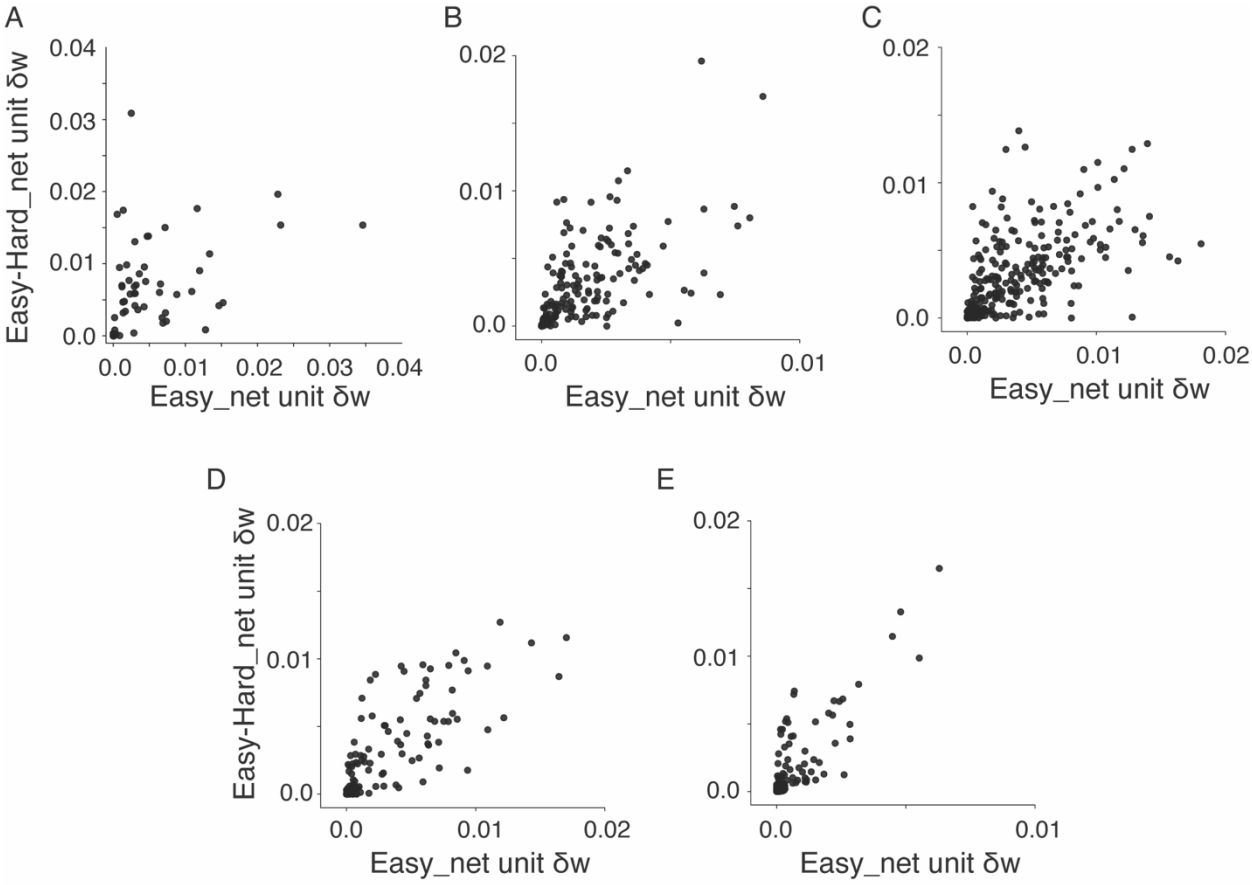

Figure 4.10 Individual weight changes in the Easy-Hard_Net versus the Easy_Net by layer.

(A-E) *Correspondence between weight changes in the Easy-Hard_net versus the Easy_net in layers conv1-conv5 respectively.*

There is a clear, strong relationship between the networks in conv4 and conv5, where neurons that were most plastic in the Easy_net continued to be the most plastic in the Easy-Hard_net (Figure 4.10D-E, Table 4.7). Yet, this relationship weakened at progressively lower levels of the network. By contrast, when we compared individual neuron's weight changes between the Easy-Hard_net to the Hard_net, we observed the strongest relationship between weight change in the first convolutional layer, and the weakest relationship between weight change in the last convolutional layer (Figure 4.11, Table 4.7). Thus, task difficulty seemed to

most strongly direct weight change at early stages of the hierarchy, while training history most strongly influenced weight change at late stages of the hierarchy.

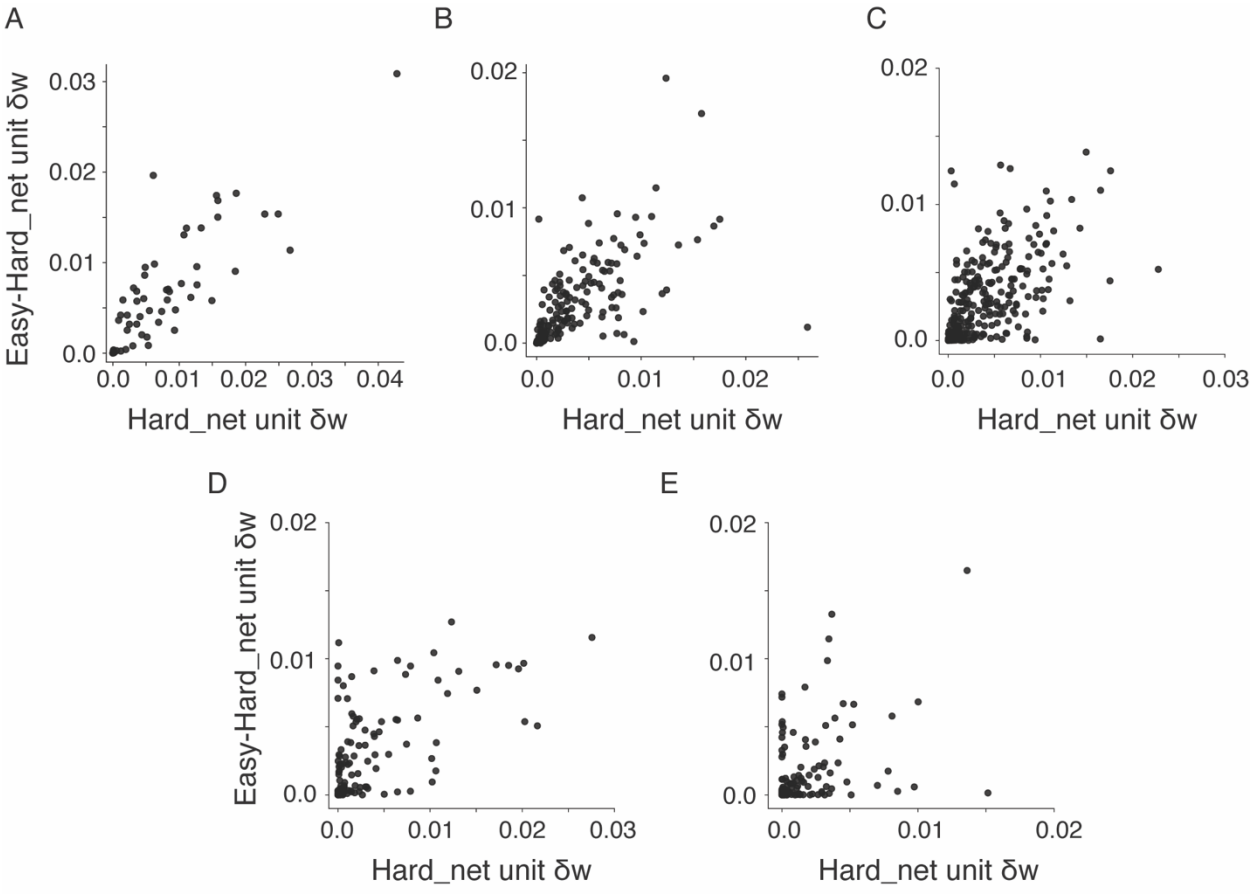

Figure 4.11 Individual weight changes in the Easy-Hard_Net versus the Hard_Net by layer.

(A-E) *Correspondence between weight changes in the Easy-Hard_net versus the Hard_net in layers conv1-conv5 respectively.*

Layer	Ratio of the eigenvalues of cov(Easy_net, Easy_hard_net)	Ratio of the eigenvalues of cov(Hard_net, Easy-Hard_net)
Conv1	2.55	12.89
Conv2	7.22	5.43
Conv3	7.43	5.49
Conv4	14.85	6.67
Conv5	31.58	2.98

Table 4.7 Quantification of the relationship between individual weight change in Easy-Hard_net and individual weight change in the Easy_net and Hard_net.

4.4 Discussion

To date, there has been little investigation into how learning-induced plasticity within a particular visual area impacts subsequent stages of processing downstream, nor how plasticity across multiple areas might work together in concert. Here, we leveraged a deep neural network to investigate the cascading effects of visual perceptual learning across a hierarchy of visual processing stages. Through this lens, we observed that plasticity within early layers of the network is amplified through plasticity in subsequent layers of processing. This finding offers an alternative view to the notion that perceptual learning gains arise from a particular origin of plasticity: instead, we show how perceptual gains could arise from coordinated plasticity across layers. Importantly, by comparing the effects of learning between an easy task and a difficult task, we found that task precision influenced how broadly neurons were recruited to inform the classification at all layers of the network, rather than which layer exhibited the greatest plasticity. This finding is significant, because task difficulty has historically been thought to

influence the locus of learning-induced plasticity (Ahissar and Hochstein, 2004; Watanabe and Sasaki, 2015). Along a similar vein, training on an easy task before training on a difficult task enhanced the read out from neurons in low levels of the hierarchy in a subtle, distributed manner that made little impact on the tuning properties of neurons in the network. Thus, our framework offers novel hypotheses for how these task manipulations influence learning-induced plasticity.

In what follows, we discuss our findings in more detail, and in the context of prominent theoretical frameworks and models of perceptual learning.

4.4.1 Learning-induced plasticity across layers enhances the feedforward input from a V1-like area

When we examined the way that plasticity within a particular layer of the network worked together with plasticity across all layers, we observed that conv3 plasticity was especially important for enhancing the discriminability of conv5, the last visual processing layer in the network. In particular, replacing the learned weights in conv3 with weights from the novice network substantially decreased the discriminability of conv5. As touched upon in the results, plasticity within conv3 reflects reweighting the inputs from conv2, and conv2 has previously been shown to exhibit representational similarity with V1 (Güçlü and Gerven, 2015; Khaligh-Razavi and Kriegeskorte, 2014). Thus, our results suggest that reweighting V1-like inputs is an important aspect of visual perceptual learning in the deep network.

The theory that perceptual learning arises from an enhanced read-out of V1 activity has been advanced by Dosher and Lu through a series of computational modeling and psychophysical studies (Dosher and Lu, 1998; Petrov et al., 2005, 2006), and has gained

considerable prominence in the field of perceptual learning (Dosher and Lu, 2017). However, the computational models that implement selective reweighting of V1 inputs have all been relatively shallow models with direct input from V1 to decision units (Dosher et al., 2013; Petrov et al., 2005, 2006; Poggio et al., 1992; Sotiropoulos et al., 2011, 2018; Weiss et al., 1993; Zhaoping et al., 2003). It was hitherto unclear that reweighting V1-like inputs would be as important in a deep, strictly hierarchical neural network, where low-level activity must pass through several additional processing stages before reaching decision units. Therefore, the finding that conv3 plasticity is critical in a deep network adds weight to the hypothesis that refining V1-like input is important for perceptual gains in humans.

4.4.2 The plasticity within any single layer is inconsequential on its own

At the same time, our results expressly show that reweighting of V1-like inputs on its own is not enough – downstream plasticity must work to complement mid-level plasticity. We observed that there was no single layer that exhibited weight plasticity powerful enough to meaningfully influence the discriminability of conv5. At best, the weight plasticity of individual layers could account for 5% of the full network's sensitivity to the trained stimulus. This finding adds weight to the view that plasticity in a single visual area is only meaningful when considered in the context of plasticity within the rest of the network. Moreover, though the absence of plasticity within conv3 was consistently the most impactful on all networks, the absence of plasticity within conv1, conv2, and conv4 also substantially diminished the discriminability of conv5. Thus, our results show that perceptual learning in a deep neural network is a distributed process that cannot be localized exclusively to any particular layer.

4.4.3 Task difficulty influences how selectively the read-out of sensory information is enhanced

Task difficulty has traditionally been thought to influence the locus of learning-induced plasticity, such that easier tasks induce plasticity in visual areas with broader receptive fields and more difficult tasks induce plasticity in visual areas with more selective receptive fields (Ahissar and Hochstein, 1997, 2004). This hypothesis is based on behavior: specifically, it is assumed that because perceptual gains transfer more broadly to untrained stimulus features in low precision tasks, learning-induced plasticity must originate from a mid-level area where neurons exhibit broader receptive fields (Watanabe and Sasaki, 2015). Because the network also exhibits greater transfer for low precision tasks, as well as a hierarchy of receptive field breadth and complexity (Cichy et al., 2016; Eickenberg et al., 2017; Güçlü and Gerven, 2015), we can test the assumptions of this hypothesis in the deep network.

Both our work and the work of Wenliang & Seitz (Wenliang and Seitz, 2018) showed that the layer-wise distribution of weight plasticity in the network and tuning properties are unchanged by task difficulty: tuning plasticity increased along the hierarchy and weight plasticity decreased along the hierarchy, regardless of task difficulty. This is not to say that task difficulty did not impact the degree of plasticity – in particular, tuning plasticity was much greater after learning the high precision task across all levels of the hierarchy. However, these results suggest that task precision need not impact the locus of plasticity in the visual hierarchy. More fundamentally, these results suggest that merely observing that tuning properties change minimally or not at all in a given visual area cannot be used to infer that plasticity did not occur, or even originate, in that visual area.

Instead, we found that task difficulty impacted the size of the population of neurons that were informative to the classification, where more neurons were informative to an easy, 20° discrimination task than a hard, 1° discrimination task. Along a similar vein, we also saw that plasticity within mid stages of the network acted more broadly on conv5 after learning an easy discrimination task than after learning a difficult discrimination task. Taken together, our results advance the simple idea that task difficulty affects how selective downstream units are in reweighting the responses of neurons upstream. In a way, this idea was already implicitly embedded in the hypothesis that the locus of plasticity would change with task difficulty: the broadening of receptive fields up the hierarchy arises from pooling over increasingly diverse populations of neurons in early visual areas. Yet, by showing that task difficulty need not lead to more plasticity at mid or late visual processing stages relative to early ones, our results call for a return to the core intuition that task difficulty affects the breadth of the neuronal population that contributes to the discrimination, rather than making the additional assumption that the distribution of plasticity across stages of the visual hierarchy will also change.

The prediction that easy tasks recruit from a broader population of neurons than difficult tasks could be tested experimentally by selectively reducing the responses of neurons tuned for various orientations using an adaptation paradigm, and measuring the resulting impact on discrimination (Hol and Treue, 2001). If it is the case that easy tasks recruit from a broader population of neurons, then it would be expected that the range of adapting stimuli that impact performance is larger in an easy task than in a difficult task.

4.4.4 Training history affects the importance of low-level plasticity, but not its extent

A particularly interesting phenomenon in the field of perceptual learning is that learning an easy task expedites subsequent learning of a more difficult task (Ahissar and Hochstein, 1997; Liu and Weinshall, 2000; Rubin et al., 1997), sometimes even making learning a difficult task possible where it would be impossible otherwise (Ahissar and Hochstein, 1997). Understanding the way that learning an easy task before learning a difficult task affects plasticity could therefore shed light into the conditions that facilitate learning. We found that the amount of evidence that neurons provided for the classification was significantly higher in the Easy-Hard_net than in the Hard_net for the layers conv1, conv2, and conv4, while the tuning properties of neurons in conv1 – conv4 were not statistically different between the two networks. Putting these two results together is important, as it shows that tuning plasticity is not necessary to enhance the information that neurons provide for the classification: this enhancement can instead be achieved through how neurons in the network are reweighted. This is similar to what has been argued by Dosher and Lu, but extended to a deep neural network (Dosher and Lu, 1998).

Intriguingly, training on an easy task before training on a difficult task also impacted how much plasticity within early stages of the network influenced the discriminability of the output of the network. Specifically, the exclusion of plasticity arising from either of the first two layers of the network reduced the discriminability of conv5 much more dramatically in the Easy-Hard_net than in the Hard_net. This suggests that training on an easy discrimination before training on a more difficult discrimination caused the network to amplify the effects of plasticity within early layers of the network to a greater degree.

4.4.5 The reverse hierarchy theory successfully predicted individual neurons' weight change trends

Training a deep neural network on an easy task before a difficult task also allowed us to investigate particular predictions of the reverse hierarchy theory, which is the only descriptive model available for how perceptual learning should impact a hierarchical network (Ahissar and Hochstein, 2004). The reverse hierarchy theory is widely cited for suggesting that task difficulty should determine the locus of plasticity, where easy tasks induce plasticity at mid stages of the hierarchy and more difficult tasks induce plasticity at early stages of the hierarchy. As discussed above, this prediction does not hold in the deep neural network. However, the reverse hierarchy theory also makes particular predictions for how learning an easy task should facilitate subsequent learning on a more difficult task. Specifically, the reverse hierarchy theory predicts that learning an easy task should pre-select which neurons are most informative to the classification at mid to late stages of the network, and should therefore inform which weights change as a result of the difficult task in a cascade from top to bottom. We see something similar to this hypothesis in the deep network: specifically, we see that in conv4 and conv5, the neurons that undergo the most weight change after learning the easy task are also the neurons that continue to undergo the most weight change after learning the hard task. Additionally, we see that the neurons that undergo the most weight change in conv1 and conv2 are more similar in the Easy-Hard_net and the Hard_net, suggesting that task difficulty has a greater influence on low-level plasticity than training history. This idea is also supported by the reverse hierarchy theory, which posits that low-level plasticity is more strongly affected by task precision (Ahissar and Hochstein, 2004). To our knowledge, our work is the first rigorous computational assessment of the reverse hierarchy theory's hypotheses about training history.

4.4.6 Comparison of deep neural network models of visual perceptual learning to other models

Deep neural network models have several limitations. Generally, although there are distinct similarities between the organization and tuning properties of visual cortex and deep neural networks (Cichy et al., 2016; Eickenberg et al., 2017; Güçlü and Gerven, 2015; Khaligh-Razavi and Kriegeskorte, 2014; Pospisil et al., 2018; Zeiler and Fergus, 2013), they are far from homologous (Lindsay, 2020; Serre, 2019). Thus, there is a limit to how much findings in the network could be mapped onto particular areas of the brain. Additionally, the learning rule implemented in this deep neural network (backpropagation via stochastic gradient descent), is not biologically plausible (but see Lillicrap et al., 2020). Models that implement alternative learning rules, inspired by Hebbian plasticity or reward prediction error, might offer a different and more accurate prediction for how learning-induced plasticity works together across the visual hierarchy. What's more, parameter decisions made by the experimenter, such as the learning rate and zero-initialization of the classification weights, may have influenced the distribution of plasticity throughout the network. Future experiments are needed to investigate how robust our results are to changes in these parameters.

Ultimately however, the most important consideration for choosing a computational model is the question being asked. The rigid hierarchy of this network precludes the possibility of studying the interaction between learning and attention (Roelfsema and Van Ooyen, 2005), the degree to which perceptual learning influences recurrent connections between neurons (Bejjanki et al., 2011; Teich and Qian, 2003), or even whether plasticity would be distributed differently through the network if low-level or intermediate visual stages could project directly to decision areas (Dosher et al., 2013; Sotiropoulos et al., 2018; Talluri et al., 2015). What's

more, the influence of correlated noise can only be considered in spiking models of perceptual learning (Bejjanki et al., 2011; Law and Gold, 2009). All of these questions are important to understanding perceptual learning, and all are better addressed with alternative computational models. Yet, here we argue that understanding the cascading effects of learning-induced plasticity throughout the visual hierarchy is also important for understanding perceptual learning, especially given the observation that learning induces tuning curve changes in multiple visual areas (Adab and Vogels, 2011; Adab et al., 2014; Raiguel et al., 2006; Schoups et al., 2001; Yang and Maunsell, 2004). For this, a deep hierarchical model is needed.

4.4.7 Conclusion

In all, our work advances a new conceptual framework for understanding visual perceptual learning as a cascade of plasticity throughout a hierarchical network. Most importantly, our work challenges the view that understanding perceptual learning can be reduced to investigating plasticity within a given visual area. Moreover, our results highlight the importance of investigating the effects of perceptual learning beyond changes in tuning properties, as tuning properties alone are insufficient to reveal the extent of learning-induced plasticity in a given area. Taken together, our work can be used to inspire future experiments that investigate perceptual learning across the visual hierarchy.

5 Discussion

Since its formal characterization in the 1980s and 1990s, the seemingly simple phenomenon of visual perceptual learning has turned out to be anything but simple. The early hypothesis that perceptual gains could be accounted for by changes in the tuning properties of single neurons in V1 turned out to reveal more about the ideas of neural encoding and decoding at the time than the phenomenon of visual perceptual learning itself. Instead and increasingly, the field has called for population level approaches to studying visual perceptual learning, as well as approaches that consider perceptual learning across visual areas, across spatial scales, and across time. This thesis makes two contributions towards these aims: it lays the groundwork for chronic two-photon imaging in behaving ferrets, and it advances the use of deep convolutional neural networks for studying perceptual learning across visual processing stages.

Ferrets as a model for studying visual perceptual learning

First and foremost, the present work advances the ferret as an animal model for studying visual perceptual learning. In chapter 2, we show that ferrets are able to learn a variety of visual tasks with low lapse rates, and that their behavior is well-described by standard psychometric functions. In general, these characteristics of their performance indicate that their behavior is under tight stimulus control. We also show that their behavioral sensitivity to motion coherence agrees well with the sensitivity of PSS neurons to motion coherence. Additionally, preliminary data shows that ferrets exhibit perceptual learning in motion and orientation discrimination tasks (Dunn-Weiss et al., 2019b). Thus, we find that ferrets are good behavioral subjects for visual learning studies.

The ferret is a particularly valuable animal model because it offers a bridge between research in different species, sharing experimental advantages with the rodent and cortical homologies with the primate. Though the field of visual perceptual learning has been dominated by research in macaques and humans, perceptual learning research in rodents has been instrumental in investigating the circuit-level plasticity underlying perceptual gains. For instance, slice physiology in rats showed that visual perceptual learning induced long term potentiation (LTP) of both horizontal and vertical inputs to V1 layer II/III (Sale et al., 2011). Similarly, repeated presentation of an oriented grating across days was shown to exhibit the same properties as LTP (Cooke and Bear, 2010; Frenkel et al., 2006). Significantly, learning-induced LTP has been shown to be able to recover perceptual deficits in amblyopic rats (Baroncelli et al., 2012). More generally, optogenetic circuit manipulations in rodents have provided insight into the circuit mechanisms underlying visual behavior by identifying the roles of different interneurons in detection tasks (Katzner et al., 2019). Modulating the activity of these interneurons has been shown to improve perceptual learning in mouse models of Fragile X syndrome (Goel et al., 2018). Thus, not only has perceptual learning research in rodents provided insight into the circuit-level plasticity underlying visual perceptual learning, but also, rodent research has exhibited promising clinical applications.

What's more, chronic two-photon imaging in mice has investigated important questions such as how task context modulates neural activity, and how learning affects neural activity at the population level (Carrillo-Reid et al., 2019; Montijn et al., 2015; Peters et al., 2014; Poort et al., 2015). In particular, by imaging the same cells in V1 across days while mice learned a visual discrimination task, Poort and colleagues showed that the response preferences of individual

neurons became more consistent with learning (Poort et al., 2015). Importantly, enhanced orientation selectivity was also observed, but only within the task context – not during passive viewing. Other studies have shown that the spatiotemporal population activity patterns become more stereotyped in both visual and motor cortex following visual and motor learning respectively, and that these reproducible patterns are associated with behavioral outputs (Carrillo-Reid et al., 2019; Peters et al., 2014). Compellingly, Carrillo-Reid and colleagues showed that behavioral performance in a go/no-go visual discrimination task could be modulated by disrupting or activating the particular set of V1 neurons that were driven by the stimulus associated with the go cue. These results strongly suggest that the stereotyped population activity that developed with learning was behaviorally relevant, and not merely an epiphenomenon.

The primate neurophysiology studies that have dominated the field of visual perceptual learning have been single-unit recordings that have looked at the time-averaged responses of neurons outside of the task context. Thus, chronic two-photon research in rodents is important, because it demonstrates that classic approaches may have missed more nuanced, distributed, and task-specific consequences of perceptual learning. However, translating between rodent and primate studies has been challenging because of distinct differences between their visual systems, both in terms of function and in terms of organization. Rodents have much lower visual acuity, less binocularity, and the more commonly used rodent models also exhibit a bias for low light conditions (Huberman and Niell, 2011). Additionally, the rodent visual system has fewer visual areas, larger receptive fields, and a different functional organization of primary visual cortex (Huberman and Niell, 2011; Ohki and Reid, 2007; Wang and Burkhalter, 2007).

Though the significance of each of these differences is still debated, these differences do mean that findings in the rodent cannot immediately be assumed to generalize to primates. By the same token, the experimental manipulations that have been so fruitful in rodent research – such as optogenetics, chronic two-photon imaging, and developmental manipulations – are challenging to implement in primates. Thus, there is a need for an animal model that can provide a bridge between these two species. The ferret provides this bridge, sharing important cortical homologies with the primate such as functional maps in V1 (Chapman et al., 1996; Redies et al., 1990; Yu et al., 2005) and much of the genetic tools and developmental accessibility of rodent research. Furthermore, investigating perceptual learning in the ferret and comparing the results to rodents and primates would provide a means of investigating which aspects of learning-induced plasticity generalize across species.

Chronic two-photon imaging in the ferret

The ferret's amenability to chronic two-photon imaging is of particular value, as chronic two-photon imaging permits the study of learning as a dynamic process at multiple spatial scales – enabling the study of spines, single neurons, and neural population activity. Typically, performing chronic two-photon imaging in behaving animals requires head fixation, unless a miniscope is used (Helmchen et al., 2001). Therefore, in chapter 2 we also describe the development of a head-fixed behavioral setup that may be used in imaging experiments, and in chapter 3, we describe the development of a chronic imaging chamber implant. Our head-fixed behavioral set up is designed for two-alternative forced-choice tasks, and includes movable spouts that give temporally precise feedback to the animal. The fact that the spouts are movable also allow for the visual stimulus to be presented while the spouts are out of the

animal's reach. This is important, as it creates a distinct epoch for recording neural activity that is specifically related to the visual stimulus, separate from neural activity that is related to licking activity, or to the receipt and consumption of reward. It also helps minimize motion artifacts due to licking during the visual stimulus presentation.

The chronic imaging chamber that we developed is specifically optimized for long-term imaging in adult ferrets, and we demonstrate the ability to image cells chronically in an awake animal for up to 9 weeks. In particular, our design features an artificial dura, which helps prevent tissue growth over the imaging region, exhibits optical clarity, and permits viral injections through the silicone. Taken together, our work advances the potential for chronic two-photon imaging in ferrets while they perform a visual perceptual learning task.

However, there are additional steps that should be taken to complete and strengthen our designs. First, the head-fixed behavioral setup should be augmented with an eye-tracking system. Eye-tracking is important for verifying that the ferret is attending to the visual stimulus, and is essential for neural recordings in order to keep the visual stimulus within the neuron's receptive field. In addition, there are three important challenges to performing chronic imaging in awake animals that are not addressed by this thesis. The first is motion correction. Motion artifacts are a particular concern for experiments in behaving animals. Recent advances in 3D motion correction for two-photon imaging will be of value for addressing this concern (Griffiths et al., 2020). The second is returning to the same cells repeatedly across days and weeks. This is crucial for tracking learning-induced plasticity. Towards this end, a process that reliably aligns the objective to kinematic markers on the imaging implant (Choi et al., 2018), or a post-hoc analysis that localizes cells within a 3D volumetric scan is needed.

The final challenge for performing long-term chronic two-photon imaging is choosing the appropriate virus. The most common viral vector for genetically-encoded calcium-indicators (GECIs) is adeno-associated virus (AAV), and the most common GECI is GCaMP. Yet, different AAV serotypes exhibit different tropism and viral spread (Aschauer et al., 2013; Daniels et al., 2016; Nathanson et al., 2009; Watakabe et al., 2015), and different GCaMP sensors exhibit different baseline fluorescence, response kinetics, and sensitivity for calcium (Chen et al., 2013b; Dana et al., 2019). Moreover, these effects have been shown to differ between species (Watakabe et al., 2015). Importantly, overexpression is a problem for GECIs because it can disrupt calcium homeostasis. The extent of expression depends on all of the factors enumerated above, as well as time: transgene expression has been shown to increase over months, and with this increase in expression, the number of unhealthy cells also increases (Chen et al., 2013b; Tian et al., 2009). Thus, different viruses may differentially impact the health of the transfected cells over time, and the viability of a virus in one species does not guarantee viability in another species.

We tried two different viruses in our chronic implant: AAV1-syn-GCaMP6f, and AAV5-TRE3-GCaMP6f + AAV5-mThy1PSs-TtAad. We chose GCaMP6f as the sensor because of its fast kinetics, and started with AAV1-syn-GCaMP6f because we had used it successfully in acute experiments after two weeks of expression. However, in the chronic implant, we found AAV1-syn-GCaMP6f expression to be too dim, and were unable to visualize cells at all. We then tried AAV5-TRE3-GCaMP6f + AAV5-mThy1PSs-TtAad. This system, developed in marmosets, uses tetracycline-inducible gene expression to amplify expression of the AAV-GCaMP construct and therefore amplify GCaMP6f calcium signals (Sadakane et al., 2015). With this system, we were

able to visualize cells for up to 9 weeks. However, we observed the cells to be unusually quiescent, and were unable to drive visual responses at any point. When we performed a series of follow-up acute anesthetized terminal experiments with the AAV5-TRE3-GCaMP6f + AAV5-mThy1PSs-TtAad system, we observed a substantial proportion of cells with nuclear fluorescence after just four weeks of expression (Dunn-Weiss et al. 2019). Thus, the Tet-inducible system, in its current form, is not a viable option for ferrets. Finding a viable virus for chronic two-photon imaging of visually responsive cells in the adult ferret is imperative for continuing this work. Successful reports of chronic imaging in visual cortex of ferret kits with AAV2/1-GCaMP6s (Chang et al., 2020; Smith et al., 2018) suggest that AAV2/1-GCaMP6s may be a promising avenue.

Future chronic two-photon imaging experiments in the ferret

Though more work needs to be done, this thesis lays important groundwork for studying visual perceptual learning using chronic two-photon imaging in ferrets. The potential power of this approach is illustrated by the following lines of inquiry that could be pursued in the future:

1. *Orientation map stability across learning*. A possible reason for why visual perceptual learning induces less tuning plasticity in V1 than perceptual learning in other modalities is that feature maps in V1 are extraordinarily specialized and exhibit exquisite orthogonalization of a multidimensional feature space (Hubel and Wiesel, 1962, 1974, 1977; Nauhaus et al., 2012, 2016; Swindale et al., 2000). Hence, tuning plasticity in one feature domain could disrupt this precise functional architecture. At the same time, fMRI studies of visual perceptual learning suggest the intriguing possibility that the

population of neurons responsive to the trained stimuli may expand transiently in an early phase of learning, and return to their baseline response properties at a later stage of learning (Yotsumoto et al., 2008). Since ferrets exhibit smoothly varying orientation maps like the primate, it would be possible to explore the stability of these maps, as well as the tuning properties of individual neurons, across learning.

2. *Distributed network-level effects of learning.* Fine visual discrimination tasks require a multi-step process: first a minute difference in the physical properties of visual stimuli must be detected, then this difference must be transformed into separable internal states that are finally decoded and mapped onto different behavioral outcomes. Learning can act on any of these stages: enhancing the ability of neurons to modulate their firing based on the physical properties of the stimuli, separating the internal representations of the stimuli along the decoding axis, or aligning the decoder to the axis at which the internal representations of the stimuli are most separable. The majority of perceptual learning research has focused on the first stage, asking how perceptual learning might enhance the sensory representation itself. Yet, given the rigidity of the functional architecture of V1, a more elegant solution might be to make the internal representations of the stimuli more separable – in other words, to make the population activity associated with each stimulus more distinct. This would be reflected in the development of distinct spatiotemporal population activity patterns associated with each of the trained stimuli. Examining V1's spatiotemporal population activity both within and outside the context of the task becomes possible with chronic two-photon

imaging, while error trials, catch trials, and manipulations of neural activity could shed light into the features that are behaviorally relevant.

3. *Circuit dynamics of learning-induced plasticity*. Imaging dendritic spines across learning in the ferret would be interesting because of the known organization of synaptic space in ferret V1. Specifically, the degree of spatial clustering between co-tuned synaptic inputs has been shown to predict the degree of orientation selectivity in layer II/III V1 neurons (Wilson et al., 2016), and overall, neighboring dendritic spines on ferret V1 neurons exhibit similar receptive field properties (Scholl et al., 2017). Thus, fine-scale chronic imaging in the ferret during visual perceptual learning might reveal shifts in synaptic spatial clustering that could give rise to enhanced orientation selectivity.

Hierarchical consequences of visual perceptual learning

The lines of inquiry enumerated above will provide valuable insight into learning-induced plasticity in V1 across time and across multiple spatial scales. Yet, investigating learning-induced plasticity in V1 is ultimately only a small part of understanding visual perceptual learning. For one, perceptual learning has been shown to impact the tuning properties of neurons and neural population activity in a number of visual areas along the ventral stream, including V1 (Ghose et al., 2002; Hua et al., 2010; van Kerkoerle et al., 2018; Schoups et al., 2001) V4 (Ni et al., 2018; Raiguel et al., 2006; Sanayei et al., 2018; Yang and Maunsell, 2004; Adab and Vogels, 2011) and PIT (Adab et al., 2014). For another, the hierarchical nature of visual processing means that any plasticity induced within V1 may have downstream ramifications. More broadly, it's unknown whether the tuning curve changes that

have been observed following perceptual learning arise from plasticity confined to the particular visual area of study, from the propagating effects of plasticity upstream, or through reweighting the inputs from the area below. Ultimately, understanding learning-induced plasticity as a cascade through multiple processing stages is essential in order to interpret the origins and significance of learning-induced plasticity within any given area.

Towards this end, hierarchical computational models of visual cortex are valuable because they provide an opportunity to monitor and manipulate the activity of and weighted connections between multiple stages of visual processing. Deep convolutional neural networks are, at present, considered to be state-of-the-art mechanistic models for hierarchical visual processing (Barrett et al., 2019; Kietzmann et al., 2019; Kriegeskorte, 2015; Lindsay, 2020). Therefore, in chapter 4, we used a deep convolutional neural network to investigate the distributed effects of visual perceptual learning *in silico*. In particular, we utilized a deep neural network to investigate the effects of task difficulty and training history on perceptual learning, both of which are thought to influence the locus of learning-induced plasticity. Significantly, we found that task difficulty did not affect which layer of the network exhibited the most plasticity, but rather influenced the breadth of the population of neurons that were informative to the classification at all layers of the hierarchy. Interestingly, we found that training on an easy task before training on a difficult task increased the influence of plasticity in early convolutional layers of the network, and led neurons in those layers to contribute more evidence to the classification. More broadly, our analytical approach gave us critical insight into the efficacy of plasticity within a single layer on tuning plasticity downstream, as well as the ways that tuning

plasticity within a single layer was amplified or refined by tuning plasticity at other visual processing stages.

Performing *in vivo* companion experiments in the brain to these *in silico* studies rests on three technical components. The first is recording from multiple brain areas at the same time. One potential avenue are Neuropixel probes (Jun et al., 2017), which have made it easier to perform electrophysiology in multiple areas at once. Neuropixel probes have 960 recording sites, and can span 4mm – 7.7mm (Steinmetz et al., 2018). Additionally, because they require minimal cabling, more than one probe may be implanted at the same time. Two chronically implanted probes yielded 700 well-isolated units across five brain structures in freely behaving mice (Jun et al., 2017). However, the lack of flexibility in a probe of this length may be an issue for chronic implants in larger animals, and localizing specific brain areas along the shank remains a challenge (Steinmetz et al., 2018).

The second technical component is the ability to measure the connectivity between neurons in different brain areas. Previously, antidromic and orthodromic activation have been used to identify projection neurons and targets along ascending visual pathways (Briggs and Usrey, 2007; Movshon and Newsome, 1996; Sommer and Wurtz, 2004), and spike-triggered local field potentials have also been used to identify monosynaptic connections between LGN and V1 (Bereshpolova et al., 2019; Jin et al., 2011). However, these approaches are fairly low-yield, and require knowledge of the particular hierarchy of the ascending pathway. An alternative avenue is to use recombinant rabies viral vectors for retrograde transsynaptic tracing (Wickersham and Feinberg, 2012). Recent developments have substantially reduced the cytotoxicity of rabies virus vectors, such that the functional and membrane properties of

neurons remain normal for at least several months (Chatterjee et al., 2018). This opens the door for chronic two-photon calcium imaging of mono-synaptic partners.

The third and final technical component is the ability to precisely manipulate the activity of neurons in one area while measuring the effects on their synaptic partners downstream. Towards this end, confined light emission techniques that can target specific neurons expressing an opsin – such as micro-LEDs integrated into silicone probes (Wu et al., 2015), and two-photon holographic optogenetics (Carrillo-Reid et al., 2017) - offer promising avenues.

Ultimately, a combination of all of these technical components is required to crack perceptual learning, which continues to pose a significant experimental challenge. In the meantime, strengthening the utility of deep convolutional neural networks as computational models of visual cortex will be important, either through efforts to make them more similar to the visual system (Lindsay, 2020; Serre, 2019), testing the differential predictions made by different network architectures (Bakhtiari, 2019), or through neurophysiology experiments that can help constrain the space of plausible models.

Conclusion

The tools we have fundamentally shape the questions we ask. By advancing chronic two-photon imaging in behaving ferrets, as well as the use of deep neural networks for studying visual perceptual learning, this thesis hopes to advance investigation into the distributed, far-reaching consequences of visual perceptual learning. In so doing, both our understanding of visual processing and our understanding of learning itself will advance.

6 Bibliography

Adab, H.Z., and Vogels, R. (2011). Practicing Coarse Orientation Discrimination Improves Orientation Signals in Macaque Cortical Area V4. Current Biology *21*, 1661–1666.

Adab, H.Z., Popivanov, I.D., Vanduffel, W., and Vogels, R. (2014). Perceptual Learning of Simple Stimuli Modifies Stimulus Representations in Posterior Inferior Temporal Cortex. Journal of Cognitive Neuroscience *26*, 2187–2200.

Adini, Y., Wilkonsky, A., Haspel, R., Tsodyks, M., and Sagi, D. (2004). Perceptual learning in contrast discrimination: The effect of contrast uncertainty. Journal of Vision *4*, 2–2.

Ahissar, M., and Hochstein, S. (1993). Attentional control of early perceptual learning. PNAS *90*, 5718–5722.

Ahissar, M., and Hochstein, S. (1996). Learning Pop-out Detection: Specificities to Stimulus Characteristics. Vision Research *36*, 3487–3500.

Ahissar, M., and Hochstein, S. (1997). Task difficulty and the specificity of perceptual learning. Nature *387*, 401–406.

Ahissar, M., and Hochstein, S. (2004). The reverse hierarchy theory of visual perceptual learning. Trends in Cognitive Sciences *8*, 457–464.

Andermann, M.L., Kerlin, A.M., and Reid, C. (2010). Chronic cellular imaging of mouse visual cortex during operant behavior and passive viewing. Front. Cell. Neurosci. *4*.

Arieli, A., Grinvald, A., and Slovin, H. (2002). Dural substitute for long-term imaging of cortical activity in behaving monkeys and its clinical implications. Journal of Neuroscience Methods *114*, 119–133.

Aschauer, D.F., Kreuz, S., and Rumpel, S. (2013). Analysis of Transduction Efficiency, Tropism and Axonal Transport of AAV Serotypes 1, 2, 5, 6, 8 and 9 in the Mouse Brain. PLOS ONE *8*, e76310.

Baker, G., Thompson, I., Krug, K., Smyth, D., and Tolhurst, D. (1998). Spatial-frequency tuning and geniculocortical projections in the visual cortex (areas 17 and 18) of the pigmented ferret. The European Journal of Neuroscience *10*, 2657–68.

Ball, K., and Sekuler, R. (1982). A specific and enduring improvement in visual motion discrimination. Science *218*, 697–698.

Ball, K., and Sekuler, R. (1987). Direction-specific improvement in motion discrimination. Vision Research *27*, 953–965.

Barlow, H.B. (1972). Single Units and Sensation: A Neuron Doctrine for Perceptual Psychology? Perception *1*, 371–394.

Baroncelli, L., Bonaccorsi, J., Milanese, M., Bonifacino, T., Giribaldi, F., Manno, I., Cenni, M.C., Berardi, N., Bonanno, G., Maffei, L., et al. (2012). Enriched experience and recovery from amblyopia in adult rats: Impact of motor, social and sensory components. Neuropharmacology *62*, 2388–2397.

Barrett, D.G., Morcos, A.S., and Macke, J.H. (2019). Analyzing biological and artificial neural networks: challenges with opportunities for synergy? Current Opinion in Neurobiology *55*, 55–64.

Bejjanki, V.R., Beck, J.M., Lu, Z.-L., and Pouget, A. (2011). Perceptual learning as improved probabilistic inference in early sensory areas. Nature Neuroscience *14*, 642–648.

Bereshpolova, Y., Stoelzel, C.R., Su, C., Alonso, J.-M., and Swadlow, H.A. (2019). Activation of a Visual Cortical Column by a Directionally Selective Thalamocortical Neuron. Cell Reports *27*, 3733-3740.e3.

Blakemore, C., and Campbell, F.W. (1969). On the existence of neurones in the human visual system selectively sensitive to the orientation and size of retinal images. J Physiol *203*, 237-260.1.

Born, R.T., and Bradley, D. (2005). Structure and Function of Visual Area MT. Annual Review of Neuroscience *28*, 157–189.

Bradley, A., Skottun, B.C., Ohzawa, I., Sclar, G., and Freeman, R.D. (1987). Visual orientation and spatial frequency discrimination: a comparison of single neurons and behavior. Journal of Neurophysiology *57*, 755–772.

Brainard, D.H. (1997). The Psychophysics Toolbox. Spat Vis *10*, 433–436.

Briggs, F., and Usrey, W.M. (2007). A Fast, Reciprocal Pathway between the Lateral Geniculate Nucleus and Visual Cortex in the Macaque Monkey. Journal of Neuroscience *27*, 5431–5436.

Britten, K.H., Shadlen, M.N., Newsome, W.T., and Movshon, J.A. (1992). The analysis of visual motion: a comparison of neuronal and psychophysical performance. J. Neurosci. *12*, 4745–4765.

Busse, L., Ayaz, A., Dhruv, N.T., Katzner, S., Saleem, A.B., Schölvinck, M.L., Zaharia, A.D., and Carandini, M. (2011). The Detection of Visual Contrast in the Behaving Mouse. J. Neurosci. *31*, 11351–11361.

Carrillo-Reid, L., Yang, W., Kang Miller, J., Peterka, D.S., and Yuste, R. (2017). Imaging and Optically Manipulating Neuronal Ensembles. Annual Review of Biophysics *46*, 271–293.

Carrillo-Reid, L., Han, S., Yang, W., Akrouh, A., and Yuste, R. (2019). Controlling Visually Guided Behavior by Holographic Recalling of Cortical Ensembles. Cell *178*, 447-457.e5.

Chang, J.T., Whitney, D., and Fitzpatrick, D. (2020). Experience-Dependent Reorganization Drives Development of a Binocularly Unified Cortical Representation of Orientation. Neuron.

Chapman, B., and Gödecke, I. (2000). Cortical Cell Orientation Selectivity Fails to Develop in the Absence of ON-Center Retinal Ganglion Cell Activity. J. Neurosci. *20*, 1922–1930.

Chapman, B., and Stryker, M.P. (1993). Development of orientation selectivity in ferret visual cortex and effects of deprivation. Journal of Neuroscience *13*, 5251.

Chapman, B., Stryker, M.P., and Bonhoeffer, T. (1996). Development of orientation preference maps in ferret primary visual cortex. J. Neurosci. *16*, 6443–6453.

Chatterjee, S., Sullivan, H.A., MacLennan, B.J., Xu, R., Hou, Y., Lavin, T.K., Lea, N.E., Michalski, J.E., Babcock, K.R., Dietrich, S., et al. (2018). Nontoxic, double-deletion-mutant rabies viral vectors for retrograde targeting of projection neurons. Nature Neuroscience *21*, 638–646.

Chen, J.L., Pfäffli, O.A., Voigt, F.F., Margolis, D.J., and Helmchen, F. (2013a). Online correction of licking-induced brain motion during two-photon imaging with a tunable lens. The Journal of Physiology *591*, 4689–4698.

Chen, L.M., Heider, B., Williams, G.V., Healy, F.L., Ramsden, B.M., and Roe, A.W. (2002). A chamber and artificial dura method for long-term optical imaging in the monkey. Journal of Neuroscience Methods *113*, 41–49.

Chen, T.-W., Wardill, T.J., Sun, Y., Pulver, S.R., Renninger, S.L., Baohan, A., Schreiter, E.R., Kerr, R.A., Orger, M.B., Jayaraman, V., et al. (2013b). Ultrasensitive fluorescent proteins for imaging neuronal activity. Nature *499*, 295–300.

Choi, J., Goncharov, V., Kleinbart, J., Orsborn, A., and Pesaran, B. (2018). Monkey-MIMMS: Towards Automated Cellular Resolution Large- Scale Two-Photon Microscopy In The Awake Macaque Monkey. In 2018 40th Annual International Conference of the IEEE Engineering in Medicine and Biology Society (EMBC), pp. 3013–3016.

Chowdhury, S.A., and DeAngelis, G.C. (2008). Fine discrimination training alters the causal contribution of macaque area MT to depth perception. Neuron *60*, 367–377.

Cichy, R.M., Khosla, A., Pantazis, D., Torralba, A., and Oliva, A. (2016). Comparison of deep neural networks to spatio-temporal cortical dynamics of human visual object recognition reveals hierarchical correspondence. Scientific Reports *6*, 1–13.

Clopper, C.J., and Pearson, E.S. (1934). The Use of Confidence or Fiducial Limits Illustrated in the Case of the Binomial. Biometrika *26*, 404–413.

Cooke, S.F., and Bear, M.F. (2010). Visual Experience Induces Long-Term Potentiation in the Primary Visual Cortex. J. Neurosci. *30*, 16304–16313.

Crist, R.E., Kapadia, M.K., Westheimer, G., and Gilbert, C.D. (1997). Perceptual Learning of Spatial Localization: Specificity for Orientation, Position, and Context. Journal of Neurophysiology *78*, 2889–2894.

Crist, R.E., Li, W., and Gilbert, C.D. (2001). Learning to see: experience and attention in primary visual cortex. Nat Neurosci *4*, 519–525.

Dakin, S.C., and Bex, P.J. (2002). Summation of concentric orientation structure: seeing the Glass or the window? Vision Research *42*, 2013–2020.

Dana, H., Sun, Y., Mohar, B., Hulse, B.K., Kerlin, A.M., Hasseman, J.P., Tsegaye, G., Tsang, A., Wong, A., Patel, R., et al. (2019). High-performance calcium sensors for imaging activity in neuronal populations and microcompartments. Nature Methods *16*, 649–657.

Daniels, D., Boucher, T., and Nielsen, K.J. (2016). Serotype-Specific Tropism of Adeno-Associated Viruses in Ferret Primary Visual Cortex. Soc Neurosci.

DeLoss, D.J., Watanabe, T., and Andersen, G.J. (2015). Improving Vision Among Older Adults: Behavioral Training to Improve Sight. Psychol Sci *26*, 456–466.

Denk, W., Strickler, J.H., and Webb, W.W. (1990). Two-photon laser scanning fluorescence microscopy. Science *248*, 73–76.

Dobbins, H.D., Marvit, P., Ji, Y., and Depireux, D.A. (2007). Chronically recording with a multi-electrode array device in the auditory cortex of an awake ferret. Journal of Neuroscience Methods *161*, 101–111.

Dorais, A., and Sagi, D. (1997). Contrast masking effects change with practice. Vision Research *37*, 1725–1733.

Dosher, B., and Lu, Z.-L. (2017). Visual Perceptual Learning and Models. Annual Review of Vision Science *3*, 343–363.

Dosher, B.A., and Lu, Z.-L. (1998). Perceptual learning reflects external noise filtering and internal noise reduction through channel reweighting. PNAS *95*, 13988–13993.

Dosher, B.A., and Lu, Z.-L. (2009). Hebbian reweighting on stable representations in perceptual learning. Learning & Perception *1*, 37–58.

Dosher, B.A., Jeter, P., Liu, J., and Lu, Z.-L. (2013). An integrated reweighting theory of perceptual learning. PNAS *110*, 13678–13683.

Doty, B.A., Jones, C.N., and Doty, L.A. (1967). Learning-Set Formation by Mink, Ferrets, Skunks, and Cats. Science *155*, 1579–1580.

Dunn-Weiss, E., Nummela, S.U., Lempel, A.A., Law, J.M., Ledley, J., Salvino, P., and Nielsen, K.J. (2019a). Visual Motion and Form Integration in the Behaving Ferret. Eneuro *6*, ENEURO.0228-19.2019.

Dunn-Weiss, E.L., Ross, J.J., and Nielsen, K.J. (2019b). Visual perceptual learning in the ferret. Soc Neurosci.

Eastman, K.M. (2012). PLDAPS: A Hardware Architecture and Software Toolbox for Neurophysiology Requiring Complex Visual Stimuli and Online Behavioral Control. FRONT NEUROINFORMATICS *6*.

Efron, B., and Tibshirani, R. (1986). Bootstrap Methods for Standard Errors, Confidence Intervals, and Other Measures of Statistical Accuracy. Statist. Sci. *1*, 54–75.

Eickenberg, M., Gramfort, A., Varoquaux, G., and Thirion, B. (2017). Seeing it all: Convolutional network layers map the function of the human visual system. NeuroImage *152*, 184–194.

Fahle, M. (2004). Perceptual learning: A case for early selection. Journal of Vision *4*, 4–4.

Fahle, M., and Edelman, S. (1993). Long-term learning in vernier acuity: Effects of stimulus orientation, range and of feedback. Vision Research *33*, 397–412.

Fahle, M., and Morgan, M. (1996). No transfer of perceptual learning between similar stimuli in the same retinal position. Current Biology *6*, 292–297.

Fahle, D.I. of B.R.M., Fahle, M., Poggio, T., and Poggio, P.T.A. (2002). Perceptual Learning (MIT Press).

Fahle, M., Edelman, S., and Poggio, T. (1995). Fast perceptual learning in hyperacuity. Vision Research *35*, 3003–3013.

Felleman, D.J., and Van Essen, D.C. (1991). Distributed hierarchical processing in the primate cerebral cortex. Cereb. Cortex *1*, 1–47.

Fiorentini, A., and Berardi, N. (1980). Perceptual learning specific for orientation and spatial frequency. Nature *287*, 43–44.

Fiorentini, A., and Berardi, N. (1981). Learning in grating waveform discrimination: Specificity for orientation and spatial frequency. Vision Research *21*, 1149–1158.

Frenkel, M.Y., Sawtell, N.B., Diogo, A.C.M., Yoon, B., Neve, R.L., and Bear, M.F. (2006). Instructive Effect of Visual Experience in Mouse Visual Cortex. Neuron *51*, 339–349.

Fritz, J., Shamma, S., Elhilali, M., and Klein, D. (2003). Rapid task-related plasticity of spectrotemporal receptive fields in primary auditory cortex. Nature Neuroscience *6*, 1216.

Gallant, J.L., Braun, J., and Van Essen, D.C. (1993). Selectivity for polar, hyperbolic, and Cartesian gratings in macaque visual cortex. Science *259*, 100–3.

Ghose, G.M., Yang, T., and Maunsell, J.H.R. (2002). Physiological Correlates of Perceptual Learning in Monkey V1 and V2. Journal of Neurophysiology *87*, 1867–1888.

Gibson, E.J. (1953). Improvement in perceptual judgments as a function of controlled practice or training. Psychological Bulletin *50*, 401–431.

Gilbert, C.D., Sigman, M., and Crist, R.E. (2001). The Neural Basis of Perceptual Learning. Neuron *31*, 681–697.

Glass, L. (1969). Moiré effect from random dots. Nature *223*, 578–580.

Glass, L., and Pérez, R. (1973). Perception of Random Dot Interference Patterns. Nature *246*, 360–362.

Goel, A., Cantu, D.A., Guilfoyle, J., Chaudhari, G.R., Newadkar, A., Todisco, B., de Alba, D., Kourdougli, N., Schmitt, L.M., Pedapati, E., et al. (2018). Impaired perceptual learning in a mouse model of Fragile X syndrome is mediated by parvalbumin neuron dysfunction and is reversible. Nature Neuroscience *21*, 1404–1411.

Green, D.M., and Swets, J.A. (1966). Signal detection theory and psychophysics. (Oxford, England: John Wiley).

Griffiths, V.A., Valera, A.M., Lau, J.Y., Roš, H., Younts, T.J., Marin, B., Baragli, C., Coyle, D., Evans, G.J., Konstantinou, G., et al. (2020). Real-time 3D movement correction for two-photon imaging in behaving animals. Nature Methods *17*, 741–748.

Grinter, E.J., Maybery, M.T., and Badcock, D.R. (2010). Vision in developmental disorders: is there a dorsal stream deficit? Brain Research Bulletin *82*, 147–60.

Güçlü, U., and van Gerven, M.A.J. (2015). Deep Neural Networks Reveal a Gradient in the Complexity of Neural Representations across the Ventral Stream. J. Neurosci. *35*, 10005–10014.

Güçlü, U., and Gerven, M.A.J. van (2015). Deep Neural Networks Reveal a Gradient in the Complexity of Neural Representations across the Ventral Stream. J. Neurosci. *35*, 10005–10014.

Harris, H., Gliksberg, M., and Sagi, D. (2012). Generalized Perceptual Learning in the Absence of Sensory Adaptation. Current Biology *22*, 1813–1817.

Heider, B., Nathanson, J.L., Isacoff, E.Y., Callaway, E.M., and Siegel, R.M. (2010). Two-Photon Imaging of Calcium in Virally Transfected Striate Cortical Neurons of Behaving Monkey. PLOS ONE *5*, e13829.

Helmchen, F., Fee, M.S., Tank, D.W., and Denk, W. (2001). A Miniature Head-Mounted Two-Photon Microscope: High-Resolution Brain Imaging in Freely Moving Animals. Neuron *31*, 903–912.

Hoel, P., Port, S., and Stone, C. (1971). Introduction to Statistical Theory. (Boston: Houghton, Mifflin), p. 83ff.

Hol, K., and Treue, S. (2001). Different populations of neurons contribute to the detection and discrimination of visual motion. Vision Research *41*, 685–689.

Hollensteiner, K.J. (2015). Crossmodal Integration Improves Sensory Detection Thresholds in the Ferret. PLOS ONE *10*, e0124952.

Homman-Ludiye, J., Manger, P., and Bourne, J.A. (2010). Immunohistochemical parcellation of the ferret (Mustela putorius) visual cortex reveals substantial homology with the cat (Felis catus). Journal of Comparative Neurology *518*, 4439–62.

Hua, T., Bao, P., Huang, C.-B., Wang, Z., Xu, J., Zhou, Y., and Lu, Z.-L. (2010). Perceptual Learning Improves Contrast Sensitivity of V1 Neurons in Cats. Current Biology *20*, 887–894.

Hubel, D.H., and Wiesel, T.N. (1962). Receptive fields, binocular interaction and functional architecture in the cat's visual cortex. J Physiol *160*, 106-154.2.

Hubel, D.H., and Wiesel, T.N. (1968). Receptive fields and functional architecture of monkey striate cortex. The Journal of Physiology *195*, 215–243.

Hubel, D.H., and Wiesel, T.N. (1970). The period of susceptibility to the physiological effects of unilateral eye closure in kittens. J Physiol *206*, 419–436.

Hubel, D.H., and Wiesel, T.N. (1974). Sequence regularity and geometry of orientation columns in the monkey striate cortex. Journal of Comparative Neurology *158*, 267–293.

Hubel, D.H., and Wiesel, T.N. (1977). Ferrier lecture - Functional architecture of macaque monkey visual cortex. Proceedings of the Royal Society of London. Series B. Biological Sciences *198*, 1–59.

Huberman, A.D., and Niell, C.M. (2011). What can mice tell us about how vision works? Trends in Neurosciences *34*, 464–473.

Hung, S.-C., and Seitz, A.R. (2014). Prolonged Training at Threshold Promotes Robust Retinotopic Specificity in Perceptual Learning. J. Neurosci. *34*, 8423–8431.

Hupfeld, D., Distler, C., and Hoffmann, K.-P. (2006). Motion perception deficits in albino ferrets (Mustela putorius furo). Vision Research *46*, 2941–2948.

Hupfeld, D., Distler, C., and Hoffmann, K.-P. (2007). Deficits of visual motion perception and optokinetic nystagmus after posterior suprasylvian lesions in the ferret (Mustela putorius furo). Exp Brain Res *182*, 509–523.

Huxlin, K.R., Martin, T., Kelly, K., Riley, M., Friedman, D.I., Burgin, W.S., and Hayhoe, M. (2009). Perceptual Relearning of Complex Visual Motion after V1 Damage in Humans. J. Neurosci. *29*, 3981–3991.

Ikezoe, K., Mori, Y., Kitamura, K., Tamura, H., and Fujita, I. (2013). Relationship between the Local Structure of Orientation Map and the Strength of Orientation Tuning of Neurons in Monkey V1: A 2-Photon Calcium Imaging Study. J. Neurosci. *33*, 16818–16827.

Jeffreys, H. (1998). The Theory of Probability (OUP Oxford).

Jin, J., Wang, Y., Swadlow, H.A., and Alonso, J.M. (2011). Population receptive fields of ON and OFF thalamic inputs to an orientation column in visual cortex. Nature Neuroscience *14*, 232–238.

Jun, J.J., Steinmetz, N.A., Siegle, J.H., Denman, D.J., Bauza, M., Barbarits, B., Lee, A.K., Anastassiou, C.A., Andrei, A., Aydın, Ç., et al. (2017). Fully integrated silicon probes for high-density recording of neural activity. Nature *551*, 232–236.

Karni, A., and Sagi, D. (1991). Where practice makes perfect in texture discrimination: evidence for primary visual cortex plasticity. PNAS *88*, 4966–4970.

Katzner, S., Born, G., and Busse, L. (2019). V1 microcircuits underlying mouse visual behavior. Current Opinion in Neurobiology *58*, 191–198.

van Kerkoerle, T., Marik, S.A., Meyer zum Alten Borgloh, S., and Gilbert, C.D. (2018). Axonal plasticity associated with perceptual learning in adult macaque primary visual cortex. Proceedings of the National Academy of Sciences *115*, 10464–10469.

Kerlin, A.M., Andermann, M.L., Berezovskii, V.K., and Reid, R.C. (2010). Broadly Tuned Response Properties of Diverse Inhibitory Neuron Subtypes in Mouse Visual Cortex. Neuron *67*, 858–871.

Khaligh-Razavi, S.-M., and Kriegeskorte, N. (2014). Deep Supervised, but Not Unsupervised, Models May Explain IT Cortical Representation. PLOS Computational Biology *10*, e1003915.

Kietzmann, T.C., McClure, P., and Kriegeskorte, N. (2019). Deep Neural Networks in Computational Neuroscience. Oxford Research Encyclopedia of Neuroscience.

Kiorpes, L. (2016). The Puzzle of Visual Development: Behavior and Neural Limits. J. Neurosci. *36*, 11384–11393.

Kiorpes, L., Price, T., Hall-Haro, C., and Anthony Movshon, J. (2012). Development of sensitivity to global form and motion in macaque monkeys (Macaca nemestrina). Vision Research *63*, 34–42.

Kiper, D.C., and Kiorpes, L. (1994). Suprathreshold contrast sensitivity in experimentally strabismic monkeys. Vision Research *34*, 1575–1583.

Kleiner,M, Brainard,D, Pelli, Denis, Ingling,A, Murray,R, and Broussard,C (2007). What's new in psychtoolbox-3. Perception *36*, 1–16.

Kriegeskorte, N. (2015). Deep Neural Networks: A New Framework for Modeling Biological Vision and Brain Information Processing. Annu. Rev. Vis. Sci. *1*, 417–446.

Krizhevsky, A. (2014). One weird trick for parallelizing convolutional neural networks. ArXiv:1404.5997 [Cs].

Krizhevsky, A., Sutskever, I., and Hinton, G.E. (2012). ImageNet Classification with Deep Convolutional Neural Networks. In Advances in Neural Information Processing Systems 25, F. Pereira, C.J.C. Burges, L. Bottou, and K.Q. Weinberger, eds. (Curran Associates, Inc.), pp. 1097–1105.

Laffray, S., Pagès, S., Dufour, H., Koninck, P.D., Koninck, Y.D., and Côté, D. (2011). Adaptive Movement Compensation for In Vivo Imaging of Fast Cellular Dynamics within a Moving Tissue. PLOS ONE *6*, e19928.

Law, C.-T., and Gold, J.I. (2008). Neural correlates of perceptual learning in a sensory-motor, but not a sensory, cortical area. Nature Neuroscience *11*, 505–513.

Law, C.-T., and Gold, J.I. (2009). Reinforcement learning can account for associative and perceptual learning on a visual-decision task. Nature Neuroscience *12*, 655–663.

Lempel, A.A., and Nielsen, K.J. (2019). Ferrets as a Model for Higher-Level Visual Motion Processing. Current Biology *29*, 1–13.

Levi, D.M., and Li, R.W. (2009). Perceptual learning as a potential treatment for amblyopia: A mini-review. Vision Research *49*, 2535–2549.

Lewis, T.L., Ellemberg, D., Maurer, D., Dirks, M., Wilkinson, F., and Wilson, H.R. (2004). A Window on the Normal Development of Sensitivity to Global Form in Glass Patterns. Perception *33*, 409–418.

Li, M., Liu, F., Jiang, H., Lee, T.S., and Tang, S. (2017). Long-Term Two-Photon Imaging in Awake Macaque Monkey. Neuron *93*, 1049-1057.e3.

Li, Y., Fitzpatrick, D., and White, L.E. (2006). The development of direction selectivity in ferret visual cortex requires early visual experience. Nature Neuroscience *9*, 676–681.

Li, Y., Van Hooser, S.D., Mazurek, M., White, L.E., and Fitzpatrick, D. (2008). Experience with moving visual stimuli drives the early development of cortical direction selectivity. Nature *456*, 952–956.

Lillicrap, T.P., Santoro, A., Marris, L., Akerman, C.J., and Hinton, G. (2020). Backpropagation and the brain. Nature Reviews Neuroscience *21*, 335–346.

Lindsay, G. (2020). Convolutional Neural Networks as a Model of the Visual System: Past, Present, and Future. Journal of Cognitive Neuroscience.

Liu, L.D., and Pack, C.C. (2017). The Contribution of Area MT to Visual Motion Perception Depends on Training. Neuron *95*, 436-446.e3.

Liu, Z., and Weinshall, D. (2000). Mechanisms of generalization in perceptual learning. Vision Research *40*, 97–109.

Lohse, M., Bajo, V.M., and King, A.J. (2019). Development, organization and plasticity of auditory circuits: Lessons from a cherished colleague. European Journal of Neuroscience *49*, 990–1004.

Maniglia, M., and Seitz, A.R. (2018). Towards a whole brain model of Perceptual Learning. Current Opinion in Behavioral Sciences *20*, 47–55.

Marbach, F., and Zador, A.M. (2017). A self-initiated two-alternative forced choice paradigm for head-fixed mice. BioRxiv 073783.

Matthews, N., Liu, Z., Geesaman, B.J., and Qian, N. (1999). Perceptual learning on orientation and direction discrimination. Vision Research *39*, 3692–3701.

Maurer, D., and Lewis, T.L. (2018). Visual Systems. In The Neurobiology of Brain and Behavioral Development, R. Gibb, and B. Kolb, eds. (Academic Press), pp. 213–233.

Mckee, S.P., and Westheimer, G. (1978). Improvement in vernier acuity with practice. Perception & Psychophysics *24*, 258–262.

von Melchner, L., Pallas, S.L., and Sur, M. (2000). Visual behaviour mediated by retinal projections directed to the auditory pathway. Nature *404*, 871–876.

Mitchell, D.E., Kennie, J., and Kung, D. (2009). Development of global motion perception requires early postnatal exposure to patterned light. Curr. Biol. *19*, 645–649.

Montijn, J.S., Goltstein, P.M., and Pennartz, C.M. (2015). Mouse V1 population correlates of visual detection rely on heterogeneity within neuronal response patterns. ELife *4*, e10163.

Movshon, J.A., and Newsome, W.T. (1996). Visual Response Properties of Striate Cortical Neurons Projecting to Area MT in Macaque Monkeys. J. Neurosci. *16*, 7733–7741.

Movshon, J.A., Thompson, I.D., and Tolhurst, D.J. (1978a). Receptive field organization of complex cells in the cat's striate cortex. The Journal of Physiology *283*, 79–99.

Movshon, J.A., Thompson, I.D., and Tolhurst, D.J. (1978b). Spatial summation in the receptive fields of simple cells in the cat's striate cortex. J Physiol *283*, 53–77.

Nathanson, J.L., Yanagawa, Y., Obata, K., and Callaway, E.M. (2009). Preferential labeling of inhibitory and excitatory cortical neurons by endogenous tropism of adeno-associated virus and lentivirus vectors. Neuroscience *161*, 441–450.

Nauhaus, I., Nielsen, K.J., Disney, A.A., and Callaway, E.M. (2012). Orthogonal micro-organization of orientation and spatial frequency in primate primary visual cortex. Nature Neuroscience *15*, 1683–1690.

Nauhaus, I., Nielsen, K.J., and Callaway, E.M. (2016). Efficient Receptive Field Tiling in Primate V1. Neuron *91*, 893–904.

Newsome, W.T., and Pare, E.B. (1988). A selective impairment of motion perception following lesions of the middle temporal visual area (MT). J. Neurosci. *8*, 2201–2211.

Ni, A.M., Ruff, D.A., Alberts, J.J., Symmonds, J., and Cohen, M.R. (2018). Learning and attention reveal a general relationship between population activity and behavior. Science *359*, 463–465.

Ohki, K., and Reid, R.C. (2007). Specificity and randomness in the visual cortex. Current Opinion in Neurobiology *17*, 401–407.

Orban, G. (2008). Higher Order Visual Processing in Macaque Extrastriate Cortex. Physiological Reviews *88*, 59 – 89.

Pasupathy, A., and Connor, C.E. (1999). Responses to contour features in macaque area V4. Journal of Neurophysiology *82*, 2490–502.

Pasupathy, A., and Connor, C.E. (2001). Shape representation in area V4: position-specific tuning for boundary conformation. Journal of Neurophysiology *86*, 2505–19.

Paszke, A., Gross, S., Massa, F., Lerer, A., Bradbury, J., Chanan, G., Killeen, T., Lin, Z., Gimelshein, N., Antiga, L., et al. (2019). PyTorch: An Imperative Style, High-Performance Deep Learning Library. Advances in Neural Information Processing Systems 32 8024--8035.

Pelli, D.G. (1997). The VideoToolbox software for visual psychophysics: transforming numbers into movies. Spat Vis *10*, 437–442.

Peters, A.J., Chen, S.X., and Komiyama, T. (2014). Emergence of reproducible spatiotemporal activity during motor learning. Nature *510*, 263–267.

Petrov, A.A., Dosher, B.A., and Lu, Z.-L. (2005). The Dynamics of Perceptual Learning: An Incremental Reweighting Model. Psychological Review *112*, 715–743.

Petrov, A.A., Dosher, B.A., and Lu, Z.-L. (2006). Perceptual learning without feedback in non-stationary contexts: Data and model. Vision Research *46*, 3177–3197.

Philipp, R., Distler, C., and Hoffmann, K.-P. (2006). A Motion-sensitive Area in Ferret Extrastriate Visual Cortex: an Analysis in Pigmented and Albino Animals. Cereb Cortex *16*, 779–790.

Pilly, P.K., and Seitz, A.R. (2009). What a difference a parameter makes: A psychophysical comparison of random dot motion algorithms. Vision Research *49*, 1599–1612.

Poggio, T., Fahle, M., and Edelman, S. (1992). Fast perceptual learning in visual hyperacuity. Science *256*, 1018–1021.

Pollard, J.S., Beale, I.L., Lysons, A.M., and Preston, A.C. (1967). Visual Discrimination in the Ferret. Percept Mot Skills *24*, 279–282.

Pontenagel, T., and Schmidt, U. (1980). Untersuchungen zur Leistungsfaehigkeit des Gesichtssinnes beim Frettchen, Mustela putoris f. furo L. Zeitschrift Fuer Saeugetierkunde *45*, 376–383.

Poort, J., Khan, A.G., Pachitariu, M., Nemri, A., Orsolic, I., Krupic, J., Bauza, M., Sahani, M., Keller, G.B., Mrsic-Flogel, T.D., et al. (2015). Learning Enhances Sensory and Multiple Non-sensory Representations in Primary Visual Cortex. Neuron *86*, 1478–1490.

Pospisil, D.A., Pasupathy, A., and Bair, W. (2018). "Artiphysiology" reveals V4-like shape tuning in a deep network trained for image classification. ELife *7*, e38242.

Prins, N., and Kingdom, F.A.A. (2018). Applying the Model-Comparison Approach to Test Specific Research Hypotheses in Psychophysical Research Using the Palamedes Toolbox. Front. Psychol. *9*.

Raiguel, S., Vogels, R., Mysore, S.G., and Orban, G.A. (2006). Learning to See the Difference Specifically Alters the Most Informative V4 Neurons. J. Neurosci. *26*, 6589–6602.

Rawat, W., and Wang, Z. (2017). Deep Convolutional Neural Networks for Image Classification: A Comprehensive Review. Neural Computation *29*, 2352–2449.

Recanzone, G.H., Jenkins, W.M., Hradek, G.T., and Merzenich, M.M. (1992a). Progressive improvement in discriminative abilities in adult owl monkeys performing a tactile frequency discrimination task. Journal of Neurophysiology *67*, 1015–1030.

Recanzone, G.H., Merzenich, M.M., and Jenkins, W.M. (1992b). Frequency discrimination training engaging a restricted skin surface results in an emergence of a cutaneous response zone in cortical area 3a. Journal of Neurophysiology *67*, 1057–1070.

Recanzone, G.H., Merzenich, M.M., Jenkins, W.M., Grajski, K.A., and Dinse, H.R. (1992c). Topographic reorganization of the hand representation in cortical area 3b owl monkeys trained in a frequency-discrimination task. Journal of Neurophysiology *67*, 1031–1056.

Recanzone, G.H., Merzenich, M.M., and Schreiner, C.E. (1992d). Changes in the distributed temporal response properties of SI cortical neurons reflect improvements in performance on a temporally based tactile discrimination task. Journal of Neurophysiology *67*, 1071–1091.

Recanzone, G.H., Schreiner, C.E., and Merzenich, M.M. (1993). Plasticity in the frequency representation of primary auditory cortex following discrimination training in adult owl monkeys. J. Neurosci. *13*, 87–103.

Redies, C., Diksic, M., and Riml, H. (1990). Functional organization in the ferret visual cortex: a double-label 2-deoxyglucose study. J. Neurosci. *10*, 2791–2803.

Reed, A., Riley, J., Carraway, R., Carrasco, A., Perez, C., Jakkamsetti, V., and Kilgard, M.P. (2011). Cortical Map Plasticity Improves Learning but Is Not Necessary for Improved Performance. Neuron *70*, 121–131.

Robnik-Sikonja, M., and Kononenko, I. (2008). Explaining Classifications For Individual Instances. IEEE Transactions on Knowledge and Data Engineering *20*, 589–600.

Roelfsema, P.R., and Van Ooyen, A. (2005). Attention-Gated Reinforcement Learning of Internal Representations for Classification. Neural Computation *17*, 2176–2214.

Roitman, J.D., and Shadlen, M.N. (2002). Response of Neurons in the Lateral Intraparietal Area during a Combined Visual Discrimination Reaction Time Task. J. Neurosci. *22*, 9475–9489.

Rosenthal, O., and Humphreys, G.W. (2010). Perceptual Organization Without Perception: The Subliminal Learning of Global Contour. Psychol Sci *21*, 1751–1758.

Rubin, N., Nakayama, K., and Shapley, R. (1997). Abrupt learning and retinal size specificity in illusory-contour perception. Current Biology *7*, 461–467.

Rudolph, K.K., and Pasternak, T. (1996). Lesions in Cat Lateral Suprasylvian Cortex Affect the Perception of Complex Motion. Cerebral Cortex *6*, 814–822.

Ruiz, O., Lustig, B.R., Nassi, J.J., Cetin, A., Reynolds, J.H., Albright, T.D., Callaway, E.M., Stoner, G.R., and Roe, A.W. (2013). Optogenetics through windows on the brain in the nonhuman primate. Journal of Neurophysiology *110*, 1455–1467.

Sadakane, O., Masamizu, Y., Watakabe, A., Terada, S.-I., Ohtsuka, M., Takaji, M., Mizukami, H., Ozawa, K., Kawasaki, H., Matsuzaki, M., et al. (2015). Long-Term Two-Photon Calcium Imaging of Neuronal Populations with Subcellular Resolution in Adult Non-human Primates. Cell Reports *13*, 1989–1999.

Sagi, D. (2011). Perceptual learning in Vision Research. Vision Research *51*, 1552–1566.

Sale, A., De Pasquale, R., Bonaccorsi, J., Pietra, G., Olivieri, D., Berardi, N., and Maffei, L. (2011). Visual perceptual learning induces long-term potentiation in the visual cortex. Neuroscience *172*, 219–225.

Salzman, C., Britten, K., and Newsome, W. (1990). Cortical microstimulation influences perceptual judgements of motion direction. Nature *346*, 174–177.

Sanayei, M., Chen, X., Chicharro, D., Distler, C., Panzeri, S., and Thiele, A. (2018). Perceptual learning of fine contrast discrimination changes neuronal tuning and population coding in macaque V4. Nature Communications *9*, 1–15.

Santisakultarm, T.P., Kersbergen, C.J., Bandy, D.K., Ide, D.C., Choi, S.-H., and Silva, A.C. (2016). Two-photon imaging of cerebral hemodynamics and neural activity in awake and anesthetized marmosets. Journal of Neuroscience Methods *271*, 55–64.

Scholl, B., Wilson, D.E., and Fitzpatrick, D. (2017). Local Order within Global Disorder: Synaptic Architecture of Visual Space. Neuron *96*, 1127-1138.e4.

Scholte, H.S., Losch, M.M., Ramakrishnan, K., de Haan, E.H.F., and Bohte, S.M. (2018). Visual pathways from the perspective of cost functions and multi-task deep neural networks. Cortex *98*, 249–261.

Schoups, A., Vogels, R., Qian, N., and Orban, G. (2001). Practising orientation identification improves orientation coding in V1 neurons. Nature *412*, 549–553.

Schoups, A.A., Vogels, R., and Orban, G.A. (1995). Human perceptual learning in identifying the oblique orientation: retinotopy, orientation specificity and monocularity. The Journal of Physiology *483*, 797–810.

Schütz, A.C., Braun, D.I., Movshon, J.A., and Gegenfurtner, K.R. (2010). Does the noise matter? Effects of different kinematogram types on smooth pursuit eye movements and perception. Journal of Vision *10*, 26–26.

Schwartz, S., Maquet, P., and Frith, C. (2002). Neural correlates of perceptual learning: A functional MRI study of visual texture discrimination. Proc Natl Acad Sci U S A *99*, 17137–17142.

Seitz, A.R., and Watanabe, T. (2003). Is subliminal learning really passive? Nature *422*, 36–36.

Seitz, A.R., Kim, D., and Watanabe, T. (2009). Rewards evoke learning of unconsciously processed visual stimuli in adult humans. Neuron *61*, 700–707.

Serre, T. (2019). Deep Learning: The Good, the Bad, and the Ugly. Annu. Rev. Vis. Sci. *5*, 399–426.

Shadlen, M.N., and Newsome, W.T. (2001). Neural Basis of a Perceptual Decision in the Parietal Cortex (Area LIP) of the Rhesus Monkey. Journal of Neurophysiology *86*, 1916–1936.

Shadlen, M.N., Britten, K.H., Newsome, W.T., and Movshon, J.A. (1996). A computational analysis of the relationship between neuronal and behavioral responses to visual motion. J. Neurosci. *16*, 1486–1510.

Sharma, J., and Sur, M. (2014). The Ferret as a Model for Visual System Development and Plasticity. In Biology and Diseases of the Ferret, (John Wiley & Sons, Ltd), pp. 711–734.

Shiu, L.-P., and Pashler, H. (1992). Improvement in line orientation discrimination is retinally local but dependent on cognitive set. Perception & Psychophysics *52*, 582–588.

Shmuel, A., and Grinvald, A. (1996). Functional Organization for Direction of Motion and Its Relationship to Orientation Maps in Cat Area 18. J. Neurosci. *16*, 6945–6964.

Shtoyerman, E., Arieli, A., Slovin, H., Vanzetta, I., and Grinvald, A. (2000). Long-Term Optical Imaging and Spectroscopy Reveal Mechanisms Underlying the Intrinsic Signal and Stability of Cortical Maps in V1 of Behaving Monkeys. J. Neurosci. *20*, 8111–8121.

Smith, G., and Fitzpatrick, D. (2016). Viral Injection and Cranial Window Implantation for In Vivo Two-Photon Imaging. In Methods in Molecular Biology (Clifton, N.J.), pp. 171–185.

Smith, G.B., Sederberg, A., Elyada, Y.M., Van Hooser, S.D., Kaschube, M., and Fitzpatrick, D. (2015). The development of cortical circuits for motion discrimination. Nat. Neurosci. *18*, 252–261.

Smith, G.B., Hein, B., Whitney, D.E., Fitzpatrick, D., and Kaschube, M. (2018). Distributed network interactions and their emergence in developing neocortex. Nature Neuroscience *21*, 1600–1608.

Sommer, M.A., and Wurtz, R.H. (2004). What the Brain Stem Tells the Frontal Cortex. I. Oculomotor Signals Sent From Superior Colliculus to Frontal Eye Field Via Mediodorsal Thalamus. Journal of Neurophysiology *91*, 1381–1402.

Sotiropoulos, G., Seitz, A.R., and Seriès, P. (2011). Perceptual learning in visual hyperacuity: A reweighting model. Vision Research *51*, 585–599.

Sotiropoulos, G., Seitz, A.R., and Seriès, P. (2018). Performance-monitoring integrated reweighting model of perceptual learning. Vision Research *152*, 17–39.

Sowden, P.T., Rose, D., and Davies, I.R.L. (2002). Perceptual learning of luminance contrast detection: specific for spatial frequency and retinal location but not orientation. Vision Research *42*, 1249–1258.

Steinmetz, N.A., Koch, C., Harris, K.D., and Carandini, M. (2018). Challenges and opportunities for large-scale electrophysiology with Neuropixels probes. Current Opinion in Neurobiology *50*, 92–100.

Stitt, I., Zhou, Z.C., Radtke-Schuller, S., and Fröhlich, F. (2018). Arousal dependent modulation of thalamo-cortical functional interaction. Nat Commun *9*, 2455.

Swindale, N.V., Matsubara, J.A., and Cynader, M.S. (1987). Surface organization of orientation and direction selectivity in cat area 18. J. Neurosci. *7*, 1414–1427.

Swindale, N.V., Shoham, D., Grinvald, A., Bonhoeffer, T., and Hübener, M. (2000). Visual cortex maps are optimized for uniform coverage. Nature Neuroscience *3*, 822–826.

Szpiro, S.F.A., Wright, B.A., and Carrasco, M. (2014). Learning one task by interleaving practice with another task. Vision Research *101*, 118–124.

Talluri, B.C., Hung, S.-C., Seitz, A.R., and Seriès, P. (2015). Confidence-based integrated reweighting model of task-difficulty explains location-based specificity in perceptual learning. Journal of Vision *15*, 17–17.

Teich, A.F., and Qian, N. (2003). Learning and Adaptation in a Recurrent Model of V1 Orientation Selectivity. Journal of Neurophysiology *89*, 2086–2100.

Tian, L., Hires, S.A., Mao, T., Huber, D., Chiappe, M.E., Chalasani, S.H., Petreanu, L., Akerboom, J., McKinney, S.A., Schreiter, E.R., et al. (2009). Imaging neural activity in worms, flies and mice with improved GCaMP calcium indicators. Nature Methods *6*, 875–881.

Tootell, R.B., Silverman, M.S., and Valois, R.D. (1981). Spatial frequency columns in primary visual cortex. Science *214*, 813–815.

Tsushima, Y., Seitz, A.R., and Watanabe, T. (2008). Task-irrelevant learning occurs only when the irrelevant feature is weak. Curr Biol *18*, R516–R517.

Umeda, K., Tanabe, S., and Fujita, I. (2007). Representation of Stereoscopic Depth Based on Relative Disparity in Macaque Area V4. Journal of Neurophysiology *98*, 241–252.

Ungerleider, L.G., and Pasternak, T. (2004). Ventral and dorsal cortical processing streams. In The Visual Neurosciences, (Cambridge: MIT Press), pp. 541–562.

Vaina, L.M., Sundareswaran, V., and Harris, J.G. (1995). Learning to ignore: psychophysics and computational modeling of fast learning of direction in noisy motion stimuli. Cognitive Brain Research *2*, 155–163.

Van Hooser, S.D., Li, Y., Christensson, M., Smith, G.B., White, L.E., and Fitzpatrick, D. (2012). Initial neighborhood biases and the quality of motion stimulation jointly influence the rapid emergence of direction preference in visual cortex. Journal of Neuroscience *32*, 7258–66.

Vogels, R., and Orban, G.A. (1985). The effect of practice on the oblique effect in line orientation judgments. Vision Research *25*, 1679–1687.

Wang, Q., and Burkhalter, A. (2007). Area map of mouse visual cortex. Journal of Comparative Neurology *502*, 339–357.

Wang, R., Zhang, J.-Y., Klein, S.A., Levi, D.M., and Yu, C. (2012). Task relevancy and demand modulate double-training enabled transfer of perceptual learning. Vision Research *61*, 33–38.

Wang, R., Zhang, J.-Y., Klein, S.A., Levi, D.M., and Yu, C. (2014). Vernier perceptual learning transfers to completely untrained retinal locations after double training: A “piggybacking” effect. Journal of Vision *14*, 12–12.

Watakabe, A., Ohtsuka, M., Kinoshita, M., Takaji, M., Isa, K., Mizukami, H., Ozawa, K., Isa, T., and Yamamori, T. (2015). Comparative analyses of adeno-associated viral vector serotypes 1, 2, 5, 8 and 9 in marmoset, mouse and macaque cerebral cortex. Neuroscience Research *93*, 144–157.

Watanabe, T., and Sasaki, Y. (2015). Perceptual Learning: Toward a Comprehensive Theory. Annual Review of Psychology *66*, 197–221.

Watanabe, T., Náñez, J.E., and Sasaki, Y. (2001). Perceptual learning without perception. Nature *413*, 844–848.

Weiss, Y., Edelman, S., and Fahle, M. (1993). Models of Perceptual Learning in Vernier Hyperacuity. Neural Computation *5*.

Wenliang, L.K., and Seitz, A.R. (2018). Deep Neural Networks for Modeling Visual Perceptual Learning. J. Neurosci. *38*, 6028–6044.

White, L.E., Coppola, D.M., and Fitzpatrick, D. (2001). The contribution of sensory experience to the maturation of orientation selectivity in ferret visual cortex. Nature *411*, 1049–1052.

Wichmann, F.A., and Hill, N.J. (2001). The psychometric function: I. Fitting, sampling, and goodness of fit. Perception & Psychophysics *63*, 1293–1313.

Wickersham, I.R., and Feinberg, E.H. (2012). New technologies for imaging synaptic partners. Current Opinion in Neurobiology *22*, 121–127.

Wiesel, T.N., and Hubel, D.H. (1963). Single-cell responses in striate cortex of kittens deprived of vision in one eye. Journal of Neurophysiology *26*, 1003–1017.

WILLIAM H. PRESS, Brian P. Flannery, Saul A. Teukolsky, and William T. Vetterling (1992). Numerical recipes in C (Cambridge University Press).

Wilson, H.R., and Wilkinson, F. (1998). Detection of global structure in Glass patterns: implications for form vision. Vision Res. *38*, 2933–2947.

Wilson, D.E., Whitney, D.E., Scholl, B., and Fitzpatrick, D. (2016). Orientation selectivity and the functional clustering of synaptic inputs in primary visual cortex. Nature Neuroscience *19*, 1003–1009.

Wilson, H.R., Wilkinson, F., and Asaad, W. (1997). Concentric orientation summation in human form vision. Vision Research *37*, 2325–2330.

Wu, F., Stark, E., Ku, P.-C., Wise, K.D., Buzsáki, G., and Yoon, E. (2015). Monolithically Integrated µLEDs on Silicon Neural Probes for High-Resolution Optogenetic Studies in Behaving Animals. Neuron *88*, 1136–1148.

Xiao, L.-Q., Zhang, J.-Y., Wang, R., Klein, S.A., Levi, D.M., and Yu, C. (2008). Complete Transfer of Perceptual Learning across Retinal Locations Enabled by Double Training. Current Biology *18*, 1922–1926.

Yamahachi, H., Marik, S.A., McManus, J.N.J., Denk, W., and Gilbert, C.D. (2009). Rapid Axonal Sprouting and Pruning Accompany Functional Reorganization in Primary Visual Cortex. Neuron *64*, 719–729.

Yamins, D.L.K., Hong, H., Cadieu, C.F., Solomon, E.A., Seibert, D., and DiCarlo, J.J. (2014). Performance-optimized hierarchical models predict neural responses in higher visual cortex. Proc Natl Acad Sci U S A *111*, 8619–8624.

Yang, T., and Maunsell, J.H.R. (2004). The Effect of Perceptual Learning on Neuronal Responses in Monkey Visual Area V4. J. Neurosci. *24*, 1617–1626.

Yotsumoto, Y., Watanabe, T., and Sasaki, Y. (2008). Different Dynamics of Performance and Brain Activation in the Time Course of Perceptual Learning. Neuron *57*, 827–833.

Young, M. (1993). The organization of neural systems in the primate cerebral cortex. Proceedings of the Royal Society of London. Series B: Biological Sciences *252*, 13–18.

Yu, H., Farley, B.J., Jin, D.Z., and Sur, M. (2005). The Coordinated Mapping of Visual Space and Response Features in Visual Cortex. Neuron *47*, 267–280.

Zeiler, M.D., and Fergus, R. (2013). Visualizing and Understanding Convolutional Networks. ArXiv:1311.2901 [Cs].

Zhang, J.-Y., Zhang, G.-L., Xiao, L.-Q., Klein, S.A., Levi, D.M., and Yu, C. (2010a). Rule-Based Learning Explains Visual Perceptual Learning and Its Specificity and Transfer. J. Neurosci. *30*, 12323–12328.

Zhang, T., Xiao, L.-Q., Klein, S.A., Levi, D.M., and Yu, C. (2010b). Decoupling location specificity from perceptual learning of orientation discrimination. Vision Research *50*, 368–374.

Zhaoping, L., Herzog, M.H., and Dayan, P. (2003). Nonlinear ideal observation and recurrent preprocessing in perceptual learning. Network: Computation in Neural Systems *14*, 233–247.

Zhou, Z.C., Yu, C., Sellers, K.K., and Fröhlich, F. (2016). Dorso-Lateral Frontal Cortex of the Ferret Encodes Perceptual Difficulty during Visual Discrimination. Scientific Reports *6*, 23568.

Zintgraf, L.M., Cohen, T.S., Adel, T., and Welling, M. (2017). Visualizing Deep Neural Network Decisions: Prediction Difference Analysis. ArXiv:1702.04595 [Cs].

Zoccolan, D., Graham, B.J., and Cox, D.D. (2010). A Self-Calibrating, Camera-Based Eye Tracker for the Recording of Rodent Eye Movements. Front. Neurosci. *4*.

7 Curriculum Vitae

Erika L. Dunn-Weiss
Zanvyl Krieger Mind/Brain Institute and Department of Neuroscience
Johns Hopkins University
338 Krieger Hall
3400 N. Charles St, Baltimore, MD 21218
Phone: +1 (203) 940 1729
Email: edunnwe1@jhmi.edu

Education

Since 2014 **Ph.D. Student, Neuroscience**
Johns Hopkins University
Cumulative GPA: 3.93/4.0

2013 **Bachelor of Science with General Honors, Mathematics**
The University of Chicago
Cumulative GPA: 3.49/4.0
Dean's List 2010, 2012, 2013

Positions and Honors

Since 2015 **Ph.D. Student, Nielsen Lab**
Advisors: Kristina J. Nielsen
Johns Hopkins University
Research subject: *Perceptual learning: experimental and computational considerations*

2018 **Helmsley Fellowship**

2011 - 2013 **Research Assistant, Bensmaia Lab**
University of Chicago
Research subject: *Neural correlates in S1 & S3b of perceived intensity - multiplexed stimuli information and afferent contributions to cortical activity*
Advisors: S. Bensmaia, H. Saal

2012 **Selected participant, Mathematics R.E.U.**
University of Chicago
Research subject: *Semi-Riemannian and Riemannian manifolds of constant sectional curvature - characterization of model spaces up to isometries*
Advisors: D. Constantine, A. Lawrie, C. Rodriguez

2010 – 2011 **Research Assistant, Social Cognitive Neuroscience Lab**
University of Chicago

Publications

Articles

Dunn-Weiss, E., Nummela, S.U., Lempel, A.A., Law, J. , Ledley, J., Salvino, P., Nielsen, K.J. Visual Motion and Form Integration in the Behaving Ferret, *eNeuro* (2019).

Dunn-Weiss, E. & Nielsen, K.J. Cascading effects of perceptual learning in a deep convolutional neural network. *In preparation.*

Dunn-Weiss, E., Daniels, A., Nielsen, K.J. Chronic two-photon imaging in ferrets: chamber design and best practices. *In preparation.*

Dunn-Weiss, E. **,** Nielsen, K.J. Categorical boundaries in perceptual learning. *In preparation*.

Abstracts

Dunn-Weiss, E.L., Ross, J.J., Nielsen, K.J., Visual Perceptual Learning in the Ferret, *Society for Neuroscience 2019*

Dunn-Weiss, E.L., Nielsen, K.J. Assessing the visual capabilities of the ferret using psychophysics and electrophysiology. *2019 Vision Sciences Society.*

Dunn-Weiss, E.L., Nielsen, K.J., Development of head-fixed visual behavior and chronic recording techniques in the ferret, *2019 Brain Initiative Investigators Meeting.*

Dunn-Weiss, E.L., Nielsen, K.J., Visual Psychophysics in the Ferret, *Society for Neuroscience 2017.*

Internal publications

Dunn-Weiss, E. *Introduction to Geometry*.
http://math.uchicago.edu/~may/REU2012/REUPapers/Dunn-Weiss.pdf

Graduate coursework

2018 **Cold Spring Harbor Laboratory**

- ❑ Computational Neuroscience: Vision

2014 - 2017 **Johns Hopkins University**

- ❑ Neuroscience & Cognition
- ❑ Algebraic Topology
- ❑ Statistical Theory
- ❑ Statistical Connectomics
- ❑ Principles of Complex Networked Systems

- ❑ Current Issues in Systems Neuroscience
- ❑ Visual System

Fall 2013 **Center for Neural Engineering and Computation, Columbia University**

- ❑ Computational Neuroscience

Programming languages

MATLAB, Python (pandas, scipy, PyTorch)

Service

Since 2017 **Student Diversity Committee, Co-Founder, Member**
Johns Hopkins University, Neuroscience Department

Advised faculty within the Neuroscience Department on training initiatives, student and faculty recruitment, and grant proposals. Organized the first interdepartmental panel discussion and happy hour for under-represented minority students and faculty at the Johns Hopkins School of Medicine

2018 - 2019 **Johns Hopkins University Biomedical Odyssey Blog, Writer**
Selected work:
"Responsibility Without Blame: An Interview with Philosopher Hanna Pickard"

"Underrepresented minority biomedical researchers: numbers, challenges, and initiatives for change"

2017 - 2018 **Neuroscience Department Diversity Committee, Member**
Johns Hopkins University

2015 - 2016 **Mentor**
Ingenuity project, Baltimore Polytechnic Institute, Baltimore Public Schools
Mission: "To prepare and launch the next diverse generation of nationally competitive STEM leaders in Baltimore City Public Schools"
Advised a high school student on an independent research project. Trained the student in coding, experimental design, scientific writing and scientific presentation via weekly meetings.

Since 2009 **Mentor**
Women and Youth Supporting Each other (WYSE), University of Chicago
Madero Middle School, Little Village, Chicago
Mission: "To empower young women by providing the resources and support necessary to make positive life choices and create community change"

2012 - 2013 **University of Chicago Clothesline Project, Director & Co-Founder**

Mission: "The UChicago Clothesline Project amplifies the voices of victims/survivors of sexual violence on campus by rendering their stories on t-shirts and displaying them on the quads. We aim to transform public consciousness around the issue of sexual assault."

2012 **Teacher's Aide, Mathematics**

Collegiate Scholars Summer Program, Chicago Public Schools

Worked with high school students from underrepresented backgrounds to prepare them for college-level mathematics